

ABSTRACT

Title of Dissertation: Charged Antiparticle to Particle Ratios
Near Midrapidity in d+Au and
p+p Collisions at $\sqrt{s_{NN}} = 200$ GeV

Abigail Anne Bickley, Doctor of Philosophy, 2004

Dissertation Directed by: Professor Alice C. Mignerey
Department of Chemistry and Biochemistry

Experiments at the Relativistic Heavy Ion Collider (RHIC) at Brookhaven National Laboratory are designed to investigate the behavior of strongly interacting matter at high temperatures and densities. The conditions created during a heavy ion collision at RHIC energies are predicted to be sufficient to form a quark-gluon plasma. As part of this investigation, smaller collision systems need to be studied to aid in the understanding and interpretation of results from the more complicated heavy ion collisions.

This thesis reports the ratios of the yields of antiparticles to particles for primary charged pions, kaons, and protons emitted in p+p and d+Au collisions at $\sqrt{s_{NN}} = 200$ GeV. In the d+Au collision system the results are measured as a function of collision centrality. The data analyzed were collected by the PHOBOS detector during the 2003 run of the Relativistic Heavy Ion Collider. Comparison of the results obtained in this thesis with the antiparticle to particle ratios measured in 200 GeV Au+Au collisions allows the effects of final state interactions on the

produced particle yields to be inferred. Furthermore, measurement of the antiproton to proton ratio allows the relative influence of the baryon number transport and the antibaryon-baryon pair production mechanisms on the collision process to be investigated.

The measured antiparticle to particle ratios represent the ratio of the yields averaged over the rapidity range of $0.1 < y_\pi < 1.3$ and $0 < y_{K,p} < 0.8$, and for transverse momenta of $0.1 < p_T^{\pi,K} < 1.0$ GeV/c and $0.3 < p_T^p < 1.0$ GeV/c. In the d+Au collision system it is found that the relative yields of antiparticles to particles are independent of centrality for all three particle species, pions, kaons and protons. The $\langle \pi^-/\pi^+ \rangle$ ratio at all centralities is consistent with one. In the top 10% most central events $\langle \pi^-/\pi^+ \rangle = 1.016 \pm 0.007$ (stat.) ± 0.019 (syst.) and in the 60–100% most peripheral events $\langle \pi^-/\pi^+ \rangle = 0.996 \pm 0.008$ (stat.) ± 0.013 (syst.). The $\langle K^-/K^+ \rangle$ ratio ranges from 0.97 ± 0.03 (stat.) ± 0.04 (syst.) in the top 10% most central events to 1.00 ± 0.04 (stat.) ± 0.03 (syst.) in the 60–100% most peripheral events. The $\langle \bar{p}/p \rangle$ ratio ranges from 0.86 ± 0.02 (stat.) ± 0.04 (syst.) in the top 10% most central events to 0.85 ± 0.02 (stat.) ± 0.03 (syst.) in the 60–100% most peripheral events. The results obtained for the p+p collision system are consistent with the values measured in d+Au collisions. Ratios of $\langle \pi^-/\pi^+ \rangle = 1.000 \pm 0.012$ (stat.) ± 0.019 (syst.), $\langle K^-/K^+ \rangle = 0.93 \pm 0.05$ (stat.) ± 0.03 (syst.), and $\langle \bar{p}/p \rangle = 0.85 \pm 0.04$ (stat.) ± 0.03 (syst.) have been measured. The data are compared to results from model calculations, other collision systems and other collision energies.

Charged Antiparticle to Particle Ratios Near Midrapidity in
d+Au and p+p Collisions at $\sqrt{s_{NN}} = 200$ GeV

by

Abigail Anne Bickley

Dissertation submitted to the Faculty of the Graduate School of the
University of Maryland in partial fulfillment
of the requirements for the degree of
Doctor of Philosophy
2004

Advisory Committee:

Professor Alice C. Mignerey, Chair/Advisor
Professor Elizabeth J. Beise
Professor Sandra C. Greer
Professor Robert A. Walker
Professor William B. Walters

© Copyright by
Abigail Anne Bickley
2004

Dedicated to
James Bickley

ACKNOWLEDGMENTS

I would like to thank my advisor, Alice Mignerey, for her guidance during my graduate career. Specifically, I appreciate that she allowed me to set my own course of research and to learn to work both independently and as part of a collaboration. She has been instrumental in providing the resources I needed to be able to work successfully away from the University of Maryland at Brookhaven National Laboratory.

As a member of the Brookhaven group, Nigel George played an integral role in my graduate career. Most importantly we worked side by side to develop the vertexless straight tracking modules and d+Au ratios analysis. I would like to thank Nigel for his guidance in navigating the political landscape of the PHOBOS collaboration and for helping me translate my chemistry background into physics vocabulary.

The Brookhaven group has provided me with a home away from the University of Maryland during my graduate career. I thank Mark Baker for incorporating me into the group and making my stay here a rewarding experience. Due to his integrity and intelligence Mark has been a scientific role model. I would also like to thank Peter Steinberg, who played an important role in incorporating me into the collaboration when I first arrived at Brookhaven. I continue to learn about the field through conversations with Peter who always challenges me to look at issues from

different perspectives. Finally, I would like to thank Burt Holzman who has been an invaluable resource and always patiently answers my questions no matter how naive they may be.

Within the collaboration, the particle ratios review committee, consisting of Frank Wolfs, George Stephans and Robert Pak, has played an important role in the development of the ratios analysis. Their efforts in evaluating the analysis procedure and making sure no stone was left unturned have been invaluable. It is only through their hard work that we have been able to get both the d+Au and p+p ratios papers submitted for publication.

I would like to thank Kris Gulbrandsen, who worked on both the 130 and 200 GeV Au+Au particle ratios analyses, for providing his expertise and advice during the course of the d+Au analysis. The trigger group from the University of Illinois at Chicago, consisting of Dave Hoffman, Richard Hollis, Aneta Iordanova and Joe Sagerer, all worked tirelessly not only setting up the triggering for d+Au and p+p runs but also determining the efficiencies and centrality cuts. The MIT tracking group, Gunther Roland, Conor Henderson and Jay Kane, helped with the development and implementation of the vertexless straight tracking modules, without which this analysis would not have been possible. In addition, I would like to thank the entire PHOBOS collaboration for not only building and operating our detector, but also for maximizing the quantity and quality of our research.

I would like to acknowledge the support of the 214 group, Nigel George, Carla Vale, Ming Kuo, Corey Reed and Marguerite Tonjes. The working and social environment of our office made everything we did that much more enjoyable. I would

like to thank Richard Bindel for helping me navigate the Chemistry Department at the University of Maryland and introducing me to root, Phat and the PHOBOS way.

Two organizations that I was involved in prior to becoming a graduate student merit recognition due to their influence on my educational path. The Indiana Academy for Science, Mathematics and Humanities and in particular Dr. Tom Adams played an integral role in providing me with the fundamentals of chemistry required for success. The Nuclear Chemistry Summer School, sponsored by the Division of Nuclear Chemistry and Technology of the American Chemical Society, taught by Dr. Frank Kinard played a pivotal role in my decision to pursue a career in nuclear chemistry.

Most importantly I would like to thank my family. My husband has provided crucial support during the roller coaster ride known as graduate school and my parents provided me with the drive and motivation to succeed.

TABLE OF CONTENTS

List of Tables	xi
List of Figures	xv
1 Introduction	1
1.1 Standard Model & QCD	3
1.2 Relativistic Heavy Ion Collisions	8
1.2.1 Historical Perspective	9
1.2.2 Collision Evolution	11
1.2.3 Experimental Observables	13
1.2.4 Theoretical Models	15
1.3 Thesis Overview	17
1.3.1 Antiparticle to Particle Ratios	18
1.3.2 Baryon Number Transport	19

2	The PHOBOS Experiment	21
2.1	Relativistic Heavy Ion Collider	22
2.2	The PHOBOS Detector	24
2.2.1	Event Triggering	25
2.2.2	Event Vertex Determination	38
2.2.3	Centrality Determination	40
2.2.4	Particle Identification	44
3	Event Selection and Centrality Determination	52
3.1	Trigger Criteria	53
3.1.1	dAVertex Trigger	55
3.1.2	dAPeriph Trigger	55
3.1.3	ppVertex Trigger	56
3.2	Event Selection	56
3.2.1	d+Au Collision Criteria	56
3.2.2	p+p Collision Criteria	61
3.3	Data Selection	62
3.3.1	Beam Orbit Regions	62
3.3.2	Data Quality	63
3.4	Centrality Determination	69
3.4.1	Ring Multiplicity Counters	70
3.4.2	Proton Calorimeter	74

4	Particle Tracking	78
4.1	Magnetic Field	79
4.2	Straight Tracking	80
4.3	Curved Tracking	83
4.4	Straight and Curved Track Matching	86
4.5	Momentum Reconstruction	89
4.5.1	Numerical Track Model	89
4.5.2	Covariance Matrices	90
4.5.3	χ^2 Minimization	92
4.5.4	Fit Probability	93
4.6	Track Reconstruction Efficiency	94
4.7	Momentum Resolution	95
5	Particle Identification	98
5.1	Energy Loss in Matter	99
5.2	Bethe-Bloch Prediction	99
5.2.1	Density Correction	100
5.2.2	Shell Correction	101
5.2.3	Application in PHOBOS	102
5.3	Particle Identification Cuts	103
5.4	Acceptance	106
5.5	Electron Contamination	106

6	Raw Particle Ratios	113
6.1	Track Selection	114
6.2	Particle Yields & Normalization	117
6.2.1	Event Normalization and Weighting	117
6.3	Raw Ratios Calculation	120
6.4	Cross Checks	121
6.4.1	Kinematic Distributions	122
6.4.2	Magnetic Field Stability	123
7	Corrected Particle Ratios	125
7.1	Feed-down Correction	126
7.1.1	Proton Feed-down Correction Factor	127
7.1.2	Pion Feed-down Correction Factor	136
7.1.3	Kaon Feed-down Correction Factor	139
7.2	Secondary Correction	141
7.2.1	Proton Secondary Correction	141
7.2.2	Pion and Kaon Secondary Correction	144
7.3	Absorption Correction	145
7.4	Final Particle Ratios	149
8	Error Analysis	150
8.1	Statistical Error Calculation	151
8.2	Systematic Error Calculation	152

9	Results and Discussion	159
9.1	Results	160
9.1.1	Centrality Dependence of Ratios	160
9.1.2	Comparison with Models	161
9.2	Discussion	162
9.2.1	RHIC $\langle \bar{p} \rangle / \langle p \rangle$ Ratio	162
9.2.2	Comparison with Au+Au Collisions	163
9.2.3	Energy Dependence of Ratios	165
9.2.4	Baryon Number Transport	166
9.3	Conclusions	168
A	PHOBOS Collaboration List	170
B	Raw Particle and Event Counts	171
C	Systematic Errors: dAVertex and dAPeriph	178
D	Systematic Errors: ppVertex	184
	Bibliography	189

LIST OF TABLES

1.1	Quarks and their Physical Properties	3
1.2	Leptons and their Physical Properties	4
1.3	Forces and their Properties	4
1.4	Terminology and Definitions	18
2.1	RHIC Beam Energies and Collision Systems for Each Run	24
2.2	Spectrometer Sensor Specifications	46
3.1	Event Selection Criteria for the d+Au Data Sets	57
3.2	Event Selection Criteria for the p+p Data Set	62
3.3	Beam Orbit Regions for All Data Sets	63
3.4	Variables Used to Determine Data Quality	66
3.5	Variables Used to Determine Data Quality, continued	67
3.6	Runs from Each Data Set that Show Significant Deviation from the Mean Data Quality Parameters	69
3.7	Centrality Cuts Used for the d+Au Collision System	73
3.8	Average Centrality Variables for Each Centrality Bin	74

3.9	Centrality Cuts and Average Number of Participants $\langle N_{part} \rangle$ Determined Using the Proton Calorimeter	77
4.1	Track Matching Criteria	87
4.2	Covariance Matrix Bins	91
4.3	Particle Trajectory Parameters	93
5.1	Bethe-Bloch Equation Symbols	100
5.2	Density Correction Equation Symbols [53]	101
5.3	d+Au Data and Monte-Carlo Electron Contamination Comparison .	108
5.4	Relative Fraction of Electrons and Pions Found in the d+Au HIJING Monte-Carlo Simulation for $p < 0.55$ GeV/c	109
5.5	Definitions for the Derivation of the Electron Contamination Correction Factor, Equations 5.5 - 5.9	111
5.6	Estimated Correction Factors for the Measured π^-/π^+ Ratio	111
5.7	Estimated Electron Contamination Correction Factors for the Measured π^-/π^+ Ratio	112
6.1	Track Selection Criteria for All Data Sets	114
6.2	Summary of Particle and Event Counts for Each Data Set	118
6.3	Summary of Track Weighted Average Z-Vertex Position for Pions, Kaons and Protons in the dAVertex Data Set	120
6.4	Normalized Slope of the B^+/B^- Ratio of the Z-Vertex Distributions for All Data Sets	121

6.5	Raw Particle Ratios	122
6.6	Percentage Difference Between Average Kinematic Variables for An- tiparticles and Particles of Both Bending Directions	123
7.1	Lower Bound to $\frac{(\bar{p}_{prim}^{prod}/p_{prim}^{prod})}{(\bar{\Lambda}_{prim}^{prod}/\Lambda_{prim}^{prod})}$ Estimate	131
7.2	Experimental and HIJING Monte-Carlo Measurements of $\frac{dN}{dy}(\bar{\Lambda})$ and $\frac{dN}{dy}(p)$	132
7.3	$\frac{\bar{p}}{p}$ Feed-down Correction Factors and Systematic Errors	136
7.4	Sources of Decay Background for π^-	137
7.5	Sources of Decay Background for π^+	137
7.6	Feed-down Correction Factors for the Measured $\frac{\pi^-}{\pi^+}$ Ratio	139
7.7	Sources of Decay Background for K^- and K^+	139
7.8	Feed-down Correction Factors for the Measured $\frac{K^-}{K^+}$ Ratio	140
7.9	Fit Parameters for the Ratio of Secondary Protons to Primary Pro- tons for d+Au and p+p Collisions	144
7.10	Antiparticle to Particle Ratios for Each Centrality Bin	149
8.1	Antiparticle to Particle Ratios and Statistical Errors for Each Cen- trality Bin	152
8.2	Systematic Error Cut Variations	153
8.3	Systematic Error Cut Variations, continued	154
8.4	Systematic Error from Correction Factors	157
8.5	Antiparticle to Particle Ratios, Statistical Errors and Systematic Er- rors for Each Centrality Bin.	158

B.1	Summary of Weighted π^- and Event Counts for All Data Sets	172
B.2	Summary of Weighted π^+ and Event Counts for All Data Sets	173
B.3	Summary of Weighted K^- and Event Counts for All Data Sets	174
B.4	Summary of Weighted K^+ and Event Counts for All Data Sets	175
B.5	Summary of Weighted \bar{p} and Event Counts for All Data Sets	176
B.6	Summary of Weighted p and Event Counts for All Data Sets	177
C.1	Event Selection Systematic Errors for the dAVertex and dAPeriph Data Sets	179
C.2	Centrality Determination Systematic Errors for the dAVertex and dAPeriph Data Sets	180
C.3	Track Selection Systematic Errors for the dAVertex and dAPeriph Data Sets	181
C.4	Particle Identification Systematic Errors for the dAVertex and dAPeriph Data Sets	182
C.5	Other Systematic Errors for the dAVertex and dAPeriph Data Sets .	183
D.1	Event Selection Systematic Errors for the dAVertex and dAPeriph Data Sets	185
D.2	Track Selection Systematic Errors for the ppVertex Data Set	186
D.3	Particle Identification Systematic Errors for the ppVertex Data Set .	187
D.4	Other Systematic Errors for the ppVertex Data Set	188

LIST OF FIGURES

1.1	Diagram of quark confinement.	6
1.2	QCD phase diagram of nuclear matter.	7
1.3	Timeline of the expansion of the universe.	8
1.4	Timeline of a relativistic heavy ion collision.	12
2.1	Schematic diagram of the alternating gradient synchrotron and relativistic heavy ion collider.	23
2.2	Diagram of the PHOBOS detector.	26
2.3	Components of an individual paddle module.	27
2.4	Schematic diagram of a Paddle Counter.	28
2.5	Time difference distribution of events in which both Paddle Counters fire.	29
2.6	Summed energy of the negative Paddle Counter modules for d+Au collisions (Au side).	29
2.7	Front view of the T_0 trigger counters and mounting frame.	31
2.8	Components of a Čerenkov module.	32
2.9	Drawing of a Čerenkov Counter around the beam pipe.	33

2.10	Diagram of the position of the Zero Degree Calorimeters and a view of the positions of protons and neutrons along the transverse x-axis at the position of the ZDC's.	34
2.11	Zero Degree Calorimeter module assembly.	35
2.12	Schematic diagram of the Spectrometer Trigger.	37
2.13	Schematic diagram of the Octagon and Vertex Detectors.	39
2.14	Schematic diagram of a Ring Multiplicity Counter.	42
2.15	Schematic diagram of the negative Proton Calorimeter and an indi- vidual Proton Calorimeter module.	43
2.16	Simulation of the separation of spectator and recoil protons and neu- trons at $z = 18$ m	44
2.17	Schematic diagram of the Spectrometer.	45
2.18	Spectrometer acceptance as a function of transverse momentum and rapidity.	47
2.19	Schematic diagram of the PHOBOS magnet.	48
2.20	Map of the y-component of the magnetic field.	49
2.21	Diagram of an assembled Time-of-Flight Wall.	50
3.1	Timing diagram for the Paddle and T_0 Counters in the d+Au collision system.	54
3.2	T0N collision time plotted versus T0P collision time.	58
3.3	Distribution of z-vertex positions for all HIJING Monte-Carlo parti- cles that produce tracks in the spectrometer.	60

3.4	The distributions of the difference between the Monte-Carlo vertex and the experimental vertex.	61
3.5	Mean x and y positions of the beam orbit for each data set.	64
3.6	The average number of straight tracks found per selected event for the dAVertex data set.	68
3.7	The number of times each run deviates by 3 or more sigma from the mean value of the data quality variables plotted versus run number for the dAPeriph data set.	68
3.8	The geometry of a d+Au collision.	70
3.9	The energy distribution in the Ring Multiplicity Counters for the d+Au collision system.	71
3.10	The HIJING Monte-Carlo energy distribution in the Ring Multiplicity Counters plotted versus the number of collisions N_{coll} in a d+Au collision.	72
3.11	The experimental dAVertex E_{Ring} distribution divided into centrality bins.	73
3.12	Number of binary collisions, N_{coll} , versus the total energy deposited in the Proton Calorimeter.	75
3.13	Experimental and scaled toy Monte-Carlo energy distributions for the Proton Calorimeter modules.	76
4.1	Hits recorded in the spectrometer for a d+Au collision event.	79

4.2	The y-component of the magnetic field (at $y = 0$) in the region of the spectrometer.	81
4.3	The reconstructed x and y collision vertex positions for a subset of the d+Au data set.	82
4.4	The reconstructed straight tracks found in a d+Au collision event. . .	84
4.5	The angles θ_0 , θ and α defined for a hit pair in a d+Au collision event.	85
4.6	The reconstructed matched tracks found in a d+Au collision event. .	88
4.7	The ratio of the reconstructed and true momenta versus true momentum for simulated protons.	92
4.8	Fit probability distribution for tracks reconstructed from the data in the negative and positive spectrometer arms.	94
4.9	Track reconstruction efficiency plotted as a function of p_T	95
4.10	The number of tracks found per event in d+Au and p+p collisions. .	96
4.11	The momentum resolution of the track reconstruction plotted as a function of momentum for the PR03 tracking procedure.	97
4.12	The momentum resolution of the track reconstruction plotted as a function of momentum for the PR04 tracking procedure.	97
5.1	Theoretical Bethe-Bloch prediction of the distribution of energy deposition versus particle momentum.	104
5.2	The average truncated energy loss expressed versus reconstructed particle momentum for the d+Au data compared to the theoretical Bethe-Bloch predictions.	104

5.3	Distribution of the average truncated energy loss as a function of reconstructed particle momentum for the d+Au data set with particle identification cuts applied.	105
5.4	Spectrometer acceptance as a function of transverse momentum and rapidity.	107
5.5	Distribution of the average truncated energy loss as a function of reconstructed particle momentum for the region in which pions and electrons can be resolved for the d+Au data set.	108
5.6	Distribution of the average truncated energy loss as a function of reconstructed particle momentum for the region in which pions and electrons can be resolved in d+Au HIJING Monte-Carlo events. . . .	109
6.1	The fit probability of tracks in beam orbit region 0 of the dAVertex data set.	115
6.2	The distribution of the distance of closest approach of true HIJING Monte-Carlo tracks to the beam orbit.	116
6.3	The distribution of the distance of closest approach of tracks to the beam orbit for Monte-Carlo and data events.	116
6.4	The z-vertex distribution observed in beam orbit region 0 of the ppVertex data set.	119
6.5	The ratio of the z-vertex distributions for B^+ and B^- events in beam orbit region 0 of the ppVertex data set.	119

6.6	The difference in the average transverse momenta of π^- and π^+ particles that bend away from the beam pipe as a function of centrality for the dAVertex data set.	123
6.7	Magnetic field strength as a function of time for the dAVertex data set.	124
7.1	The reconstruction efficiency of primary protons and feed-down protons generated from primary Λ particles as a function of transverse momentum.	134
7.2	$br * \epsilon_{acc}$ as a function of transverse momentum.	134
7.3	$br * \epsilon_{acc}$ as a function of transverse momentum fit with the functional form shown in Eq. 7.15.	135
7.4	Ratio of secondary protons to primary protons in simulated d+Au HIJING Monte-Carlo events.	143
7.5	Secondary to primary ratio as a function of p_T for pions and kaons in simulated minimum bias d+Au HIJING Monte-Carlo events.	145
7.6	The proton absorption fraction as a function of transverse momentum for negative and positive magnetic field polarities.	147
7.7	The antiproton absorption fraction as a function of transverse momentum for magnetic field polarity negative and magnetic field polarity positive.	148
8.1	Relative ratio plots for pions, kaons and protons for the Track Selection Systematic DCA Cut for the dAVertex data set.	156

9.1	Particle ratios plotted versus centrality for the d+Au and p+p 200 GeV collision systems.	160
9.2	The antiproton to proton ratio plotted versus number of collisions $\langle \nu \rangle$ for simulated and experimental 200 GeV d+Au collisions.	161
9.3	The $\langle \bar{p} \rangle / \langle p \rangle$ ratio reported by all of the RHIC experiments for a variety of collision species and energies.	163
9.4	Particle ratios measured in the PHOBOS detector plotted versus centrality for the d+Au, p+p and Au+Au collisions at 200 GeV.	164
9.5	Antiproton to proton ratio near midrapidity plotted versus center-of-mass collision energy for p+p, central Pb+Pb and central Au+Au collisions.	165

Chapter 1

Introduction

The study of relativistic heavy ion collisions is motivated by fundamental questions concerning the properties and interactions of strongly interacting matter. Quarks and gluons are the building blocks of nuclear matter. Their interactions are governed by the strong force which is described by the principles of Quantum Chromodynamics, QCD. Understanding the properties and behavior of quarks and gluons will shed light on the underlying principles which govern matter in the physical universe and possibly provide insight into the evolutionary path that the universe has followed.

Relativistic heavy ion collisions provide the mechanism by which it is possible to study strongly interacting matter in the laboratory setting. In these collisions nuclear matter is subjected to extreme temperatures and densities in order to probe the phase diagram of nuclear matter. The Relativistic Heavy Ion Collider (RHIC)

located at Brookhaven National Laboratory is designed to provide collisions between two beams of nuclei that have been accelerated to a maximum center-of-mass energy of $\sqrt{s_{NN}} = 200$ GeV. It has been predicted that the energy densities achieved in 200 GeV Au+Au collisions are sufficient to create a quark-gluon plasma (QGP) [1]. The objective of the experiments at RHIC is to identify and characterize the QGP phase of nuclear matter. In order to do this, it is necessary to study smaller collision systems in which the quark-gluon plasma is not expected to be formed as a reference. For this reason RHIC also provides collisions between 200 GeV d+Au and p+p nuclei.

The PHOBOS experiment, located at the Relativistic Heavy Ion Collider, is designed to measure global characteristics of the system created in a heavy ion collision. One of the distinctive properties of a collision is the relative yields of antimatter and matter produced. As the net baryon density of the collision system approaches zero, the ratio of antimatter to matter should approach one. In addition, the relative yields of antiprotons and protons produced in a collision can be used to study the interplay of baryon number transport and antibaryon-baryon pair production processes. This thesis presents a study of the antiparticle to particle ratios in the d+Au and p+p collision systems at $\sqrt{s_{NN}} = 200$ GeV. The collision energy and centrality dependence of the ratios are investigated and the ratios are compared with results obtained from the Au+Au collision system.

Table 1.1: Quarks and their Physical Properties

Name	Symbol	Charge	Rest Mass (MeV/c ²) [2]
Up	u	+2/3	1.5-4
Down	d	-1/3	4-8
Strange	s	-1/3	80-130
Charm	c	+2/3	1150-1350
Bottom	b	-1/3	4100-4400
Top	t	+2/3	174300 ± 5100

1.1 Standard Model & QCD

The Standard Model provides a description of the fundamental particles and forces that govern matter. Within the framework of the Standard Model quarks and leptons are identified as elementary particles. Each quark and lepton has an antimatter partner referred to as antiquarks and antileptons. Quarks are spin 1/2 fermions that exist in the bound state as hadrons. Table 1.1 provides a list of quarks and their physical properties. Quarks and antiquarks have never been observed in isolation. Instead, in the ground state they exist in groups of 2 as mesons and groups of 3 as baryons. Normal nuclear matter is composed of protons and neutrons whose valence quark composition is uud and udd , respectively. An antiproton is the antimatter equivalent of the proton and has a quark composition of $\bar{u}\bar{u}\bar{d}$, where a bar above the quark symbol denotes an antiquark. Pions and kaons are mesons and are composed of a quark and an antiquark. Positively charged pions have the composition $u\bar{d}$ and positively charged kaons have the composition $u\bar{s}$. Analogously, negatively charged pions and kaons have the quark structure $\bar{u}d$ and $\bar{u}s$, respectively.

Leptons are also fermions, but appear to be point-like and contain no under-

Table 1.2: Leptons and their Physical Properties

Name	Symbol	Charge	Rest Mass (MeV/c ²) [2]
electron neutrino	ν_e	0	< 0.003
electron	e	-1	0.511
muon neutrino	ν_μ	0	< 0.19
muon	μ	-1	105.6
tau neutrino	ν_τ	0	< 18.2
tau	τ	-1	1777

Table 1.3: Forces and their Properties

Name	Relative Strength	Range	Exchange Particle
gravity	10^{-38}	∞	graviton
weak	10^{-13}	$< 10^{-18}$ m	Z^0, W^+, W^-
electromagnetic	10^{-2}	∞	photon
strong	1	10^{-14} m	gluon

lying substructure. In contrast to quarks, leptons do not bind together, but instead appear individually in nature. Table 1.2 contains a list of leptons and their physical properties.

The Standard Model also accounts for the forces that govern the interactions between particles. These forces are the electromagnetic, weak and strong forces. Each force is conveyed by a distinct mediator or exchange particle. Table 1.3 lists each of the forces, their relative strengths and exchange particles. The electromagnetic force can be either attractive or repulsive and acts between charged objects. The weak force is responsible for radioactive decay and the strong force binds quarks together in hadrons and nucleons together within the nucleus. The gravitational force, which acts as an attractive force between two massive bodies, has yet to be incorporated into the Standard Model.

The properties of the strong force are described by the theory of Quantum Chromodynamics. Within this theory, the property associated with the interaction is referred to as *color* and is analogous to the electric charge in Quantum Electrodynamics. Each parton, defined as a quark or gluon, carries a color charge, either red, green or blue. Because gluons themselves carry color they can interact with each other, unlike photons which are electrically neutral. This phenomenon has profound consequences on the behavior of strongly interacting matter.

According to the principles of QCD, the coupling between color carriers increases with distance. This leads to the properties of both *asymptotic freedom* and *confinement*. At very small distances the QCD potential is weak enough that quarks behave as if they are unbound or asymptotically free. In contrast, at large distances the QCD potential becomes large and confines quarks within their respective hadrons. As a consequence of confinement, it is not possible to separate bound quarks. The energy necessary to pull a $q\bar{q}$ pair apart is greater than the rest mass of the pair; therefore, as energy is introduced into the system a new $q\bar{q}$ pair will be produced from the vacuum instead of separating the original pair. A cartoon diagram of this process is shown in Fig. 1.1, where the lines between the $q\bar{q}$ pairs represent the color force.

It has been postulated that under the conditions of extreme temperature and/or density it could be possible to achieve a state of asymptotic freedom. Within this state quarks and gluons would be deconfined from hadrons and exist in a quark-gluon plasma. The conditions necessary to achieve this state are shown in the QCD phase diagram of nuclear matter, Fig 1.2, which describes the states of strongly in-

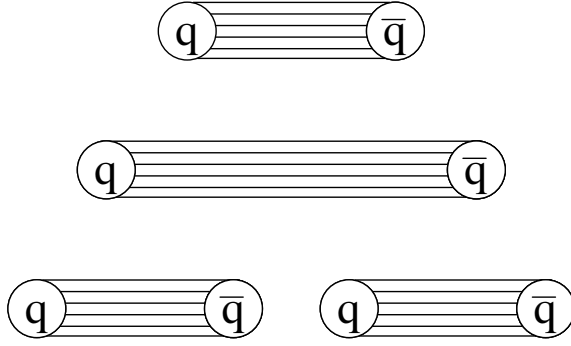


Figure 1.1: Diagram of quark confinement. The lines between the $q\bar{q}$ pairs represent the color force.

teracting matter under varying conditions of temperature and pressure. The vertical axis represents temperature and the horizontal axis is the baryochemical potential μ_B of the system. The baryochemical potential is related to the baryon density of stressed nuclear matter compared to that of normal nuclear matter. At low values of temperature and baryochemical potential quarks are confined within hadrons in the form of a hadron gas. Conversely, at high values of temperature or μ_B the conditions are sufficient for a transition to the quark-gluon plasma phase. The wide band between the hadronic gas and QGP phases represents the uncertainty in the location of the phase transition.

Measurements made in two separate regimes of the phase diagram provide insight into the properties of strongly interacting matter. Neutron stars are believed to exist in the low temperature and high baryochemical potential regime of the QCD phase diagram. They possess a mass that is roughly equivalent to that of the Sun, yet have a radius of only 10's of kilometers. The extreme density at the core of a neutron star is believed sufficient for the neutrons to overlap. The other extreme

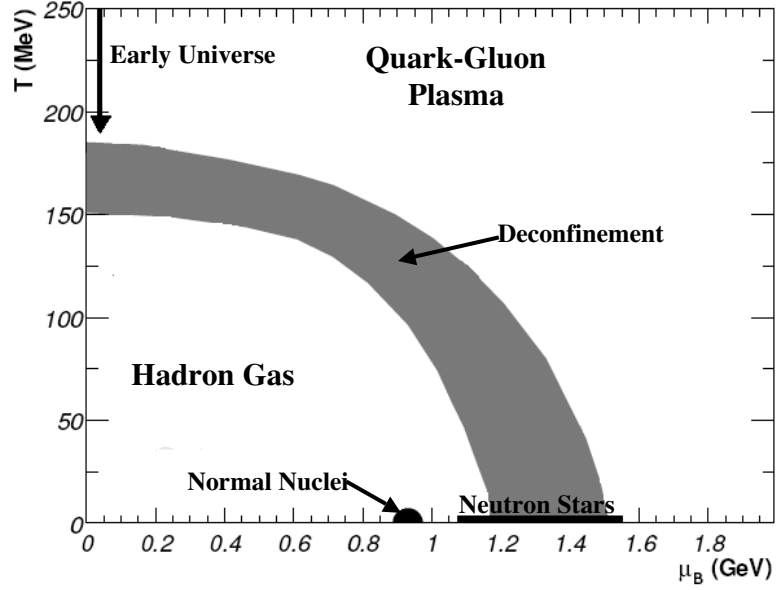


Figure 1.2: QCD phase diagram of nuclear matter. The wide band between the hadronic gas and QGP phases represents the uncertainty in the location of the phase transition.

of the QCD phase diagram, the region of vanishing baryochemical potential and high temperature, is believed to describe the properties of the state of the universe at 10^{-6} s after the Big Bang. The theory of the Big Bang postulates that at one time all matter and energy in the universe was compressed into a single point which subsequently exploded. Some of the energy released by the explosion was converted into matter that existed in the quark-gluon plasma phase. As the system expanded, it cooled and condensed into a hadron gas. Figure 1.3 shows the time-line of the expansion of the universe. Since the time of the Big Bang the universe has continued to expand and cool. Now relativistic heavy ion collisions may provide a means of achieving the conditions found when the universe was only 10^{-6} s old. It is through this mechanism that it is possible to probe the fundamental principles of Quantum Chromodynamics.

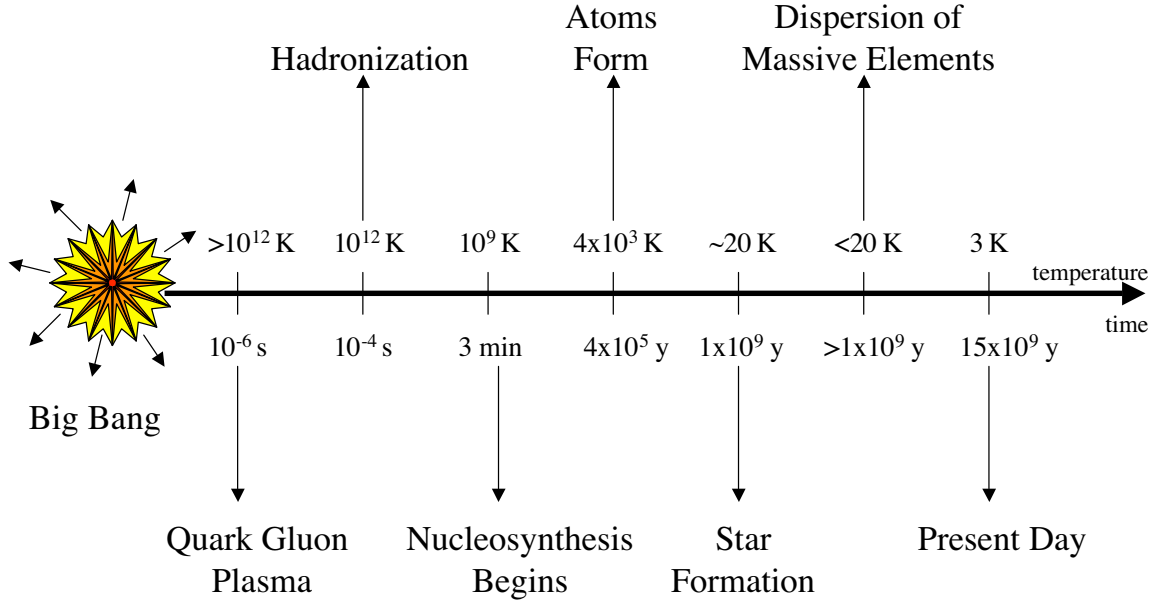


Figure 1.3: Timeline of the expansion of the universe.

1.2 Relativistic Heavy Ion Collisions

Relativistic heavy ion collisions are used to attempt to recreate the quark-gluon plasma in the laboratory setting where the properties of the system and phase transition can be studied. This is the goal of experiments being conducted at the Relativistic Heavy Ion Collider at Brookhaven National Laboratory (BNL). At RHIC collisions between nuclei have been studied up to a maximum center-of-mass energy of $\sqrt{s_{NN}} = 200$ GeV. The conditions created in these collisions probe the high temperature and low baryochemical potential regime of the QCD phase diagram shown in Fig. 1.2. In addition to colliding Au+Au, RHIC can also accelerate low mass nuclei. Collisions between p+p beams and d+Au beams provide valuable reference information necessary to interpret the results obtained from the Au+Au collisions.

1.2.1 Historical Perspective

The experiments being conducted at RHIC are the most recent in a series of studies designed to investigate the QGP. Experiments at the Super Proton Synchrotron at CERN (SPS) and the Alternating Gradient Synchrotron at BNL (AGS) collided both light and heavy nuclei such as, oxygen, silicon, sulfur, lead and gold. The experiments at the SPS and AGS were fixed target experiments in which a beam of nuclei is accelerated and directed towards a stationary target. The maximal beam energies achieved at the AGS and SPS were 10.8 GeV/nucleon and 200 GeV/nucleon, respectively. In the center-of-mass frame these energies are equivalent to only $\sqrt{s_{NN}} = 4.6$ GeV at the AGS and $\sqrt{s_{NN}} = 17.8$ GeV at the SPS. Due to the limited collision energy available, experiments at both of these facilities sampled regions of the QCD phase diagram with higher baryochemical potential than is being studied at RHIC.

The RHIC facility includes four independent heavy ion experiments PHOBOS, PHENIX, STAR and BRAHMS. Each of these experiments is optimized to study the properties of high energy Au+Au collisions in a complementary way. The PHENIX and STAR experiments are both large scale detectors and are composed of a large number of sub-detectors. PHENIX contains two central arms, two forward muon arms and event characterization detectors. Each central arm sits within a magnetic field and contain the following sub-detectors: a drift chamber, pad chambers, Ring Imaging Čerenkov detectors, Time Expansion Chamber, time-of-flight detector and an electromagnetic calorimeter. The forward muon arms also sit within a

magnetic field and are composed of muon tracker and muon identifier sub-detectors. Beam-beam counters, Zero Degree Calorimeters, a forward calorimeter and a Multiplicity Vertex detector are used for event characterization. The Phenix experiment is designed to measure direct probes of the collisions, such as electrons, muons and photons.

The STAR experiment consists of midrapidity and forward Time Projection Chambers, a Ring Imaging Čerenkov detector, an electromagnetic calorimeter, a silicon vertex tracker, a silicon strip detector, a time-of-flight detector, a photon multiplicity detector, a forward pion detector, Beam-Beam Counters and Zero Degree Calorimeters. With these tools the STAR experiment is optimized to study hadronic probes of the collisions, such as particle spectra and strangeness. Continuous modifications and upgrades to the two large experiments are designed to extend the capabilities of each detector system. These descriptions represent the state of the detector systems in 2004.

The BRAHMS and PHOBOS experiments are small scale detectors. The BRAHMS experiment has midrapidity and forward spectrometers, Beam-Beam Counters, a Multiplicity detector and Zero Degree Calorimeters. These detectors are used to examine particle production in the forward and midrapidity regions. The PHOBOS experiment is the subject of this thesis. A detailed explanation of the components of the detector is provided in Chapter 2 and an overview of the physics objectives can be found in Sec. 1.3.

The next generation relativistic heavy ion collider is already under construction. The Large Hadron Collider (LHC) located at CERN will provide heavy ion

collisions at a maximum energy of $\sqrt{s_{NN}} = 5.5$ TeV. Currently, three LHC experiments which propose to study heavy ion collisions are under construction: ALICE, ATLAS and CMS. These experiments will continue the tradition of probing strongly interacting matter under extreme conditions.

1.2.2 Collision Evolution

A relativistic heavy ion collision can be divided into five separate time frames. These periods correspond to the initial impact, parton production, hadronization, chemical freeze-out, and thermal freeze-out stages, and are depicted in Fig. 1.4. When nuclei are accelerated to relativistic energies they experience Lorentz contraction. As a result, from the center-of-mass reference frame of a collision the nuclei appear as thin disks instead of as spherically symmetric balls. The initial impact of the two nuclei is characterized by the impact parameter b , which is the transverse distance between the centers of the two colliding nuclei. This is commonly referred to as the *centrality* of the collision. A collision in which the overlap between the two nuclei is small is referred to as a *peripheral* collision and a collision in which the overlap between the nuclei is large is a *central* collision. Section 3.4 provides an explanation of how collision centrality is determined in the PHOBOS experiment.

In a collision between two nuclei all of the constituent nucleons do not necessarily participate in the collision. Those nucleons that are not involved in the collision continue to travel along the axis of the beam and are referred to as *spectators*. Nucleons that are involved in the collision are identified as *participants*.

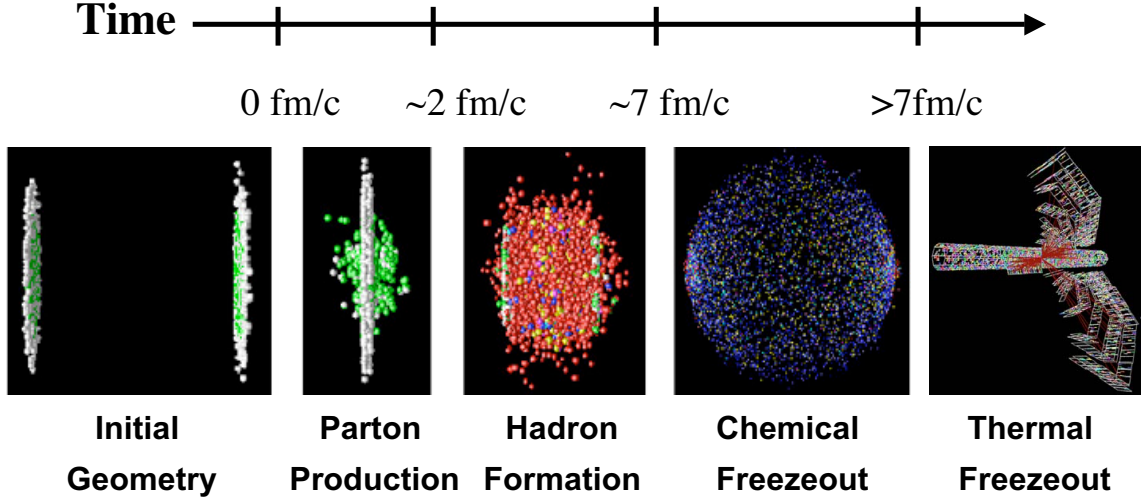


Figure 1.4: Timeline of a relativistic heavy ion collision. The images associated with the Initial Geometry, Parton Production, Hadron Formation and Chemical Freeze-out stages of a collision are simulated representations of the collision system. The Thermal Freeze-out representation is an image of a single collision event in the PHOBOS detector.

Immediately after impact the collision system exists in a state of pre-equilibrium. The participants deposit their original kinetic energy into the collision system and some of this energy is used for parton production. If the energy density achieved by the collision is sufficient, it is possible that a quark-gluon plasma is formed. Parton rescattering can lead to thermal equilibrium during this stage. Once equilibrium is achieved the common thermodynamic properties of temperature and pressure can be used to characterize this stage of the collision process.

As the system evolves the pressure causes it to expand and cool. At the transition temperature hadronization occurs and the partons become bound within hadrons. Inelastic collisions between the newly formed hadrons continue to occur until the system cools to the chemical freeze-out point. This is when the relative yields of each particle species produced becomes fixed. Finally, elastic collisions

between the hadrons cease at the thermal freeze-out point. It is only after thermal freeze-out that the particles produced in the collision can be measured by the detectors. Measurements made by relativistic heavy ion experiments are designed to probe the stages of a heavy ion collision in an attempt to better understand the collision dynamics and subsequent evolution of the collision system.

1.2.3 Experimental Observables

To study the properties of heavy ion collisions it is necessary to identify experimental measurements that can provide a window into the properties of the collision system. This section provides examples of measurable quantities that probe each stage of the collision evolution and should not be considered to be an exhaustive list of experimental observables. The measurements identified each contribute to the overall understanding of the dynamics of a heavy ion collision and the properties of the state of matter that is produced.

The centrality of the initial impact of a collision can be determined by examining the multiplicity of the collision [3]. Multiplicity is defined as the total yield of produced particles. In central collisions many nucleons participate in the collision, thus the energy available for particle production is high. Conversely, in peripheral collisions few nucleons participate in the collision and little energy is available for particle production. As a result, the collision multiplicity is proportional to the degree of overlap between the two colliding nuclei.

In the parton production stage hard collision processes occur between partons

that result in large momentum transfers ($> 10 \text{ GeV}/c$) and high momentum quark pairs are produced. These quarks are able to travel out of the interaction volume and fragment to produce hadronic jets. Jets can be experimentally distinguished as clusters of particles in phase space. Jets provide a useful probe of the pre-equilibrium stage because the high momentum quarks experience relatively few interactions as they leave the interaction volume. If the interaction volume consists of a strongly interacting medium or QGP, jet-quenching could occur in which the jet experiences rescattering in the medium and loses momentum [4, 5]. This is believed to be a potential signal of QGP formation.

The measurement of elliptic flow can be used to determine if thermal equilibrium is achieved during the parton production stage of a collision [6, 7]. Elliptic flow examines the azimuthal distribution of produced particles. The magnitude of the flow signal is sensitive to the time needed for the collision system to equilibrate. A large flow signal indicates an early equilibration time in the evolution of the collision system.

The hadronization and chemical freeze-out stages of a collision can be studied by measuring the yields of identified particles. The ratios of the yields of antiparticles to particles provide insight into the relative amount of matter and antimatter created in the collision. In conjunction with statistical models, the antiparticle to particle ratios can be used to determine the baryochemical potential of the system created by a heavy ion collision [8]. The ratio of antiprotons to protons probes the relative yields of measured baryons resulting from baryon number transport and antibaryon-baryon pair production processes. The antiparticle to particle ratios and baryon

number transport are further discussed in Sec. 1.3.

Finally, the properties of the collision system at the time of thermal freeze-out can be determined using Hanbury-Brown-Twiss interferometry (HBT) [9]. HBT studies measure the 3-dimensional size of the system at thermal freeze-out. The HBT radii can be used to estimate the time duration of the collision system.

1.2.4 Theoretical Models

The dynamics of a heavy ion collision are very complicated and not readily calculable directly. For this reason, models are used to describe the interactions of colliding nuclei. Models provide theoretical predictions of the collision dynamics that are based upon previously reported experimental data. Used in conjunction with a detector response simulation package GEANT [11], predictions of experimental observables can be obtained from the models. These predictions can be compared with experimental results to gain insight into the physical processes that contribute to the collision system. The following sections describe three collision simulation packages that are used in this thesis.

1.2.4.1 HIJING

The Heavy Ion Jet INteraction Generator (HIJING) [12, 13] is based upon perturbative QCD physics and, in its default configuration, includes no novel physics phenomena. Specifically, HIJING does not account for QGP formation or thermal equilibration of the interaction medium. This allows it to be used as a reference by which the presence of new physics in experimental data can be judged. HIJING

is a partonic transport model; therefore, the collision dynamics are simulated via parton-parton interactions. Hard collisions dominate at momenta above 2 GeV/c and soft interactions occur below 2 GeV/c. Parton production from soft collisions is simulated using diquark-quark strings. Hard processes generate multiple mini-jets that also contribute to parton production. Partons are converted to hadrons using a string fragmentation model. Options within the HIJING model allow for the inclusion of parton shadowing and jet quenching.

1.2.4.2 AMPT

The AMPT model [14, 15] is a cascade model that includes both partonic and hadronic interactions. The initial collision conditions are determined by the HIJING model including a Woods-Saxon radial shape for the colliding nuclei and nuclear shadowing through the mechanism of gluon recombination. Parton-parton collisions are simulated using a parton cascade model [16, 17] and the partons are converted to hadrons in accordance with a string fragmentation model [18, 19, 20]. Subsequent hadronic interactions are simulated using a relativistic transport model [21] that includes baryon-antibaryon production from meson interactions.

1.2.4.3 RQMD

The particle interactions of collision events generated by the Relativistic Quantum Molecular Dynamics model (RQMD) [22] are fundamentally different from those of the HIJING and AMPT models. Instead of simulating the collision in terms of parton-parton interactions, RQMD is a hadronic transport model. The incident

nucleons interact by way of strings and resonances which subsequently decay to produce particles. At large beam energies (> 10 AGeV) the collision can no longer be modeled as a series of separate hadron or resonance collisions and it is necessary to incorporate sub-hadronic processes. This is done using cross-sections from the additive quark model [23, 24, 25]. RQMD also includes the effects of secondary rescattering and mean-field interactions.

1.3 Thesis Overview

The PHOBOS detector was designed to measure the global properties of the collision systems created at the Relativistic Heavy Ion Collider. Table 1.4 provides a list of terminology and definitions relevant to these studies. To maximize the probability of detecting new physics phenomena the detector is situated near midrapidity, where the highest energy densities are expected to occur. Furthermore, PHOBOS is optimized to measure charged particles with low transverse momenta over a broad range of pseudorapidity. Particle tracking and identification capabilities allow for the measurement of the yields of primary produced pions, kaons, and protons within the acceptance of the detector.

In addition to high energy Au+Au collisions, experiments at RHIC have also studied asymmetric (d+Au) and light ion (p+p) collisions. The energy densities achieved in these collisions are much lower than in the Au+Au collision system and are not expected to be sufficient to result in a transition to the quark-gluon plasma phase. However, measurements of the properties of these collisions provide an im-

Table 1.4: Terminology and Definitions

Term	Definition
Rapidity, y	$y = \frac{1}{2} \ln \left(\frac{E+p_{ }}{E-p_{ }} \right)$
Pseudo-rapidity, η	$\eta = -\ln \left[\tan \left(\frac{\theta}{2} \right) \right]$
Midrapidity	Approximately $-1 < \eta < 1$
Longitudinal Momentum, $p_{ }$	Component of momentum parallel to the beam
Transverse Momentum, p_T	Component of momentum perpendicular to the beam

portant baseline for evaluating the results obtained from more complex heavy ion collisions. They are particularly valuable for evaluating the influence of interactions within the dense medium formed after the collision, or final state interactions, on the physical observables of the collision system.

1.3.1 Antiparticle to Particle Ratios

The objective of this thesis is to measure the ratio of the yields of antiparticles and particles for primary charged pions, kaons, and protons in d+Au and p+p collisions at $\sqrt{s_{NN}} = 200$ GeV. These ratios are of interest because comparisons of d+Au and Au+Au data suggest that the conditions in Au+Au collisions are very different from those observed in the d+Au system [26, 27, 28, 29]. Whether these different conditions influence the particle ratios is explored by measuring the ratios in d+Au and p+p collisions and comparing the results with those obtained from Au+Au collisions.

Results from Au+Au collisions [30, 31] show that the $\langle K^- \rangle / \langle K^+ \rangle$ and $\langle \bar{p} \rangle / \langle p \rangle$ ratios are consistent with thermal models, which assume the collision system has

achieved thermal equilibrium. This suggests that final state interactions dominate. In d+Au and p+p collisions little reinteraction is expected; therefore, the particle ratios should reflect the initially produced particle yields. Furthermore, the relative yields of antiprotons and protons near midrapidity depend largely on the dynamics of baryon-antibaryon pair production and baryon number transport in nucleus-nucleus collisions. The rate of pair production can depend on the state of the matter created, see references in [32]. Thus, the influence of baryon number transport, baryon production, and final state interactions can be investigated by comparing results from p+p, d+Au and Au+Au collision systems.

1.3.2 Baryon Number Transport

Primary protons measured in the PHOBOS detector are generated via two separate mechanisms. The first mechanism, pair production, results in equal yields of protons and antiprotons and is the only pathway by which primary antiprotons are formed. The second mechanism, baryon number transport, influences only the measured proton yield. A proton from the original colliding nuclei is considered to be transported if its direction of motion is shifted away from the axis of the beam. To be tracked and identified in the PHOBOS detector the proton must be transported to midrapidity or $\theta \sim 90^\circ$ with respect to the axis of the beam. Baryon number transport results in a net increase of protons detected relative to antiprotons and reduces the measured $\langle \bar{p} \rangle / \langle p \rangle$ ratio. A net baryon free region exists at midrapidity when the collision energy of the incident nuclei is sufficient to not allow the trans-

port of protons into this region. This condition would result in a measured $\langle\bar{p}\rangle/\langle p\rangle$ ratio of 1.0.

In Au+Au collisions at RHIC energies the ratio of $\langle\bar{p}\rangle/\langle p\rangle$ increases from 0.6 to 0.8 as the collision energy increases from 130 GeV to 200 GeV, and shows a weak dependence on centrality and p_T [30, 31, 33, 34, 35, 36, 37, 38, 39]. These results imply that baryon-antibaryon pair production is larger than baryon number transport and yet there is still finite baryon number transport [32].

To compare particle ratios measured in different collision systems, the number of collisions experienced by each participating nucleon ν is used as a measure of collision centrality, see Sec. 3.4. Based on lower energy data, the expectation is that the more collisions a participating nucleon suffers, the greater the baryon number transport to midrapidity [40, 41]. This results in the reduction of the measured $\langle\bar{p}\rangle/\langle p\rangle$ ratio. For central Au+Au collisions (12% most central events [31]) each participating nucleon suffers on average 5.2 collisions. In d+Au collisions, when looking in the deuteron hemisphere, ν can be defined using the number of participating nucleons from the deuteron. Over the range of centrality studied in this thesis, $\langle\nu\rangle$ varies from 2 to 8 in the d+Au system. Measurement of the antiparticle to particle ratios in the p+p collision system provides insight into the simplest possible nuclear system, where each participating nucleon experiences only 1 collision. The data presented in this thesis allows for a comparison of the relative magnitude of the baryon number transport per produced baryon over a large range in ν and collision environments.

Chapter 2

The PHOBOS Experiment

The PHOBOS experiment was designed to observe the global event characteristics of heavy ion collisions produced at the Relativistic Heavy Ion Collider (RHIC) located at Brookhaven National Laboratory in Upton, New York. The PHOBOS detector is comprised of multiple elements ranging from silicon pad detectors to plastic scintillator counters. This chapter reviews each of the components of the detector system, as well as the RHIC facility. The PHOBOS collaboration consists of approximately 60 individuals from 8 member institutions and 3 countries. Appendix A contains a list of current collaboration members and institutions.

2.1 Relativistic Heavy Ion Collider

The Relativistic Heavy Ion Collider was designed to achieve a maximum collision energy of $\sqrt{s_{NN}} = 200$ GeV for heavy nuclei such as Au, which surpasses that achieved by previous heavy ion colliders. In order to achieve this energy, the RHIC facility relies upon several preexisting structures, the Tandem Van de Graaff accelerator, the Booster synchrotron, and the Alternating Gradient Synchrotron, AGS. Each of these facilities is used as a stepping stone as the beam of heavy ions is accelerated to its maximum energy. A schematic diagram of the entire RHIC facility is shown in Fig. 2.1.

The Au ions, Au^{+79} , that circulate in the RHIC ring begin their journey in the pulsed cesium sputter ion source as Au^{-1} anions. The ions are accelerated twice through a potential of 14 MV in the Tandem Van de Graaff generator where they are stripped of 12 electrons by a thin carbon stripping foil while being accelerated and an additional 21 electrons when exiting the generator [42]. The resulting Au^{+32} ions are transported to the Booster synchrotron through the Heavy Ion Transfer Line and are subsequently accelerated to an energy of 1 GeV/nucleon. After being accelerated, the ions are stripped of 45 additional electrons and are then injected into the Alternating Gradient Synchrotron where they are further accelerated. Upon exiting the AGS, the beam consists of pulses of Au^{+77} ions with an energy of 10 GeV/nucleon. The beam is directed towards the AGS-to-RHIC transfer line where the two remaining electrons are removed before injection into RHIC. After entering RHIC, the ions are accelerated to their final energy of 100 GeV/nucleon. Within RHIC

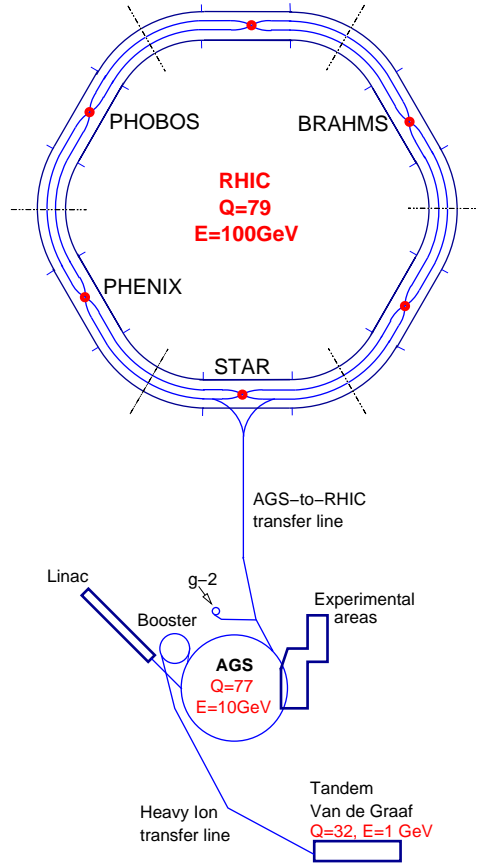


Figure 2.1: Schematic diagram of the alternating gradient synchrotron, AGS, and relativistic heavy ion collider, RHIC.

Table 2.1: RHIC Beam Energies and Collision Systems for Each Run

Run	Date	Energy $\sqrt{s_{NN}}$ (GeV)	Collision System
Comissioning Run 2000	March - July 2000	56, 130	Au+Au
Physics Run 2000	July - September 2000	130	Au+Au
Physics Run 2001	July 2001 - January 2002	200 200	Au+Au p+p
Physics Run 2003	December 2002 - May 2003	200 200	d+Au p+p
Physics Run 2004	December 2003 - May 2004	200 200	Au+Au p+p

two beams of ions are simultaneously accelerated in opposite directions in two concentric rings. The beams cross one another at six interaction areas denoted as red points in Fig. 2.1. Currently only four of the interaction areas are occupied by experiments. Colliding two beams of ions provides the advantage over fixed target experiments that the center-of-mass frame of the collision remains at rest.

One of the strengths of the RHIC facility and experiments is the ability to study a variety of different collision systems and collision energies. Table 2.1 outlines the different running conditions implemented thus far. The data analyzed in this thesis was collected during the 2003 running period and thus encompasses the d+Au and p+p collision systems.

2.2 The PHOBOS Detector

The PHOBOS detector is located at the 10 o'clock position of the RHIC ring and is the only RHIC experiment that sits in the accelerator tunnel. A diagram of the detector system as it was positioned for the 2003 Physics Run is shown in Fig. 2.2.

Each of the individual components performs a task that is critical to the overall performance of the detector. The sub-detectors can be grouped into four principal categories based upon their functionality: Event Triggering, Event Vertex Determination, Centrality and Multiplicity Determination, and Particle Identification.

2.2.1 Event Triggering

The trigger detectors are responsible for deciding which events are recorded by the experiment. This decision is made as the collisions are occurring and initiates the readout of all of the other sub-detectors in the experiment. The PHOBOS detector has five different types of trigger counters: Paddles, T_0 's, Čerenkovs, Zero Degree Calorimeters and the Spectrometer Trigger. The data used in this analysis was collected using a combination of the Paddle and T_0 triggers. The specific details of the event triggering for this data set can be found in Sec 3.1.

2.2.1.1 Paddle Trigger Counters

The PHOBOS detector includes two sets of Paddle Trigger Counters that are arrays of 16 individual modules each [43]. A module consists of a plastic scintillator (Bicron, BC-400), a light guide (Bicron, BC-800), a hybrid photomultiplier tube (Hamamatsu, H1151-2), and a magnetic shield. The physical dimensions of each module are shown in Fig. 2.3. The modules are mounted around the beam pipe in a ring, as shown in Fig. 2.4. In the coordinate system of the experiment, one array of paddle modules sits at $+3.21\text{ m}$ from the nominal interaction point along the axis of the beam, z-axis, while the other array is positioned symmetrically at $z = -3.21\text{ m}$.

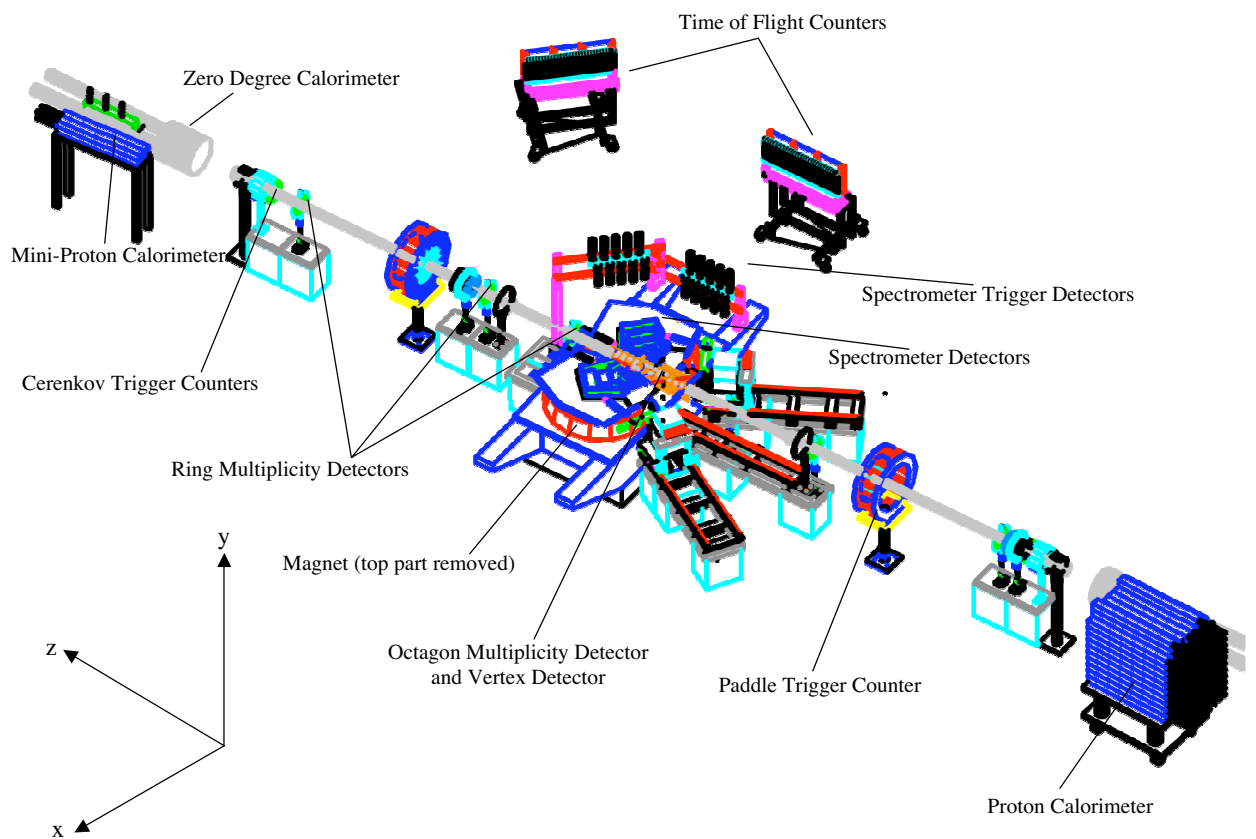


Figure 2.2: Diagram of the PHOBOS detector and the PHOBOS coordinate system. The top part of the magnet has been removed for clarity.

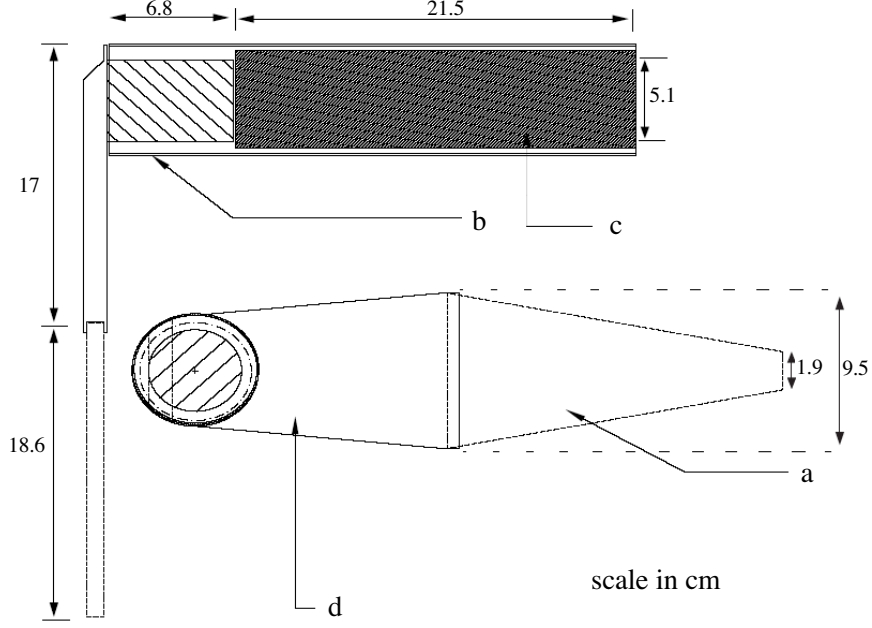


Figure 2.3: Components of an individual paddle module: a) scintillator, b) magnetic shield, c) photomultiplier tube, d) light guide.

The active area of each array subtends 94% of the solid angle in the pseudo-rapidity range $3 < |\eta| < 4.5$.

When a particle interacts with the plastic scintillator in a paddle module the energy and the timing of the interaction are recorded. This information can be used, in conjunction with the number of paddle modules that were hit, to determine whether the collision event should trigger the read-out of the other PHOBOS sub-detectors. Trigger conditions can be varied based upon the desired characteristics of the data set. At a minimum, the timing of the paddle signal must be consistent with the time-of-flight of the particle from within the interaction diamond of the colliding beams. The time-of-flight of a particle with a velocity approaching the speed of light from the nominal interaction point to the paddle counters is ~ 11 ns. The width of the timing cut applied is dependent upon the desired z-vertex range.

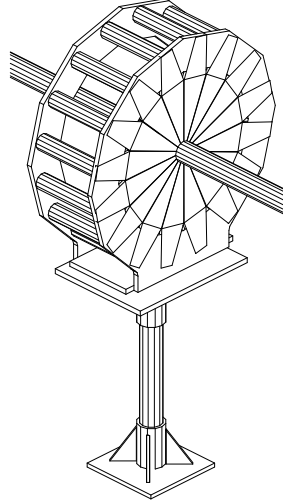


Figure 2.4: Schematic diagram of a Paddle Counter mounted around the beam pipe.

Because the paddles have equal sensitivity to particles traveling in both directions, a coincidence of at least one hit in both the negative and positive paddle arrays with the proper timing is required. Figure 2.5 shows the time difference distribution of events that fire both paddles in coincidence. Even strict timing restrictions still allow a limited number of background events to be recorded. Background events are removed in the analysis software as described in Sec. 3.2.

The paddle counters can also be used to estimate the centrality of the event. If the number of particles produced in a collision is assumed to increase monotonically with collision centrality, then the total energy deposited in both paddle counters is also proportional to centrality. This relationship can be used to create a centrality trigger to enhance the proportion of central or peripheral events in the data set. This is implemented by applying a maximum or minimum hardware cut to the summed paddle energy, shown in Fig. 2.6.

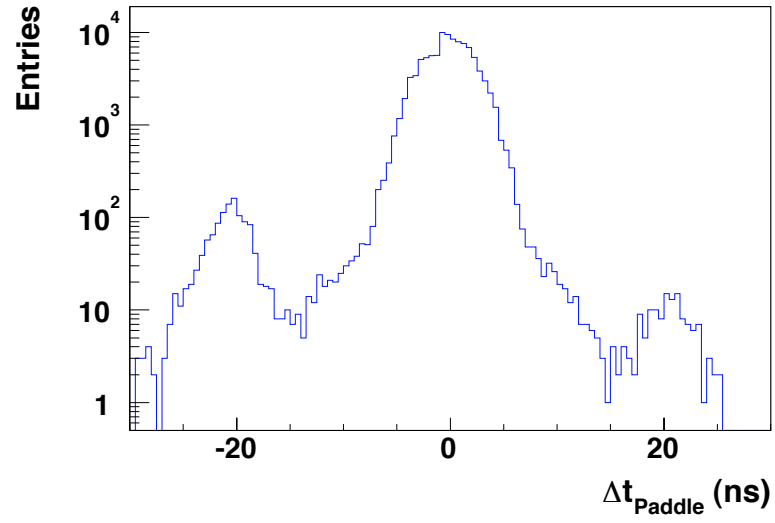


Figure 2.5: Time difference distribution of events in which both Paddle Counters fire.

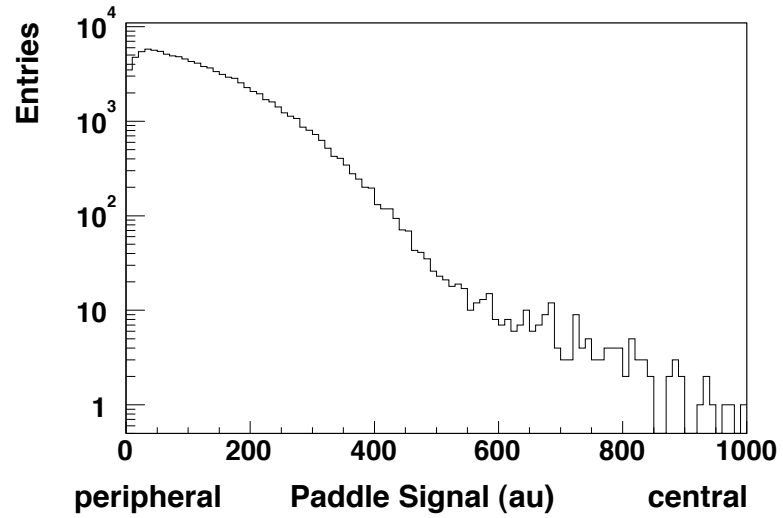


Figure 2.6: Summed energy of the negative Paddle Counter modules for d+Au collisions (Au side).

2.2.1.2 T_0 Trigger Counters

The two T_0 Trigger Counters are each arrays of 10 modules. The individual modules are constructed from a cylindrical acrylic Čerenkov radiator (Bicron, BC-800), coupled to a fast photomultiplier tube (Hamamatsu, R2083). The radiators have a length of 3.0 *cm* and a diameter of 5.1 *cm*. A diagram of the setup can be seen in Fig. 2.7. The positions of the T_0 Trigger Counters were chosen to optimize the acceptance for primary collision products, while minimizing the amount they shadow the acceptance of the Ring Multiplicity Counters. For the d+Au collision system the positive array (d side) was positioned at $z = 2.6$ *m* and the negative array (Au side) was placed at $z = -5.3$ *m*. The positive and negative counters covered the pseudo-rapidity ranges of $3.7 < |\eta| < 4.2$ and $-4.9 < |\eta| < -4.4$, respectively. The counters were repositioned for the p+p collision system, with the positive T_0 array installed at $z = 2.5$ *m*, covering a pseudo-rapidity range of $3.6 < |\eta| < 4.1$, and the negative array at $z = -1.2$ *m*, covering $2.9 < |\eta| < 3.4$.

The T_0 Trigger Counters were used to determine whether a collision event should be recorded, in an analogous manner to the Paddle Trigger Counters. When a particle interacts with a T_0 radiator the energy and timing of the interaction are recorded. A triggered event requires that the timing of the interaction with respect to the collision be consistent with the assumption that the particle originated from the collision. In addition, a coincidence between at least one negative T_0 module and one positive T_0 module was required to minimize background contamination.

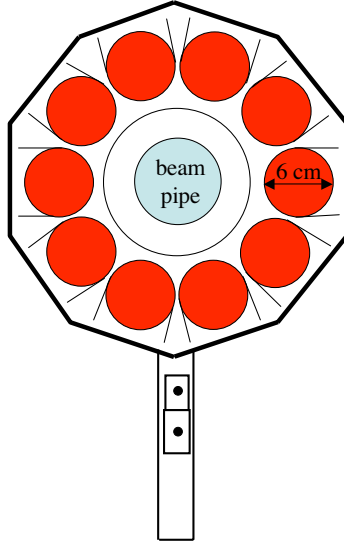


Figure 2.7: Front view of the T_0 trigger counters and mounting frame.

2.2.1.3 Čerenkov Trigger Counters

The PHOBOS detector has two sets of Čerenkov Trigger counters located at $z = \pm 5.5 \text{ m}$ [44]. Each counter is an assembly of 16 individual modules. A module is composed of an acrylic radiator (Bicron, BC-800), a hybrid photomultiplier tube assembly (Hamamatsu, H5211, phototube R1924), and a double magnetic shield to protect the photomultiplier tube. The dimensions of each of these components are shown in Fig. 2.8. The modules are mounted in a circle around the beam pipe so that the radiators are parallel to the beam line, as shown in Fig 2.9. The distance from the center of the radiators to the beam pipe is 8.57 cm . The active area of each counter subtends 37% of the solid angle over a pseudo-rapidity range of $4.5 < \eta < 4.7$. The timing resolution of the Čerenkov modules is between 350 and 400 ps and the signal-to-noise ratio is 6:1. Using timing delay cables and position adjustments built into

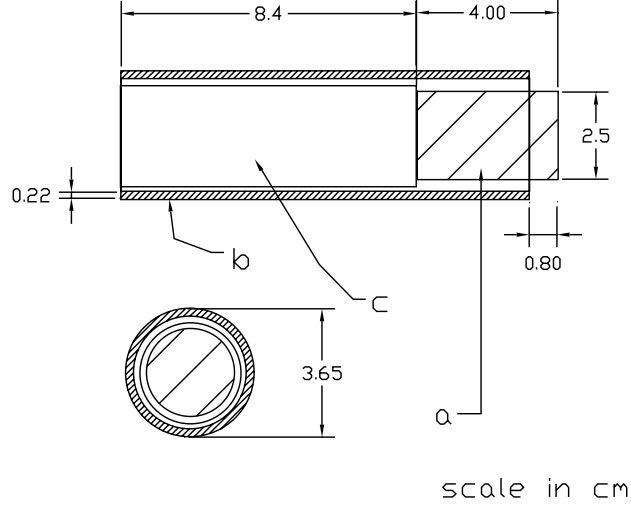


Figure 2.8: Components of a Čerenkov module: a) radiator, b) magnetic shield, c) photomultiplier tube.

the frame of the mount, the timing of the counters was matched to within 50 *ps*. This level of precision was possible due to the fact that the mounting frame was designed to allow for fine position adjustments in *mm* increments, up to a total length of 10 *cm* along the axis of the beam.

The Čerenkov Trigger Counters can be used to provide an online event vertex cut. This is necessary because the collision vertex provided by RHIC is known to fluctuate by as much as ± 60 *cm* [44]. The useable vertex range for the PHOBOS spectrometer based analyses is only ± 12 *cm*; therefore, it is desirable to maximize the fraction of recorded events that contain vertices within these limits. A trigger is provided when the time difference between the first signals from the negative and positive Čerenkov arrays is consistent with the desired vertex range. The vertex trigger decision is available 650 *ns* after the collision. The vertex resolution of the counters is 4 *cm* [44].

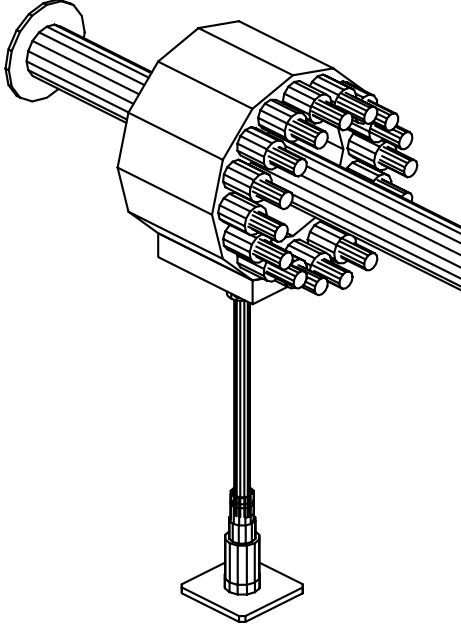


Figure 2.9: Drawing of a Čerenkov Counter around the beam pipe.

2.2.1.4 Zero Degree Calorimeters

When a collision occurs between two nuclei the matter that does not participate in the collision due to incomplete geometrical overlap either fragments or evaporates. The fragments are referred to as *spectators*. At RHIC three types of spectators are commonly observed, protons, neutrons and charged fragments. After the collision, the protons are diverted out of the beam pipe by the magnetic field of the DX magnets and the neutrons proceed in a straight path along the axis of the collision. The charged fragments proceed along the path of the beam pipe because their charge to mass ratio is low, thus their path bends little in the magnetic field. The Zero Degree Calorimeters, ZDC's, are positioned to detect the spectator neutrons. Figure 2.10 shows the magnitude of the deflection of each of the types of spectators, as well as the path of the beam. A coincidence between the positive and negative

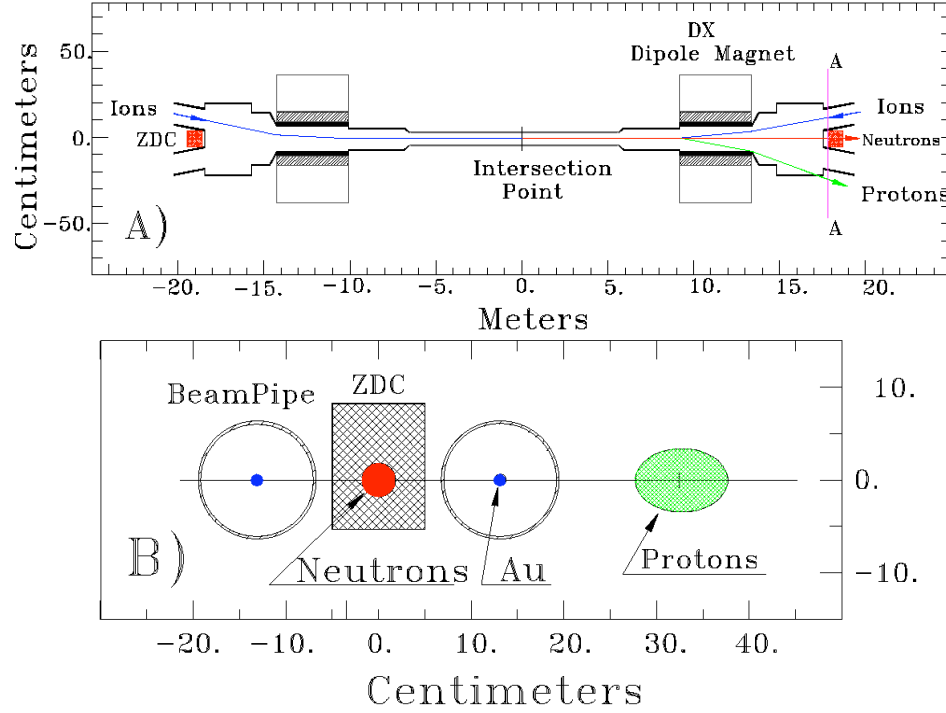


Figure 2.10: Top) Diagram of the position of the Zero Degree Calorimeters, ZDC's, in the RHIC tunnel in relation to the nominal intersection point and the DX dipole magnets. Bottom) View of the positions of protons and neutrons along the transverse x-axis at the position of the ZDC's.

ZDC's can be used as an event trigger. In addition, the ZDC's are also used to provide a common measure of beam luminosity among the four RHIC experiments.

The Zero Degree Calorimeters are the only common sub-detector among all four of the RHIC experiments [45]. One ZDC sits at either end of the PHOBOS experiment, $z = \pm 18.5$ m, behind the DX magnets where the two RHIC beam lines diverge. Each ZDC is constructed from three calorimeter modules, which are themselves alternating layers of 5-mm thick tungsten alloy absorber and 0.5-mm diameter Čerenkov fiber layers. The light produced from the fibers in each module

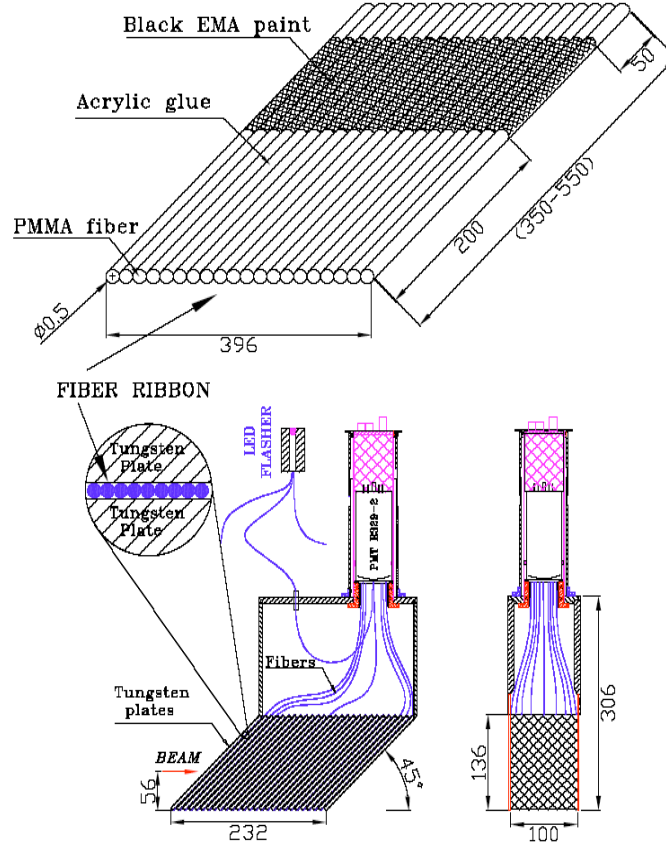


Figure 2.11: Zero Degree Calorimeter module assembly. All dimensions shown are in units of mm . [45]

is collected by a 50- mm diameter photomultiplier tube (Hamamatsu, R239). Figure 2.11 shows a schematic diagram of a ZDC module. The ZDC plates are oriented at 45° to the beam axis to optimize the yield of Čerenkov light and discriminate against background particles. The three modules are placed directly behind one another to maximize the amount of neutral energy that is collected; an efficiency of 98% is achieved.

2.2.1.5 Spectrometer Trigger

Two Spectrometer Trigger walls were installed in PHOBOS for the 2003 Physics Run. One wall is positioned parallel to the beam pipe at $x = -1.6$ m and has a pseudo-rapidity coverage of $|\eta| < 0.23$. The other wall is positioned at a 45° angle with respect to the beam pipe, $x = -2.0$ m from the nominal interaction point, and has a pseudo-rapidity coverage of $0.64 < \eta < 1.2$. Each wall is composed of ten modules. A module consists of a rectangular plastic scintillator (Bicron, BC408), a plexiglass light guide, a photomultiplier tube (Amperex, XP2212S), and a magnetic shield. Diagrams of a Spectrometer Trigger module and the mounting frame are shown in Fig. 2.12.

The Spectrometer Trigger walls were designed to optimize the efficiency of triggering on high p_T charged particles produced within the PHOBOS acceptance. High p_T particles can be identified because their flight paths are weakly affected by the PHOBOS magnetic field. This allows them to travel along a straight line trajectory from the event vertex. Each Spectrometer Trigger wall is placed between the last silicon plane of the Spectrometer and a Time-of-Flight wall. A coincidence between a Spectrometer Trigger module and the Time-of-Flight wall must linearly extrapolate back to the known z-position of the event vertex in order to initiate a trigger. This ensures that each triggered event possesses the characteristic features of high p_T particle production.

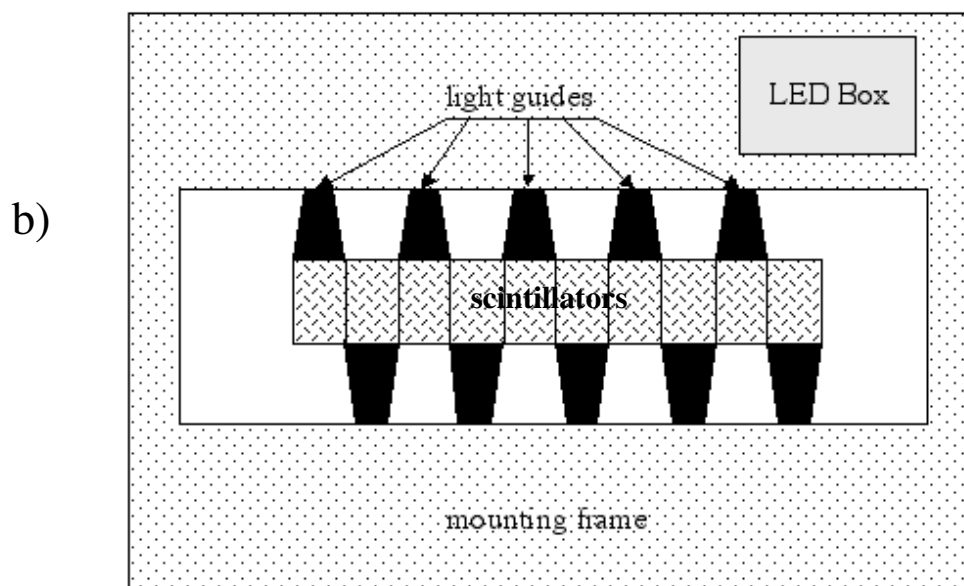
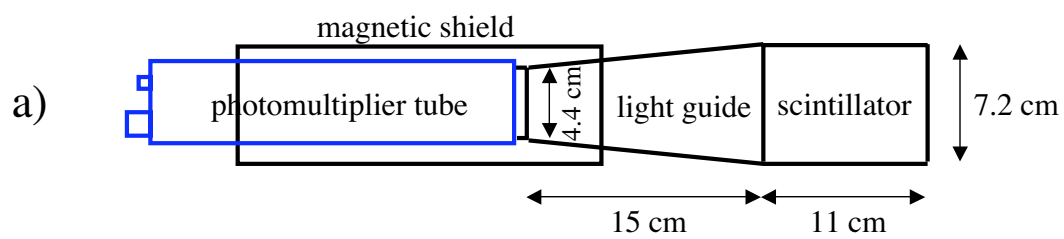


Figure 2.12: a) Schematic diagram of a Spectrometer Trigger module. b) Diagram of one Spectrometer Trigger wall with modules installed.

2.2.2 Event Vertex Determination

Every collision between two nuclei occurs at a well-defined location in space; therefore, the spatial coordinates of the collision position can be determined. This location is defined as the event vertex. In this analysis, events are selected based upon their collision vertex to ensure that the properties of the collision are accurately represented by the information recorded by each sub-detector. Two principle sub-detectors are used in the PHOBOS experiment to determine the event vertex: the Octagon and the Vertex Detector.

2.2.2.1 Octagon

The Octagon received its name because it is an octagonal barrel of silicon sensors positioned around the beam pipe. The Octagon is 120-*cm* long and has a diameter of 9 *cm*. Four of the eight sides of the Octagon are constructed from thirteen silicon sensors each oriented parallel to the beam pipe. The remaining four sides are each missing three sensors. These sensors were excluded to leave openings for the Top and Bottom Vertex detectors and the Positive and Negative Spectrometer arms, thus reducing the number of secondary particles produced along the trajectories to those sub-detectors. The silicon sensors in the Octagon are 3.6 *cm* \times 8.4 *cm* and have a total of 11,040 active channels. The Octagon has a large acceptance in pseudo-rapidity, $|\eta| < 3.2$, and covers nearly 2π in ϕ . A schematic diagram of the Octagon is shown in Fig. 2.13.

In the low multiplicity environment of d+Au and p+p collisions only the longi-

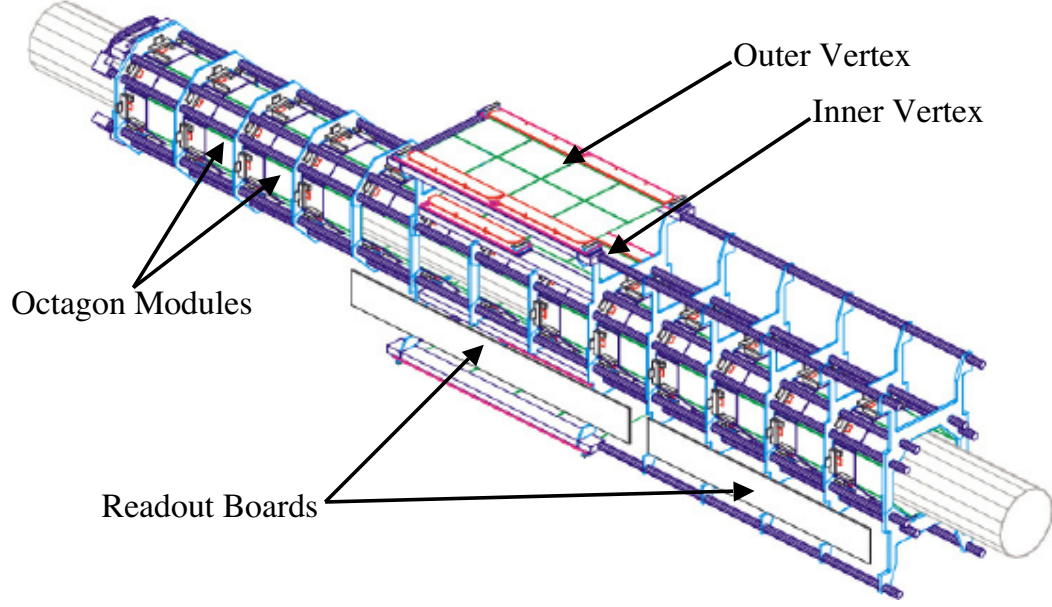


Figure 2.13: Schematic diagram of the Octagon and Vertex Detectors.

tudinal position, z , of the collision can be determined. The z -position of the vertex is found by maximizing the number of hits in the Octagon above a variable threshold. Due to the changing angle of incidence, the energy deposited per track in the Octagon increases as the distance from the vertex increases; thus, the low energy cutoff that defines a hit also increases with distance from the vertex. The vertex resolution ranges from 0.7 cm to 1.3 cm in central and peripheral collisions, respectively [46].

2.2.2.2 Vertex Detector

The Vertex Detector is composed of two planes of silicon sensors that sit above, $y > 0$, the nominal interaction point and two planes of silicon sensors that sit below, $y < 0$, the nominal interaction point, as shown in Fig. 2.13. The two Inner Vertex planes are located at $y = \pm 5.64\text{ cm}$ from the beam axis and the Outer Vertex planes are located at $y = \pm 11.78\text{ cm}$. The Inner Vertex layers are each composed

of four silicon sensors that have a 0.47-mm segmentation in the z-direction and a 1.2-cm segmentation in the x-direction. The Outer Vertex layers each have eight silicon sensors that have a 0.47-mm segmentation in the z-direction and a 2.4-cm segmentation in the x-direction. The physical dimensions of the silicon sensors are $6.06\text{ cm} \times 4.82\text{ cm}$. The pseudo-rapidity coverage of the Inner Vertex layers is $|\eta| < 1.54$ and is $|\eta| < 0.92$ for the Outer Vertex layers. The Vertex detectors cover 42.7° in ϕ .

The event vertex is reconstructed by identifying two-point tracks from hits in the Inner and Outer Vertex layers that point back to the collision vertex. Due to the segmentation of the silicon pads, the Vertex detector is only able to resolve the y and z components of the event vertex. The design goal of the Vertex detector was to determine the vertex position with an accuracy of less than 0.2 mm in the z-direction for central Au+Au collisions; a z-vertex resolution of 0.32 mm was achieved [47]. The primary contribution to the resolution comes from inaccuracies in the measurement of the geometrical positions of the silicon sensors.

2.2.3 Centrality Determination

When two nuclei collide the properties of the collision can be characterized based upon the geometrical overlap of the nuclei. A glancing collision with incomplete overlap is referred to as a *peripheral* collision, whereas a head-on collision is a *central* collision. In general, the multiplicity of the collision, or number of produced particles, scales with collision centrality. In the PHOBOS experiment many of the

sub-detectors measure multiplicity and can be used to measure collision centrality. In this analysis the Ring Multiplicity Counters are used. In addition, the Proton Calorimeter provides a multiplicity independent measure of centrality by measuring the amount of energy deposited by spectator protons.

2.2.3.1 Ring Multiplicity Counters

Six Ring Multiplicity Counters are installed in the PHOBOS detector. Three are located on the positive z-side of the nominal interaction point at $z = +1.13, +2.35$ and $+5.05$ m, while the remaining three Rings are located at the same positions in the negative z-direction. Each Ring Counter is an octagonal array of eight silicon sensors that are each divided into 64 pads. The silicon sensors are trapezoidal in shape and the pad size increases radially outward so that each pad spans an equal range in $\Delta\eta\Delta\phi$ space. The pad sizes range from $3.8\text{ mm} \times 5.1\text{ mm}$ in the inner most pads to $10.2\text{ mm} \times 10.2\text{ mm}$ in the outermost pads. The inner diameter of each counter is 10 cm and the outer diameter is 22 cm . A diagram of a Ring Multiplicity Counter is shown installed around the beam pipe in Fig. 2.14. The Ring Counters cover a pseudo-rapidity range of $3 < |\eta| < 5.4$ and extend the range over which PHOBOS can measure charged particle multiplicity to $|\eta| < 5.4$.

When a collision event produces particles that interact with the Ring Counters the total energy deposited in the sensors is recorded. The number of particles that are incident upon the Rings can be determined based on the magnitude of the deposited energy. These variables are referred to as E_{Ring} and N_{Ring} , respectively. Both of these variables are proportional to the multiplicity of the event, thus are

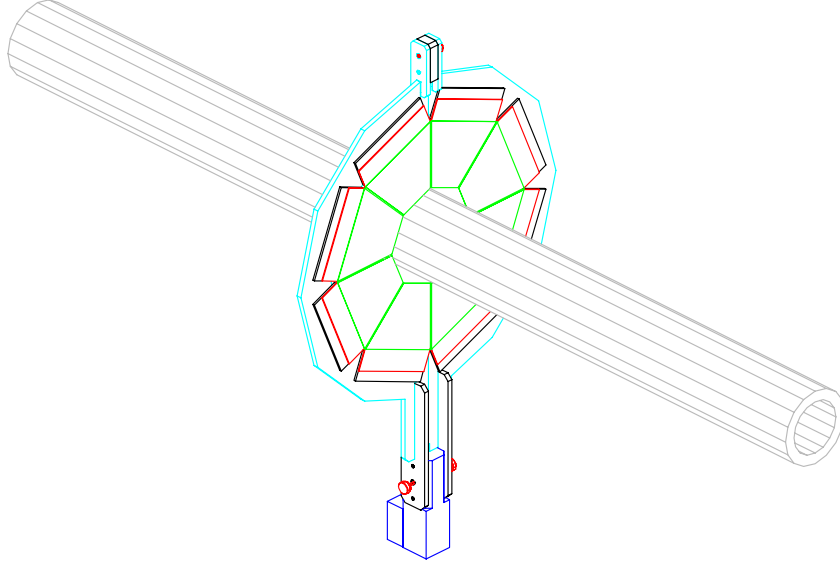


Figure 2.14: Schematic diagram of a Ring Multiplicity Counter positioned around the beam pipe.

also proportional to the collision centrality. HIJING Monte-Carlo [12] simulated events propagated through a GEANT 3.21 simulation [11] of the PHOBOS detector can be used to assign each collision event to a centrality class. Section 3.4 provides a more detailed explanation of how centrality classes are assigned in this analysis.

2.2.3.2 Proton Calorimeter

Two Proton Calorimeters were installed in the PHOBOS detector for the 2003 Physics Run. A full-sized calorimeter was located on the Au side adjacent to the negative ZDC outside of the DX magnet and a smaller mini-calorimeter was adjacent to the positive ZDC in d direction. The negative Proton Calorimeter is an 8×11 array of lead scintillating fiber modules; the positive Proton Calorimeter is a 2×2 array of the same modules. A schematic diagram of the negative Proton Calorimeter is shown in Fig. 2.15a. Each module is a *spaghetti* type calorimeter

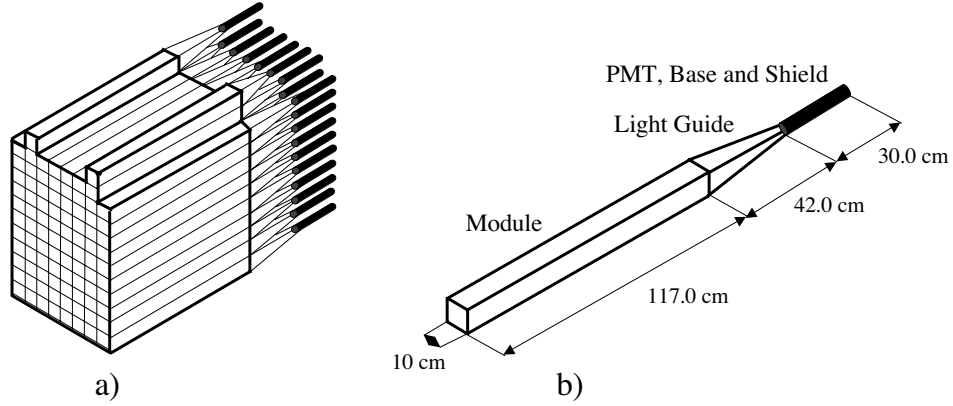


Figure 2.15: a) Schematic diagram of the negative Proton Calorimeter. b) Diagram of an individual Proton Calorimeter module.

constructed from layers of lead substrate, scintillating plastic fiber optics (Bicron, BCF12), a lucite light guide, and a photomultiplier tube (Philips, XP-2262B). The lead substrate is a mixture of 99% lead and 1% antimony. The scintillating fibers are embedded in grooves in the lead substrate at intervals of 0.213 cm . Each module contains a 47×47 array of fibers. A diagram of an individual module and the corresponding dimensions is shown in Fig. 2.15b.

The design of the Proton Calorimeters is based on the same principals as the ZDC's. However, whereas the ZDC's are positioned to measure the spectator neutrons from a collision, the Proton Calorimeters are positioned to measure protons. Two types of protons, referred to as black and grey, survive a heavy ion collision. Grey protons have lost linear momentum in the collision and are also known as recoil protons. Black protons are true spectator particles that did not participate in the collision. When black and grey protons encounter the magnetic field of the DX magnet they are deflected in the direction of the Proton Calorimeter. The decrease in linear momentum suffered by the grey protons during the collision causes them

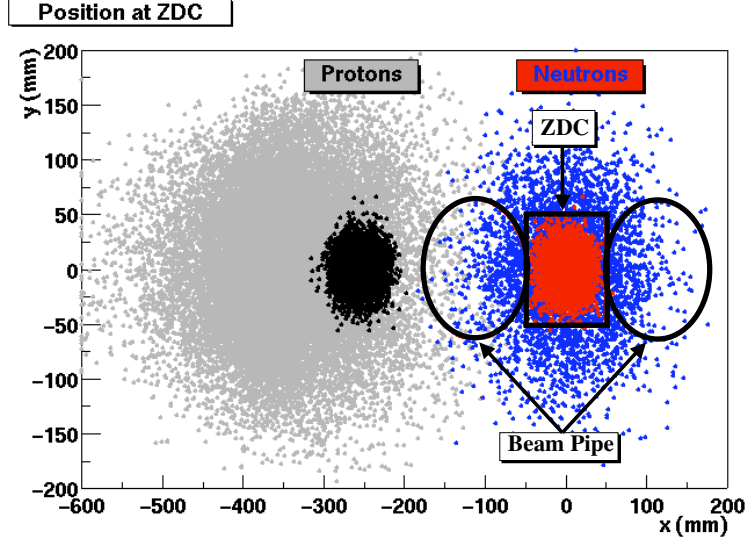


Figure 2.16: Simulation of the separation of spectator and recoil protons and neutrons at $z = 18$ m. Recoil protons are shown in grey, spectator protons are black, recoil neutrons are blue and spectator neutrons are red.

to be deflected at an angle greater than that of the black protons. This results in a separation of the two types of protons, as shown in Fig. 2.16. The Proton Calorimeters record the amount of energy deposited in the modules per collision. This value should be proportional to the centrality of the collision.

2.2.4 Particle Identification

The physical properties of the particles produced in a heavy ion collision can be used to identify each particle. The PHOBOS experiment is designed to detect hadrons. Pions, kaons and protons can be identified. Two sub-detectors are used for particle identification: the Spectrometer and the Time-of-Flight Walls. The charge sign of each particle can be identified by observing its bending direction in the field of the PHOBOS Magnet. This analysis exclusively uses results obtained from the

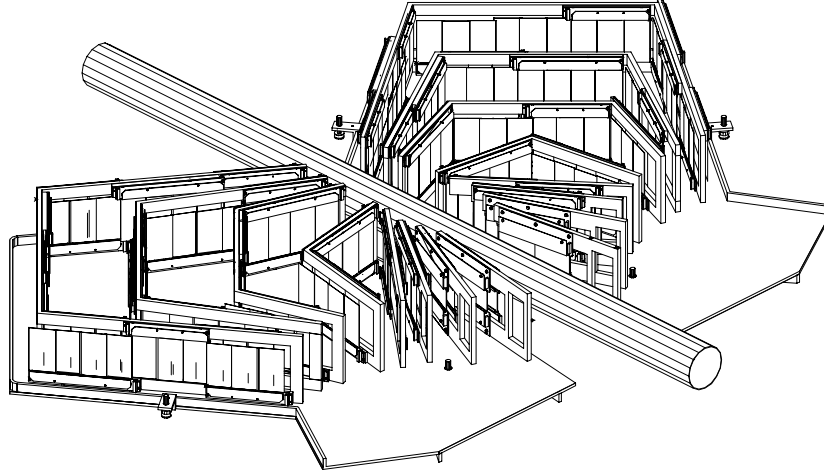


Figure 2.17: Schematic diagram of the Spectrometer installed around the beam pipe.

Spectrometer when the magnetic field was applied. A more detailed description of how particles are identified can be found in Chapter 5.

2.2.4.1 Spectrometer

The PHOBOS Spectrometer consists of two arms of silicon tracking planes that are symmetric about the beam pipe, as shown in Fig. 2.17. Each arm is constructed from 42 multi-sensor modules with 137 silicon sensors, 780 read-out chips and a total of 56,064 channels. The arms can be divided into three different regions based upon the shape of the silicon planes. The eight planes closest to the beam pipe are straight, the ninth and tenth planes are triangular and the six outer planes are U-shaped. The first plane sits 8 *cm* from the nominal interaction point and the last plane is approximately 75 *cm* from the same point.

Five types of silicon sensors are used in each spectrometer arm. Table 2.2 provides a summary of the characteristics of each type of sensor. Type 1 and Type

Table 2.2: Spectrometer Sensor Specifications

Sensor	Number of Pads	Pad Size (mm^2)	Location
Type 1	70×22	1.000×1.0	Planes 1-4
Type 2	100×5	0.427×6.0	Planes 5-8
Type 3	64×8	0.667×7.5	Planes 9-16 inner wing
Type 4	64×4	0.667×15.0	Planes 9-12
Type 5	64×4	0.667×19.0	Planes 13-16

2 sensors have the smallest pixel width and therefore the highest resolution. They are used close to the interaction point and in the region where the magnetic field is increasing rapidly in order to provide an accurate estimate of the initial trajectory of the particles and their curvature in the magnetic field. Type 4 and Type 5 sensors are optimized to provide information about the momentum of the particles while minimizing the number of channels. These sensors are installed in the planes furthest from the collision. Type 3 sensors are installed in the inner wing of planes 9 – 16 close to the beam pipe. Type 3 sensors are more highly segmented in the y-direction than Types 4 and 5 because particle densities in this region are high.

The silicon modules are mounted on aluminum cooling frames through which cooled water is circulated. The cooling frames are supported by a carbon-epoxy carrier frame that itself is mounted on a movable trolley. This allows each arm to be independently rolled into and out of the gap in the magnet. All materials were chosen to minimize vibrations and deflections induced by the magnetic field, which is described in Sec. 2.2.4.2.

The spectrometer was designed to provide particle tracking and identification for approximately 2% of all particles produced in a collision. The acceptance of

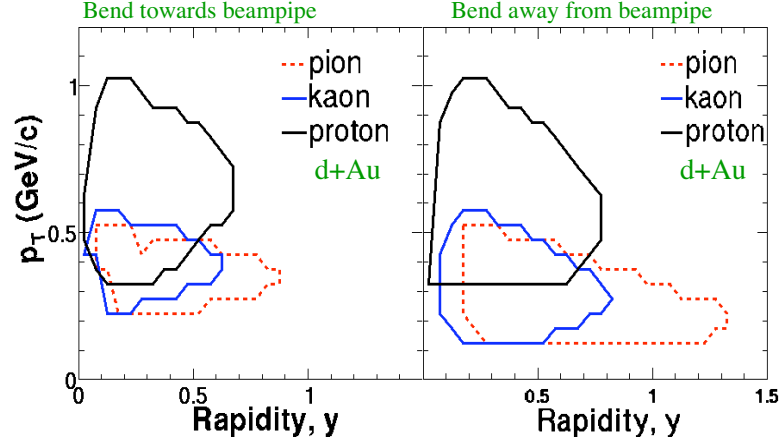


Figure 2.18: Spectrometer acceptance as a function of transverse momentum and rapidity, for each particle species in the two bending directions for the d+Au data set. The contours represent where the acceptance has fallen to 10% of the maximal value.

the spectrometer in rapidity, y , and transverse momentum, p_T , space is shown in Fig. 2.18. The upper p_T limits are imposed by the energy resolution of the Spectrometer, not the geometrical acceptance. Low momentum particles that stop in one of the first seven planes of the spectrometer are identified using the particle's total energy and measured energy deposition. Higher momentum particles that traverse 15 of the 16 silicon planes are identified based upon their energy deposition and radius of curvature in the magnetic field.

2.2.4.2 Magnet

The PHOBOS Magnet is a conventional magnet that was designed to provide a magnetic field in the spectrometer region. The magnetic field bends particles through the spectrometer planes, thus allowing their momentum to be measured. This requires a low field region close to the interaction point so that the initial straight trajectory of the particles can be determined and a uniform high field region throughout the

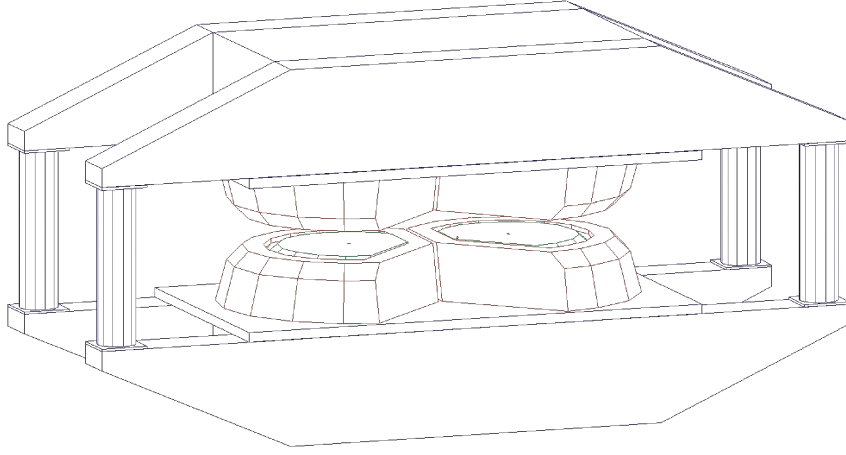


Figure 2.19: Schematic diagram of the PHOBOS magnet. The beam pipe runs through the center of the magnet out of the plane of the page.

rest of the spectrometer to measure the curvature of the particles. This is achieved with a double dipole magnet design, as shown in Fig. 2.19. The Magnet straddles the beam pipe and provides a field directed vertically upward around one spectrometer arm and a downward directed field around the other arm. The polarity of the magnetic field is reversible, allowing identical measurements to be made in both spectrometer arms. A map of the vertical component of the magnetic field for one arm is shown in Fig. 2.20. The positions of the spectrometer planes are indicated in the diagram. The spectrometer sits within the 15.8 cm gap between the top and bottom halves of the Magnet. The maximum field provided by the PHOBOS Magnet is 2.18 Tesla and the total bending power is approximately 1.5 Tm . The dimensions of the magnet are $4.04\text{ m} \times 1.4\text{ m} \times 1.93\text{ m}$ and it weighs approximately $40,000\text{ kg}$.

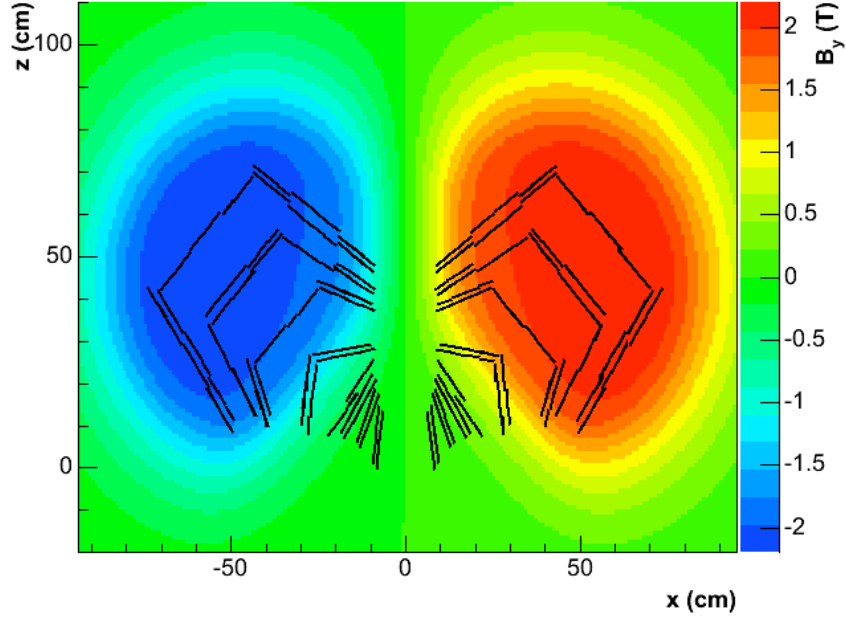


Figure 2.20: Map of the y-component of the magnetic field. The positions of both the positive and negative spectrometer arms are shown. The beam pipe runs along the z-axis at $x = 0$ cm.

2.2.4.3 Time-of-Flight Walls

The range in p_T over which particles can be identified in PHOBOS is extended by two Time-of-Flight (TOF) Walls. For the 2003 Physics Run one wall was positioned parallel to the beam pipe at a distance of $x = -3.9$ m. The other wall was positioned $x = -5.4$ m from the nominal interaction point at a 45° angle with respect to the beam pipe. Each TOF wall is constructed from 30 scintillator modules, as shown in Fig. 2.21. The modules are composed of four pieces of plastic scintillator (Bicron BC404) attached via light guides to two photomultiplier tubes (Hamamatsu R5900U-M4). The plastic scintillators are 200-mm high and have a cross-sectional area of $8\text{ mm} \times 8\text{ mm}$. A photomultiplier tube is attached to the top and bottom of each scintillator and the time difference between the two signals is used to determine

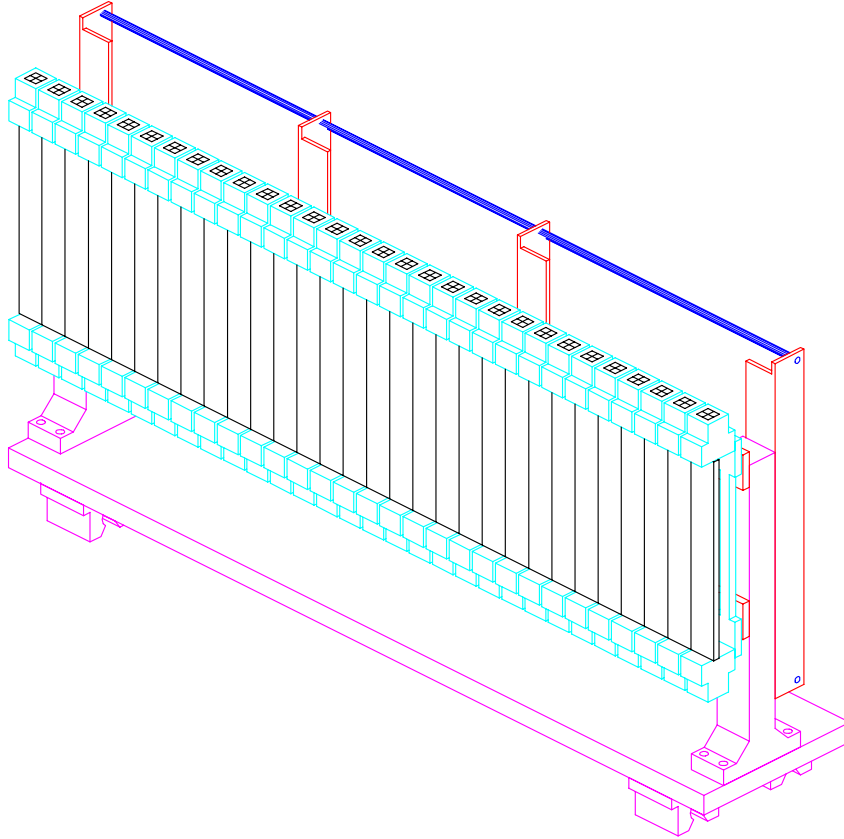


Figure 2.21: Diagram of an assembled Time-of-Flight Wall.

the vertical position of the incident particles. The vertical position resolution is 10 mm for the time difference reconstruction and 37 mm for the ratio of pulse height reconstruction technique. The time-of-flight resolution is 75 ps [47].

Particle tracking can be extended from the spectrometer to the Time-of-Flight Walls. This allows high momentum particles to be tracked and identified. Low momentum particles that are tracked in the spectrometer curve out of the acceptance of the TOF walls due to the strength of the magnetic field in the spectrometer region. The information provided by the Time-of-Flight Walls allows pions and kaons to be identified up to a momentum of $2.3\text{ GeV}/c$ and protons to be identified up to a

momentum of 3.2 GeV/c.

Chapter 3

Event Selection and Centrality Determination

In this analysis the antiparticle to particle ratios are measured for three different data sets. These data sets were collected using different trigger and event selection criteria and are referred to throughout the remainder of this document as dAVertex, dAPeriph and ppVertex. The dAVertex and dAPeriph data sets were collected from the d+Au collision system, while the ppVertex data set contains the results of p+p collisions. The dAVertex data was collected using a minimum bias T_0 vertex trigger. A Paddle centrality trigger was used in conjunction with the T_0 vertex trigger to collect the dAPeriph data set. Finally, the ppVertex data was collected using a minimum bias Paddle vertex trigger. In this chapter the details of each of these trigger conditions and event selection criteria are examined, as well as how the selected events are assigned to centrality classes.

3.1 Trigger Criteria

The PHOBOS detector is capable of collecting data using three principal types of triggers: minimum bias, vertex and centrality. The minimum bias trigger is the least restrictive. It is designed to sample a broad cross section of events without applying cuts that could introduce biases into the data set. An example of a minimum bias trigger is the single arm paddle trigger. This trigger records every event in which at least one Paddle Counter module detects a particle. It is considered to be minimum bias because the only restriction placed upon the event is that it produce a particle within the acceptance of one paddle module; thus, the bias of the data sample is minimized. Unfortunately, using a single arm paddle trigger the fraction of the collected events that can be used in this analysis is low due to the limited acceptance of the spectrometer. Furthermore, data collected with this trigger generally contain a high level of background contamination from beam-gas events in which a beam ion collides with a gas molecule in the beam pipe.

In order to enhance the fraction of events that contain tracks in the spectrometer, while minimizing the bias introduced into the data sets, a vertex trigger can be implemented. A vertex trigger requires a coincidence between two detectors placed on either side of the nominal interaction point, as shown in Fig. 3.1. The timing of the coincidence must be compatible with the collision having occurred within the preset z-vertex limits. For the d+Au collision system a T_0 vertex trigger was implemented and a Paddle vertex trigger was commissioned for the p+p collision system. A vertex trigger eliminates many of the background events recorded by the

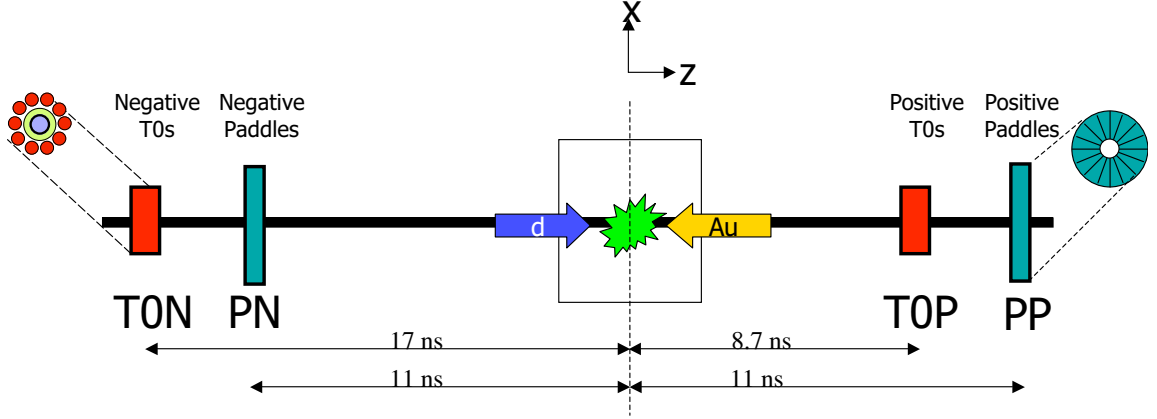


Figure 3.1: Timing diagram for the Paddle and T_0 Counters in the d+Au collision system, not to scale.

minimum bias trigger because a coincidence is required. However, it also introduces a bias into the data sample because a vertex trigger requires that at least two collision products be generated within the acceptance of the trigger detectors in order for the collision to be recorded.

Because the multiplicity of an event is proportional to the centrality of the collision, peripheral events are less likely to satisfy the conditions of a vertex trigger than are central collisions. This results in a deficit of peripheral collisions in vertex triggered data sets. Peripheral collisions can be selectively recorded using a centrality trigger. A peripheral centrality trigger requires that the multiplicity observed in a given sub-detector be below the preset limit for the event to be recorded. In a parallel fashion, a centrality trigger that selects central events can be implemented by requiring that the event multiplicity be above a preset limit. Of the PHOBOS trigger detectors, the Paddle and T_0 Counters have been used as centrality triggers.

3.1.1 dAVertex Trigger

The dAVertex triggered data was collected using a T_0 vertex trigger. This trigger requires a coincidence between a negative and a positive T_0 module. The time agreement between the two signals must correspond to an approximate vertex range of $|z| < 50$ cm. The dAVertex trigger samples 50% of the total collision cross section. Using this trigger, 31.4 million raw d+Au collision events were collected.

3.1.2 dAPeriph Trigger

In order to collect enough peripheral collisions to measure the centrality dependence of the antiparticle to particle ratios in d+Au collisions, a peripheral centrality trigger was implemented. The dAPeriph trigger requires that the multiplicity observed in both of the Paddle Counters be less than eight; therefore, high multiplicity events are rejected. This results in an enhancement of the fraction of peripheral events recorded. In order to make this data set as analogous as possible to the dAVertex triggered data, the T_0 vertex trigger conditions described in Sec. 3.1.1 were also required. The dAPeriph trigger samples only 11% of the total collision cross section, but has an efficiency of 21% for collision centralities of 30-100%; see Sec. 3.4 for a detailed explanation of centrality. A total of 21.4 million raw d+Au collision events were collected using the dAPeriph trigger.

3.1.3 ppVertex Trigger

The ppVertex trigger was designed in a similar way to the dAVertex Trigger, but uses the Paddle Counters instead of the T_0 Counters. The Paddles were chosen as the trigger for the low multiplicity p+p collision environment due to their large geometrical acceptance. The ppVertex trigger requires a coincidence between a positive and negative paddle module and a time agreement that corresponds to an approximate vertex range of $|z| < 150 \text{ cm}$. The ppVertex trigger samples 62% of the inelastic collision cross section. After requiring a valid vertex reconstruction, 48% of the inelastic cross section is available for analysis. A total of 28.6 million raw p+p collision events were collected using the ppVertex trigger.

3.2 Event Selection

Event selection cuts are applied in the analysis software to remove background events and ensure that the data being analyzed are representative of a true collision. It is important that the collision occurred within the acceptance of the detector so that the properties of the collision are accurately represented by the data. The event selection criteria used for each of the collision systems are described in the following sections.

3.2.1 d+Au Collision Criteria

The event selection criteria applied to the d+Au data are shown in Table 3.1. The beam of ions that circulates in the RHIC ring is not a steady stream of particles.

Table 3.1: Event Selection Criteria for the d+Au Data Sets

Condition	Cut	Description
AllT0Diagonal	$ T_0N - T_0P \leq 5 \text{ ns}$	Collision occurred between nuclei in the central beam bunches
NotPileUp	NotPrePileUp NotPostPileUp	No pile-up 5 μs before event No pile-up 600 ns after event
PaddleCoinc	$(multN > 0) \&\& (multP > 0)$	Coincidence in Paddle Counters; required for centrality definitions
ValidOctDeVz	$OctDeVz \neq 0$	Valid vertex found in Octagon
OctDeT0	$ OctDeVz - T0Vz < 25 \text{ cm}$	Agreement between two different vertexing techniques
NarrowVertex	$ OctDeVz \leq 8 \text{ cm}$	Vertex in spectrometer acceptance

Instead, when the beam is first injected into the RHIC ring, the particles are grouped into *bunches*. The beam is steered to provide collisions between the central bunches of each beam at the nominal interaction point. As the beam ages, particles begin to leak out of the initial central bunch into the adjacent gaps. Collisions between non-central bunches do not necessarily occur at the nominal interaction point. The AllT0Diagonal cut is applied to remove events that occur between non-central beam bunches by placing a more restrictive time requirement on the coincidence between the negative and positive T_0 's than is applied by the hardware trigger. This reduces the probability of reconstructing an invalid event vertex. Figure 3.2 shows dAVertex triggered events in black and those accepted by the AllT0Diagonal cut in red.

When two bunches of ions cross it is possible for more than one collision to occur before the sub-detectors are all read out. This condition is referred to as *pile-up*. When pile-up occurs, the data recorded by each sub-detector is representative of more than one event. This is particularly problematic when assigning events to centrality classes because the technique is dependent upon the total energy deposited

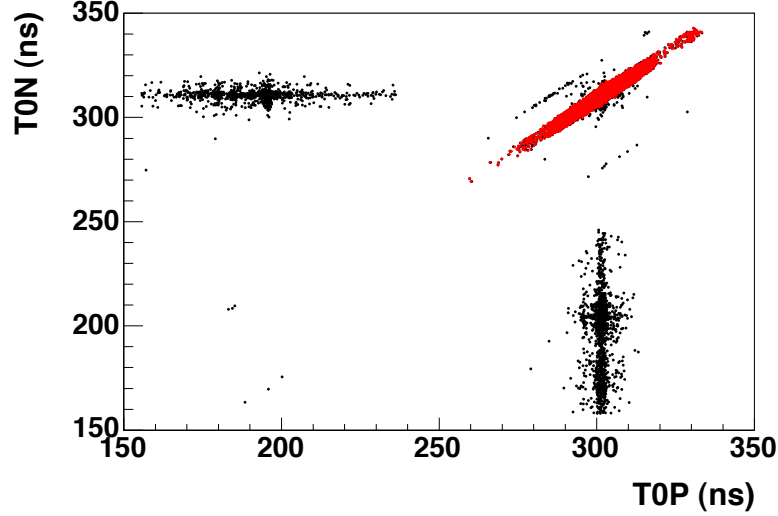


Figure 3.2: T0N collision time plotted versus T0P collision time. The dAVertex triggered events are shown in black and the dAVertex triggered events that pass the AllT0Diagonal cut are shown in red.

in the Ring Multiplicity counters per event, Sec. 3.4. Pile-up events that occur $5 \mu s$ before an event or within $600 ns$ after an event are removed from the analysis.

The PHOBOS detector identifies particles based upon the tracks they generate in the spectrometer. Only particles produced within the geometrical acceptance of the spectrometer generate tracks; therefore, it is important to remove collision events from the analysis that occur outside of the spectrometer acceptance. This is done by applying a cut to the z-position of the collision vertex, OctDeVz. However, first the accuracy of the value calculated for OctDeVz must be examined. The algorithm used to find the z-position of the event vertex in the Octagon has an undesirable default behavior when no collision products are detected in the Octagon. Because no vertex can be calculated, the algorithm assigns a default value of exactly zero. The ValidOctDeVz requirement shown in Table 3.1 removes events in which this occurs from the analysis. In addition, sometimes the information recorded by the Octagon

is insufficient to determine an accurate collision vertex. The accuracy of the vertex found in the Octagon is examined by comparing it with the z-vertex position found by the T_0 vertex trigger. This cut is referred to as OctDeT0 in Table 3.1. If the two z-vertex positions differ by more than 25 *cm* the event is removed from the analysis.

Once it has been established that an event has been assigned an accurate z-vertex position, the event can be examined to determine if it occurred within the acceptance of the spectrometer. Extensive studies were conducted to determine the geometrical acceptance of the spectrometer using Monte-Carlo events generated by HIJING [12] that were propagated through the detector using a GEANT 3.21 simulation [11]. The objective of this study is to find a z-vertex range over which the spectrometer accepts particles of both bending directions. The bending direction of a particle is defined as the product of the charge of the particle q and the polarity of the magnetic field B . The simulated events were generated in the range of $-20 < z < 20$ *cm* with a triangular input z-vertex distribution peaked at $z = 0$ *cm* with a base of $-45 < z < 45$ *cm*.

Figure 3.3 shows the results of this study for the sum of all particle species: pions, kaons and protons. It is observed that the acceptance of the spectrometer ranges from $-15 \leq z \leq 10$ *cm*, but begins to taper sharply in the range of $-15 < z < -10$ *cm* for both bending directions.

The resolution of the vertexing technique, OctDeVz, must be determined before assigning the z-cut positions. The resolution of OctDeVz is found using HIJING Monte-Carlo events with a known z-vertex position. The difference between the Monte-Carlo vertex and OctDeVz is calculated and the distribution is shown in

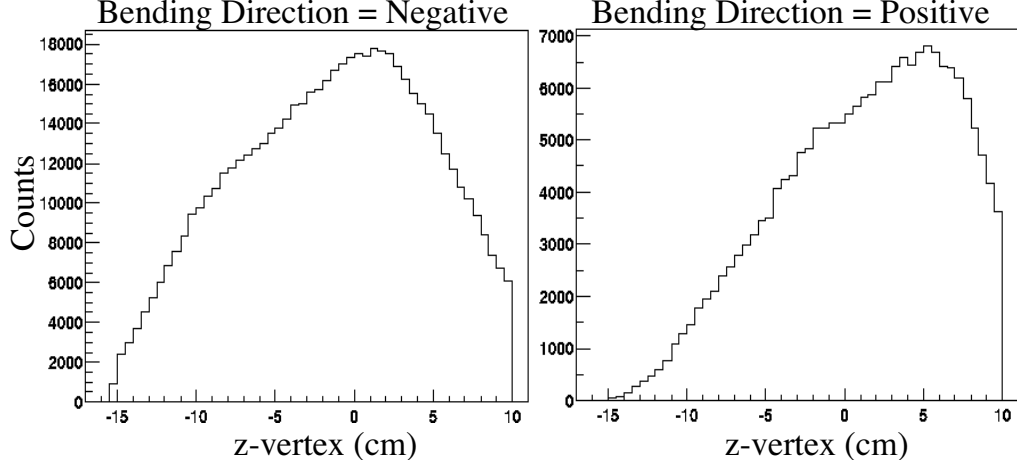


Figure 3.3: Distribution of z-vertex positions for all HIJING Monte-Carlo particles that produce tracks in the spectrometer. The bending direction is defined as the sign of the product of the charge, q , of the particle and the polarity, B , of the magnetic field.

Fig. 3.4. A Gaussian fit of each distribution shows that OctDeVz has a resolution of 0.7 cm for central events and 1.6 cm for peripheral events. The vertex resolution in the Octagon is lower for peripheral events than for central events because the ability of the vertex reconstruction algorithm to determine the vertex position is dependent upon the observed multiplicity.

The information obtained from the acceptance and resolution studies can be combined to determine the optimal z-vertex range to be used in the analysis. Two factors must be balanced. The statistics available for the analysis are maximized by a large vertex range; however, a large vertex range can also introduce systematic effects into the data sample, because events that occur outside of the acceptance of the spectrometer do not contribute tracks. The acceptance of the spectrometer is optimized for both bending directions in the range of $-10 < z < 10\text{ cm}$ and the position of the vertex is known to within $\pm 2\text{ cm}$. Therefore, a vertex range of

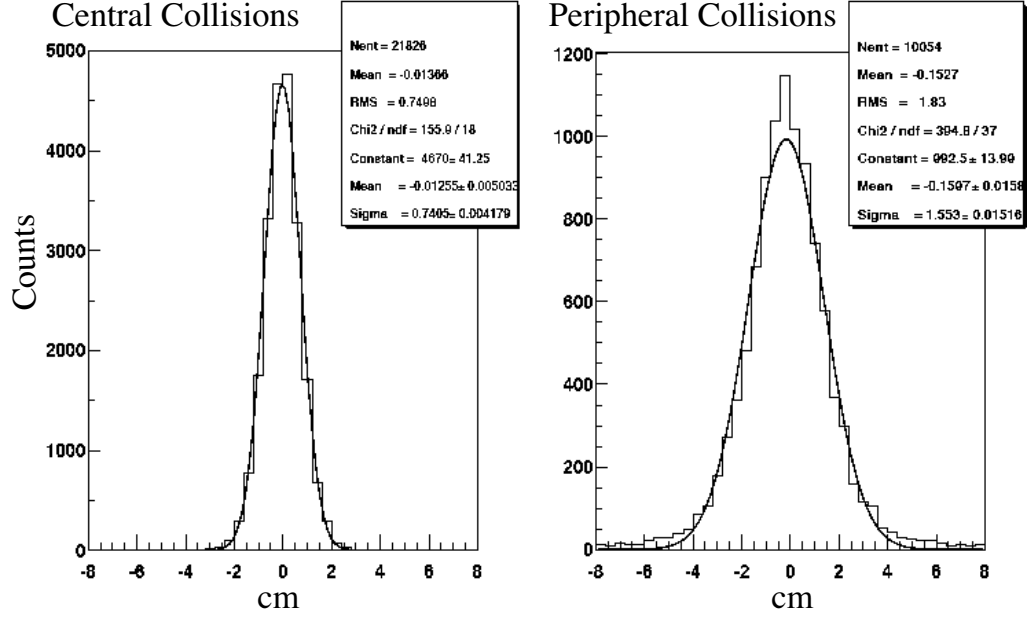


Figure 3.4: The distributions of the difference between the Monte-Carlo vertex and the experimental vertex, OctDeVz, are shown for central (0-10%) and peripheral (50-90%) collisions. The resolution of OctDeVz is determined by the Gaussian fit.

$-8 \leq z \leq 8$ cm is used.

3.2.2 p+p Collision Criteria

The event selection criteria used for the p+p data set are similar to those used for the d+Au system. Each of the event selection cuts are shown in Table 3.2. The only cut applied to the p+p data that is not used in the d+Au system is the PaddleTime cut. This cut limits the allowed normalized time difference between the negative and positive Paddle Counters to ± 5 ns. The PaddleTime cut is slightly more restrictive than the online ppVertex trigger to provide the vertexing algorithm with a restricted range within ± 75 cm of the nominal vertex. Because the T_0 sub-detectors were not used in the ppVertex trigger, it is not necessary to apply the AllT0Diagonal and

Table 3.2: Event Selection Criteria for the p+p Data Set

Condition	Cut	Description
NotPileUp	NotPrePileUp NotPostPileUp	No pile-up 5 μs before event No pile-up 600 ns after event
ValidOctDeVz	$OctDeTopo \neq 0$	Valid vertex found in Octagon
NarrowVertex	$ OctDeVz \leq 8 \text{ cm}$	Vertex in spectrometer acceptance
PaddleTime	$(PdlTDiff - PdlOffset) < 5 \text{ ns}$	Narrow Paddle time cut

OctDeT0 event selection cuts used in the analysis of the d+Au data sets.

3.3 Data Selection

Once the event selection criteria have been determined for each data set it is necessary to examine the events to ensure that they were collected under uniform conditions. Events in which the collider or the detector were not performing optimally are excluded from the analysis. Exclusion of such events reduces the systematic error introduced into the measurement of the particle ratios. It is found that many of the variables used to examine data quality are sensitive to the xy position at which the collision occurred. The mean xy collision position for a stable data collection period is referred to as the *beam orbit*. The data sets will first be divided into beam orbit regions before examining the quality of the data.

3.3.1 Beam Orbit Regions

The x and y positions of the beam orbit are plotted as a function of time or Run Number in Fig. 3.5. It can be seen that the position of the beam orbit remains

Table 3.3: Beam Orbit Regions for All Data Sets

Data Set	BO Region	$\langle x \rangle$ (cm)	$\langle y \rangle$ (cm)	Run Range	B+ Evts	B- Evts
dAVertex	0	0.10	0.050	10897-10921	4.1 M	1.2 M
dAVertex	1	0.15	0.075	10964-11057	2.7 M	4.8 M
dAVertex	2	0.15	-0.050	11066-11135	5.6 M	3.8 M
dAVertex	3	0.050	mix	11137-11197	3.2 M	6.0 M
dAPeriph	0	0.19	mix	11596-11639	2.3 M	2.2 M
dAPeriph	1	0.18	0.20	11658-11791	8.6 M	8.3 M
ppVertex	0	-0.0069	0.11	11978-12108	4.2 M	3.6 M
ppVertex	1	0.13	0.16	12216-12418	7.6 M	13.2 M

approximately constant for a period of time and then jumps to another value. The position of the beam orbit is strictly dependent upon the tune of the colliding beams. The colored lines in Fig. 3.5 represent the divisions between the beam orbit regions. Data collected between two like colored lines belongs to a given beam orbit region. The details of each region are documented in Table 3.3. It should be noted that in the dAVertex data set beam orbit region 3 does not have a constant mean value of the y position of the beam orbit. The region was not divided further into smaller regions because each of the smaller regions does not contain data collected with both magnet polarities. This situation also occurs in beam orbit region 0 of the dAPeriph data set. The technique used for determining the particle ratios requires that each beam orbit region contain data collected under both magnetic field polarities and is described in detail in Chapter 6.

3.3.2 Data Quality

The stability of the data as a function of time provides an estimate of the quality of the data with respect to detector and beam effects. A total of 22 different variables

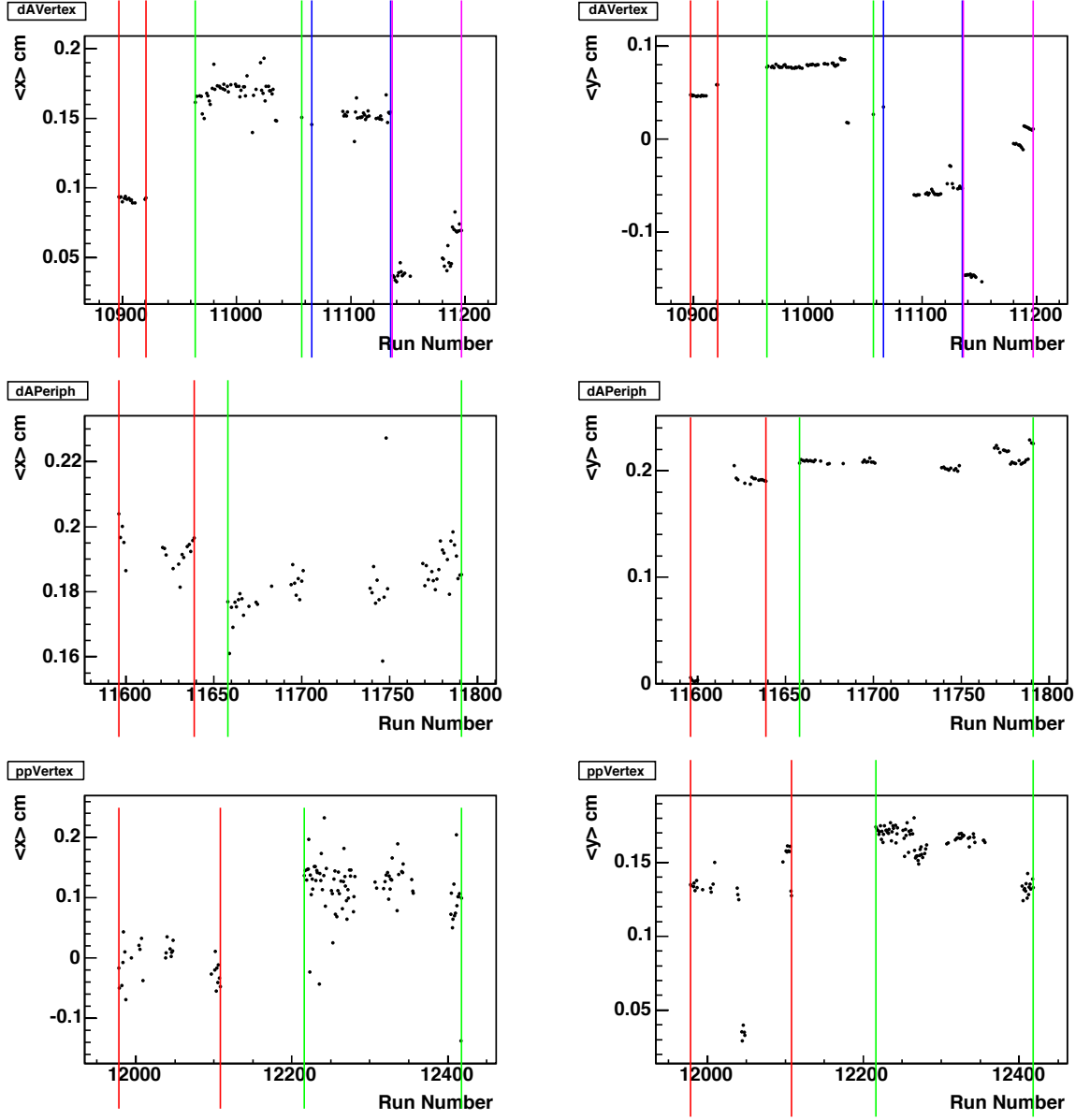


Figure 3.5: Mean x and y positions of the beam orbit for each data set. The vertical colored lines indicate the divisions between the beam orbit regions.

are used to estimate data quality. These variables are tabulated in Tables 3.4 and 3.5. The mean value of each variable for a given run is plotted versus run number, which is correlated with time. Figure 3.6 shows an example of the number of straight tracks found per selected event plotted versus run number. Each beam orbit region, from Table 3.3, is independently fit with a constant as shown by the red lines. The fit parameters are shown in the upper right corner of Fig. 3.6. The deviation of each run from the fit is then calculated. Data that is inconsistent with the fit is defined as deviating by 3 or more sigma. Finally, the number of data quality variables for which each run deviates from the fit by 3 sigma is tabulated. The results are shown for the dAPeriph data set in Fig 3.7. Table 3.6 contains a list of runs from the dAVertex, dAPeriph and ppVertex data sets that deviate the most. Because these runs constitute a significant fraction of each data set they are not excluded from the analysis. Instead, the effect of the inclusion of these runs on the final particle ratios is calculated and incorporated into the systematic error of the measurements.

Table 3.4: Variables Used to Determine Data Quality

Variable	Description
$\langle nStraightTracks \rangle$	Average number of straight tracks found per selected event
$\langle nCurvedTracks \rangle$	Average number of curved tracks found per selected event
$\langle nStraightTracks \rangle:SpecArm$	Average number of straight tracks found per selected event divided according to spectrometer arm
$\langle nCurvedTracks \rangle:SpecArm:Bend$	Average number of curved tracks found per selected event divided according to spectrometer arm and bending direction
$\langle nCurvedTracks \rangle:SpecArm:Q:B$	Average number of curved tracks found per selected event divided according to spectrometer arm, charge and polarity
$\langle StrTrkVtxVZ - OctDeVtxVZ \rangle$	Average difference between the z vertex position found using the StrTrkVtx and OctDeVtx methods per selected event
$\langle StrTrkVtxVY - beamy \rangle$	Average difference between the y vertex position found by the StrTrkVtx method and the y position of the beam orbit per selected event
$\langle StrTrkVtxVZ - OctDeVtxVZ \rangle:SpecArm$	Average difference between the z vertex position found using the StrTrkVtx and OctDeVtx methods per selected event divided according to spectrometer arm
$\langle StrTrkVtxVX - beamx \rangle$	Average difference between the x vertex position found by the StrTrkVtx method and the x position of the beam orbit per selected event
$\langle ZVertexVY - beamy \rangle$	Average difference between the y vertex position found by the ZVertex method and the y position of the beam orbit per selected event
$\langle StrTrkVtxVZ \rangle$	Average z vertex position found by the StrTrkVtx method per selected event
$\langle StrTrkVtxVX \rangle$	Average x vertex position found by the StrTrkVtx method per selected event
$\langle p \rangle: SpecArm:Bend$	Average track momentum per selected event divided according to spectrometer arm and bending direction

Table 3.5: Variables Used to Determine Data Quality, continued

Variable	Description
$\langle p \rangle$: PID	Average track momentum per selected event divided according to particle species
$\langle NOct \rangle$	Average number of hits in the Octagon per selected event and selected track (event weighted)
$\langle PdlMult \rangle$	Average event weighted paddle multiplicity
$\langle Rapidity_{\pi} \rangle$:SpecArm:Bend	Average rapidity of all tracks per selected event assuming the mass of the pion divided according to spectrometer arm and bending direction
$\langle Rapidity_K \rangle$:SpecArm:Bend	Average rapidity of all tracks per selected event assuming the mass of the kaon divided according to spectrometer arm and bending direction
$\langle Rapidity_p \rangle$:SpecArm:Bend	Average rapidity of all tracks per selected event assuming the mass of the proton divided according to spectrometer arm and bending direction
$\langle Rapidity_{\pi}^{PID} \rangle$:SpecArm:Bend	Average rapidity of all identified pions per selected event divided according to spectrometer arm and bending direction
$\langle Rapidity_K^{PID} \rangle$:SpecArm:Bend	Average rapidity of all identified kaons per selected event divided according to spectrometer arm and bending direction
$\langle Rapidity_p^{PID} \rangle$:SpecArm:Bend	Average rapidity of all identified protons per selected event divided according to spectrometer arm and bending direction

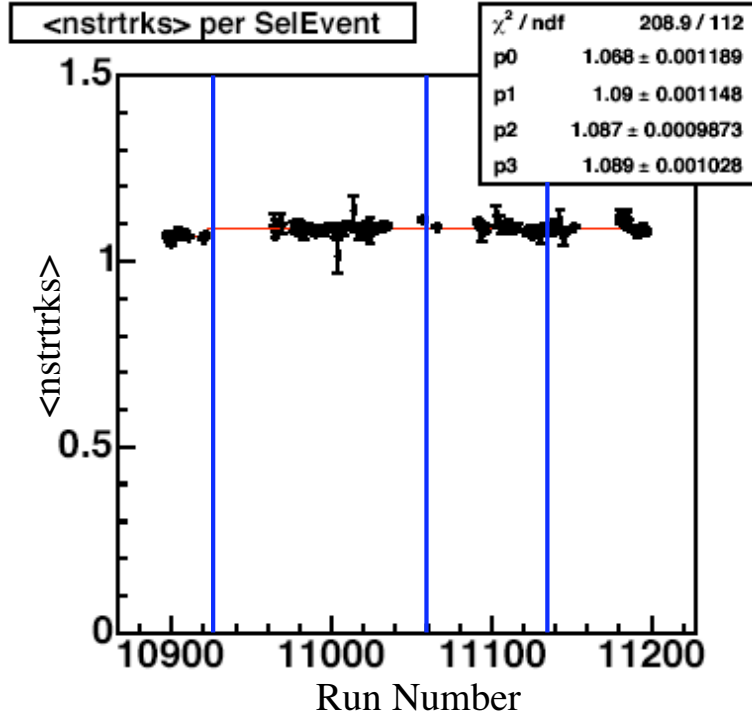


Figure 3.6: The average number of straight tracks found per selected event for the dAVertex data set. The blue lines show the divisions between the beam orbit regions. The red lines represent the constant fit to each beam orbit region. The fit parameters are shown in the upper right corner of the plot.

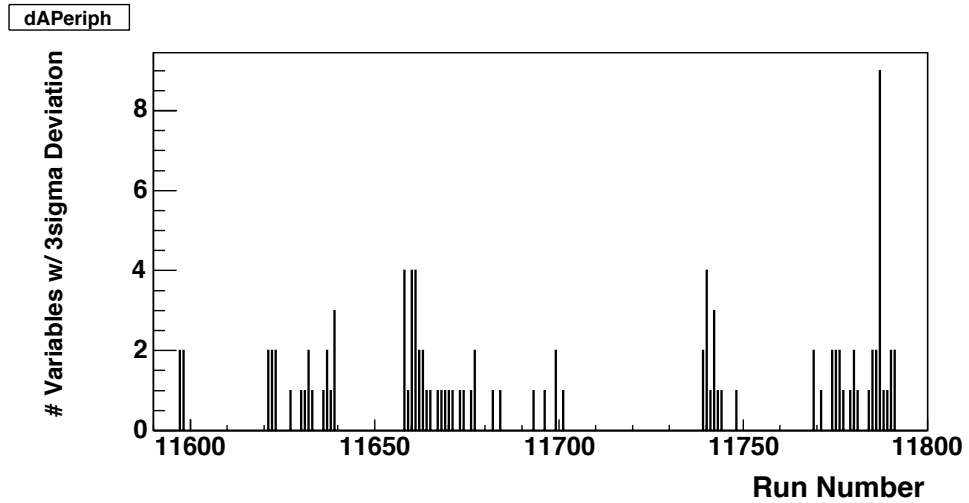


Figure 3.7: The number of times each run deviates by 3 or more sigma from the mean value of the data quality variables plotted versus run number for the dAPeriph data set.

Table 3.6: Runs from Each Data Set that Show Significant Deviation from the Mean Data Quality Parameters

Data Set	Run Number	Polarity	$\#3\sigma$	BO Region	% Events
dAVertex	11035	+	9	1	19 %
dAVertex	11057	+	9	1	9.4 %
dAVertex	10897	−	7	0	43 %
dAVertex	11180	−	7	3	3.5 %
dAPeriph	11787	+	9	1	5.0 %
dAPeriph	11658	+	4	1	1.0 %
dAPeriph	11660	+	4	1	5.0 %
dAPeriph	11661	+	4	1	2.0 %
dAPeriph	11740	+	4	1	6.0 %
ppVertex	12318	−	4	1	1.3 %
ppVertex	12216	−	3	1	5.0 %
ppVertex	12342	−	3	1	3.1 %
ppVertex	12226	−	2	1	6.0 %
ppVertex	12323	−	2	1	2.7 %
ppVertex	12328	−	2	1	7.9 %

3.4 Centrality Determination

One of the parameters that is commonly used to characterize a heavy ion collision is centrality. Centrality is used to describe the geometry of the collision. Figure 3.8 depicts a collision between a deuteron nucleus and a Au nucleus. The impact parameter b of the collision describes the distance between the centers of the two colliding nuclei. The number of participants N_{part} refers to the number of nucleons that participate in the collision and the number of collisions N_{coll} is the total number of nucleon-nucleon interactions that occur. Another variable used to measure centrality is the number of collisions experienced by each participating nucleon, ν . For the d+Au collision system, from the reference frame of the deuteron, ν is defined using the number of deuteron nucleons that participate in the collision, $\nu \equiv \frac{N_{coll}}{N_{part}^d}$.

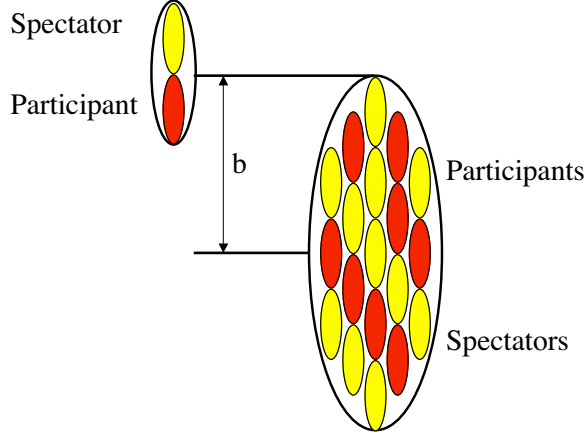


Figure 3.8: The geometry of a d+Au collision. The impact parameter, b , between the nuclei is shown. Participant nucleons take part in the collision while spectator nucleons do not interact.

For symmetric collision systems, such as Au+Au and p+p collisions, the number of collisions experienced by each participating nucleon is defined as $\nu \equiv \frac{N_{coll}}{N_{part}/2}$. Unfortunately, none of these variables are physically observable. In this analysis two independent techniques are used to determine collision centrality. The Ring Multiplicity Counters are used to relate the observed multiplicity of the collision to centrality and the Proton Calorimeter measures the amount of energy deposited by spectator and recoil protons.

3.4.1 Ring Multiplicity Counters

The Ring Multiplicity Counters measure the total energy deposited E_{Ring} and the number of incident particles N_{Ring} per collision. A signal is recorded when a silicon pad registers an energy greater than the noise threshold. The noise threshold of the Ring Counters is set at 30 keV . This value is approximately three times larger than the measured noise in the rings, 10.6 keV [48]. The d+Au experimental and HIJING

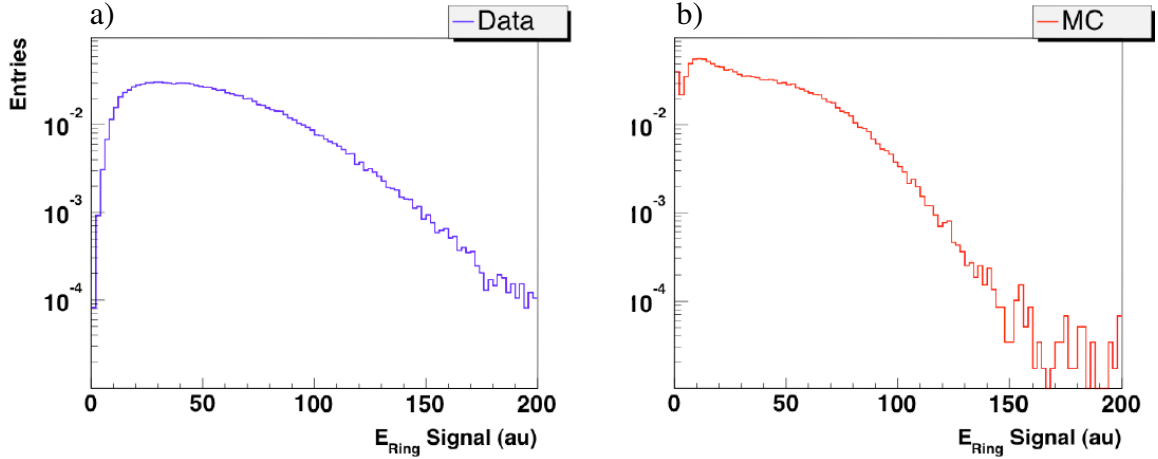


Figure 3.9: The energy distribution in the Ring Multiplicity Counters for the d+Au collision system. a) The distribution observed in the dAVertex triggered data. b) The HIJING Monte-Carlo distribution.

Monte-Carlo energy distributions in the Ring Counters are shown in Fig. 3.9. These distributions are used to determine the positions of the centrality bin cuts and the corresponding average collision geometry in each centrality bin. This correlation is possible because E_{Ring} scales monotonically with the number of collisions, as shown in Fig. 3.10.

Centrality cuts are used to divide the data into bins that represent the degree of overlap between the two colliding nuclei. For example, the 0-10% bin includes those events that experience the most central collisions. Central collisions deposit large amounts of energy in the Ring Counters and thus appear at the high end of the E_{Ring} distribution. In contrast, peripheral collisions deposit very little energy in the Ring Counters and appear at the lower end of the distribution. The probability of two nuclei interacting in a peripheral collision is much greater than that of a central collision. This trend is observed in the Monte-Carlo distribution shown in Fig. 3.9b.

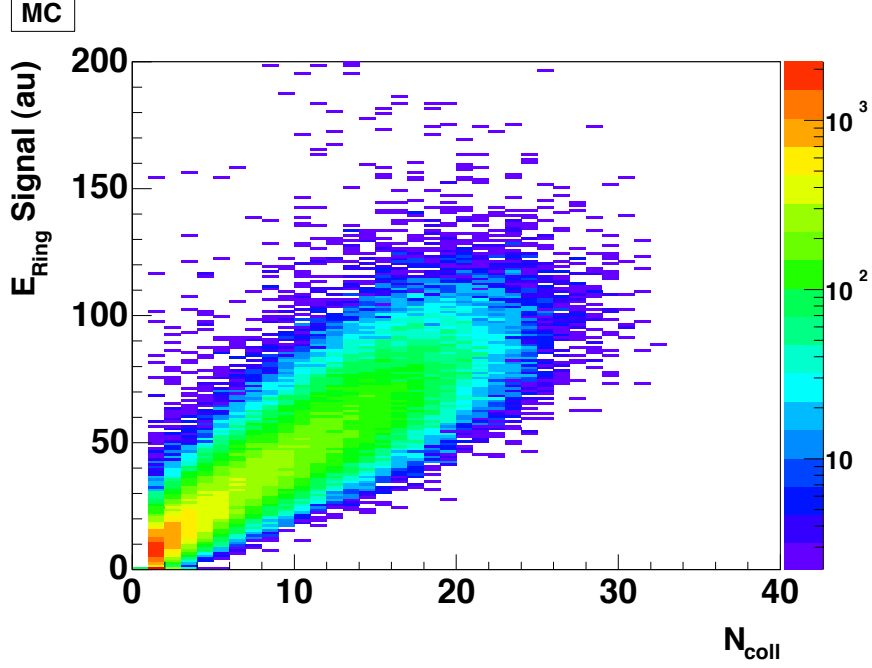


Figure 3.10: The HIJING Monte-Carlo energy distribution in the Ring Multiplicity Counters plotted versus the number of collisions N_{coll} in a d+Au collision.

However, the distribution from the data, shown in Fig. 3.9a, does not include as many peripheral events as does the Monte-Carlo distribution. This is a result of the inefficiency of the trigger. Because peripheral events have a low multiplicity, they frequently do not produce a trigger.

The positions of the centrality bin cuts are first found using Monte-Carlo events, because this sample is not affected by the trigger and vertexing inefficiencies. In the d+Au analysis four centrality bins are used. They correspond to 0-10%, 10-30%, 30-60% and 60-100% of the unbiased total collision cross section. The bins are referred to as central, mid-central, mid-peripheral and peripheral, respectively. The Monte-Carlo E_{Ring} distribution is then scaled to match the distribution observed in the data and the corresponding cut positions are found. These are the cuts that are

Table 3.7: Centrality Cuts Used for the d+Au Collision System

Bin		%	Data Cuts	MC Cuts
Peripheral	least central	60-100%	0.0 - 22.0	0.0 - 23.0
Mid-Peripheral	:	30-60%	22.0 - 50.3	23.0 - 47.8
Mid-Central	:	10-30%	50.3 - 84.3	47.8 - 72.4
Central	most central	0-10%	$84.3 - \infty$	$72.4 - \infty$

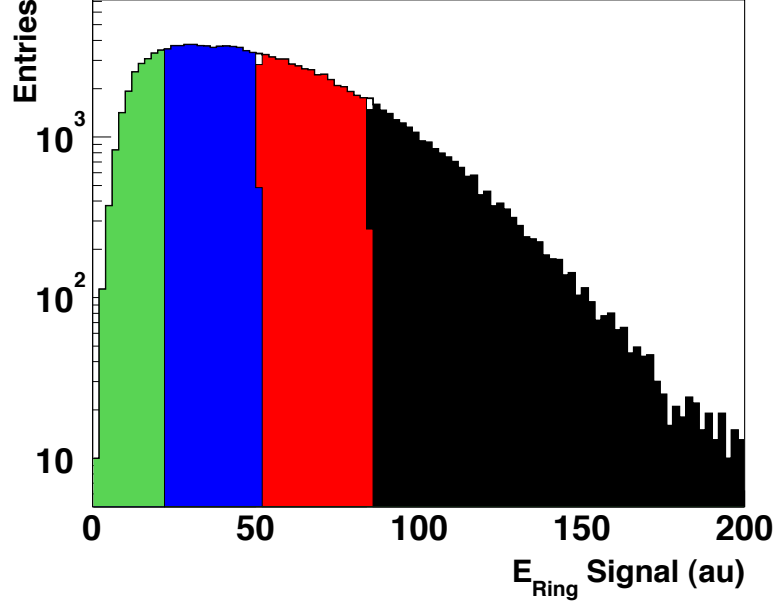


Figure 3.11: The experimental dAVertex E_{Ring} distribution divided into centrality bins. The central bin is shown in black, the mid-central bin is red, the mid-peripheral bin is blue, and the peripheral bin is green.

used throughout the analysis. Table 3.7 contains the details of the cuts used for the dAVertex and dAPeriph triggered data sets and Fig. 3.11 shows the cuts applied to the experimental dAVertex E_{Ring} distribution.

The average number of collisions experienced by each participating nucleon in each centrality bin is calculated using simulated HIJING Monte-Carlo events for which N_{coll} and N_{part}^d are known. In order to accurately represent the data, the trigger and vertexing efficiencies ϵ observed in the data are applied to the Monte-

Table 3.8: Average Centrality Variables for Each Centrality Bin

Trigger	%	$\langle\epsilon\rangle$	$\langle N_{coll}\rangle$	$\langle N_{part}\rangle$	$\langle b\rangle$	$\langle\nu\rangle$
dAVertex	60-100%	0.20	2.9(1.7)	3.5(1.3)	7.4(1.4)	2.2(1.3)
dAVertex	30-60%	0.61	7.0(3.0)	8.2(2.4)	5.6(1.5)	4.0(1.8)
dAVertex	10-30%	0.78	12(3.6)	13(2.8)	4.0(1.5)	6.1(1.8)
dAVertex	0-10%	0.84	16(4.0)	17(3.6)	3.0(1.4)	8.1(2.0)
dAPeriph	60-100%	0.18	2.8(1.7)	3.5(1.3)	7.4(1.4)	2.2(1.3)
dAPeriph	30-60%	0.24	6.2(2.7)	7.3(2.2)	5.9(1.6)	3.7(1.6)

Carlo events. Table 3.8 shows the results for each centrality bin. The average trigger and vertex efficiency $\langle\epsilon\rangle$, the average number of binary collisions $\langle N_{coll}\rangle$, the average number of participants $\langle N_{part}\rangle$, the average impact parameter $\langle b\rangle$, and the average number of collisions per deuteron participant $\langle\nu\rangle$ are shown for each centrality bin. The numbers in parentheses represent the RMS of their respective values and the systematic errors in these quantities are 30%, 20%, 15%, 10% from peripheral to most central. The supplementary trigger requirements applied to the dAPeriph data set remove more central events and result in slightly different average values in the mid-peripheral bin compared to the dAVertex data set.

3.4.2 Proton Calorimeter

The Proton Calorimeter provides a multiplicity independent method for determining collision centrality and is used as a cross check of the values obtained from the Ring Multiplicity Counters. The Proton Calorimeter measures the energy deposited by the spectator and recoil protons produced in each collision. The signal observed in the detector modules scales monotonically with centrality [49]. This relationship is shown in Fig. 3.12.

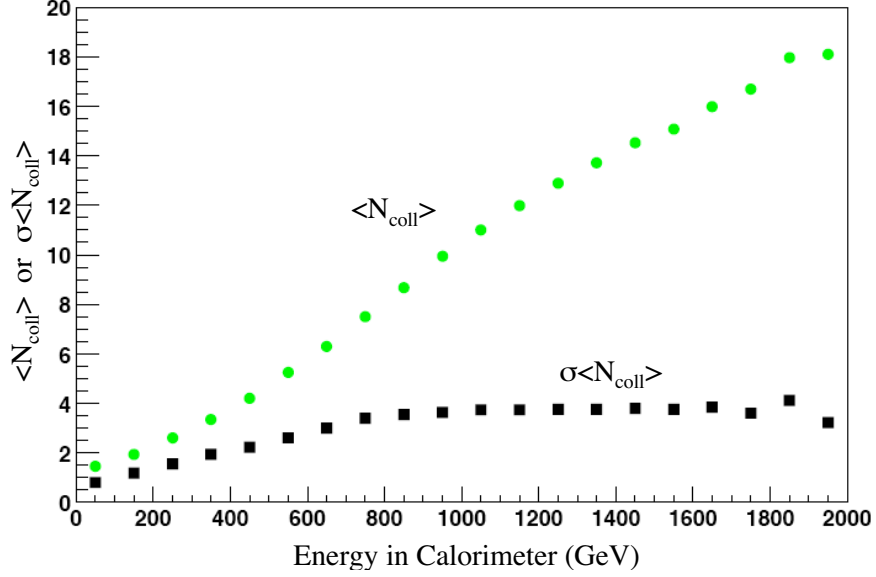


Figure 3.12: Number of binary collisions, N_{coll} , versus the total energy deposited in the Proton Calorimeter. The black squares represent the RMS of the measurement of N_{coll} . [49]

The centrality bin cut positions are found using the sum of the raw Analog to Digital Converter, ADC, signals of the two modules that receive the largest energy deposition in the negative calorimeter. These modules are referred to as modules [4,0] and [5,0]. The first term represents the vertical position of the module in the calorimeter array and the second term represents the horizontal position with respect to the axis of the beam. The blue curve in Fig. 3.13 shows the energy distribution observed in modules [4,0] and [5,0]. A toy Monte-Carlo model is used to relate the experimental energy distribution to collision centrality. The unbiased, scaled toy Monte-Carlo distribution is shown in Fig. 3.13 in pink and the model distribution with trigger and vertexing inefficiencies applied is shown in red. A multiplicative scale factor of 0.38 is applied to the model distribution to match the experimentally observed magnitude.

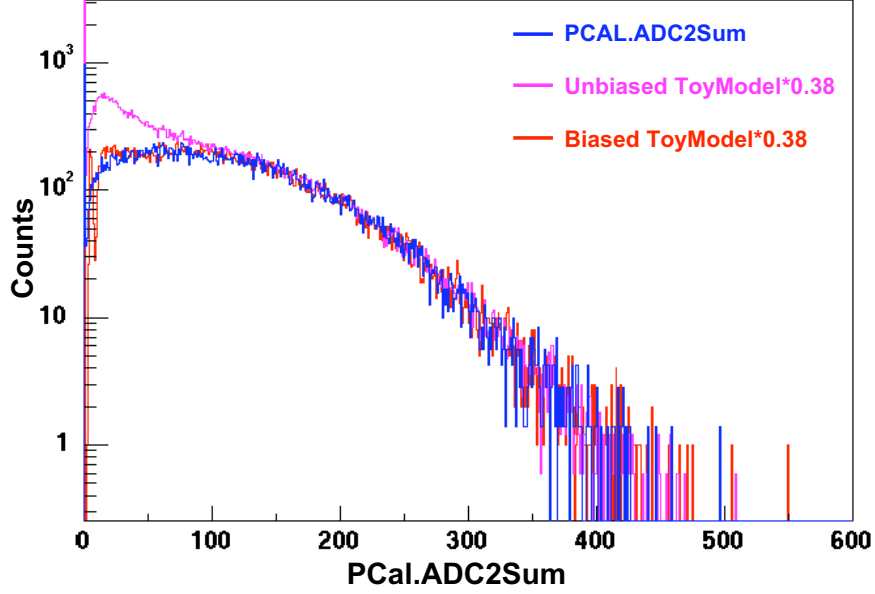


Figure 3.13: Experimental and scaled toy Monte-Carlo energy distributions for Proton Calorimeter modules [4,0] and [5,0]. The blue curve represents the raw experimental distribution, the pink curve shows the unbiased, scaled toy Monte-Carlo distribution, and the red curve shows the scaled toy Monte-Carlo distribution to which trigger and vertexing inefficiencies have been applied.

The centrality bin cuts are determined for the Proton Calorimeter in an analogous manner to that used in the Ring Multiplicity Counter method. First, the model distribution is divided into percentage centrality bins. Next, the model distribution and centrality bin cut positions are scaled to match the experimentally observed energy distribution. Finally, the average collision centrality of each bin is calculated from the simulated model events. The results of this procedure are shown in Table 3.9. The numbers in parentheses represent the RMS of their respective values and the systematic errors in these quantities are 30%, 20%, 15%, 10% from least central to most central, respectively. The results differ little from those found using E_{Ring} .

Table 3.9: Centrality Cuts and Average Number of Participants $\langle N_{part} \rangle$ Determined Using the Proton Calorimeter

Trigger	%	Data Cuts	MC Cuts	$\langle N_{part} \rangle$
dAVertex	60-100%	0 - 41	0.00 - 25.3	3.7(1.6)
dAVertex	30-60%	41 - 110	25.3 - 54.9	8.3(3.2)
dAVertex	10-30%	110 - 190	54.9 - 85.9	13(3.7)
dAVertex	0-10%	190 - ∞	85.9 - ∞	16(3.9)
dAPeriph	60-100%	0 - 41	0 - 25.3	3.7(1.6)
dAPeriph	30-60%	41 - 110	25.3 - 54.9	7.4(2.9)

Chapter 4

Particle Tracking

The particles produced in a collision that traverse the PHOBOS two arm magnetic spectrometer can be tracked and identified. Each time the particle interacts with the silicon of the spectrometer a *hit* is recorded. In each collision event many hits are recorded in the spectrometer, as shown in Fig. 4.1. These hits are generated by primary collision products, secondary collision products and background particles. The track reconstruction algorithm is used to associate all of the hits generated by a single particle. The reconstruction requires three separate steps. First, hits deposited in the magnetic field free region of the spectrometer are analyzed to determine straight track candidates. Next, curved track candidates are found by associating hits in the field on region. Finally, straight and curved track candidates are matched to generate full tracks and the properties of the track are

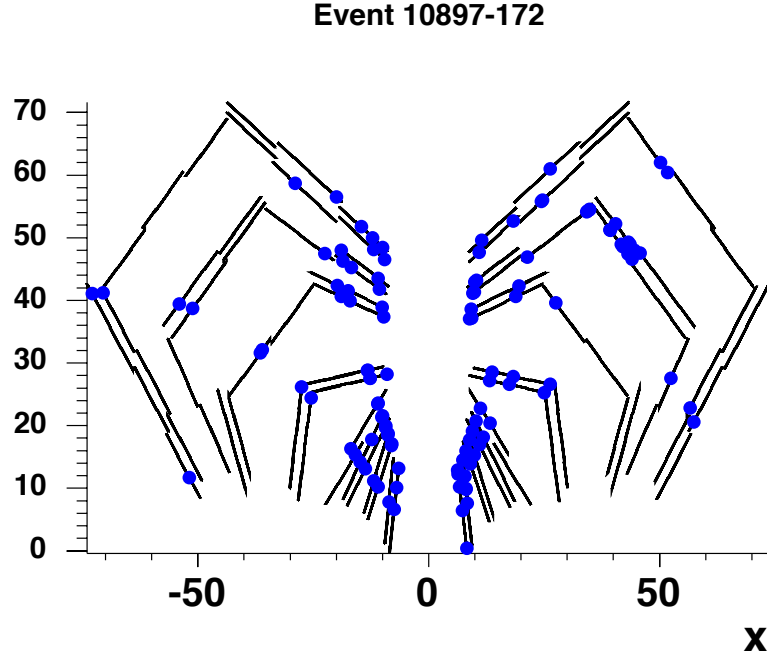


Figure 4.1: Hits recorded in the spectrometer for d+Au collision event 10897-172.

determined. The details of the track reconstruction algorithm are described in the following sections. The same tracking algorithms are used to reconstruct tracks in both the d+Au and p+p data sets.

4.1 Magnetic Field

The operating principal of a magnetic spectrometer is that the curvature of the track of a charged particle in a magnetic field is dependent upon both the charge, q , and the momentum, p , of the particle. The direction of curvature of the track reveals the charge sign of the particle and the radius of curvature can be used to measure the momentum of the particle. Track reconstruction requires knowledge of the initial straight line trajectory of the track prior to when the particle enters the

magnetic field. Therefore, in order to both track and identify particles they must pass through two distinct magnetic field regions.

Figure 4.2 shows the magnitude of the y-component of the magnetic field (at $y=0$) at the position of each spectrometer layer. The spectrometer layers, or planes, are identified sequentially by the letters shown in Fig. 4.2. Layers A-F are positioned in the field free region. Hits in these layers are used to reconstruct straight tracks. Layers K-P sit predominantly within a constant field of $\pm 2.18\text{ T}$ and are used to measure curved tracks. The field strength along the axis of the beam, the z-axis, is zero to minimize the effect of the magnetic field on the orbit of the beam. The PHOBOS magnet is a reversible double dipole design; therefore, the two spectrometer arms sit in opposite polarity fields. Approximately half of the data used in this analysis was collected using the magnetic field configuration shown in Fig. 4.2 and the other half was collected using the reverse polarity configuration.

4.2 Straight Tracking

Straight tracks are reconstructed by combining series of hits found in layers A-F of the spectrometer that extrapolate back to the orbit of the beam. The two colliding beams that circulate in the RHIC ring are tuned to provide collisions at the nominal interaction point ($x=0$, $y=0$, $z=0$) of the experiment. However, because the beams consist of tightly bunched groupings of nuclei, they have a finite dispersion in the xy-plane. When the beams cross, nucleus-nucleus collisions occur throughout this region, which is referred to as the collision diamond. Figure 4.3

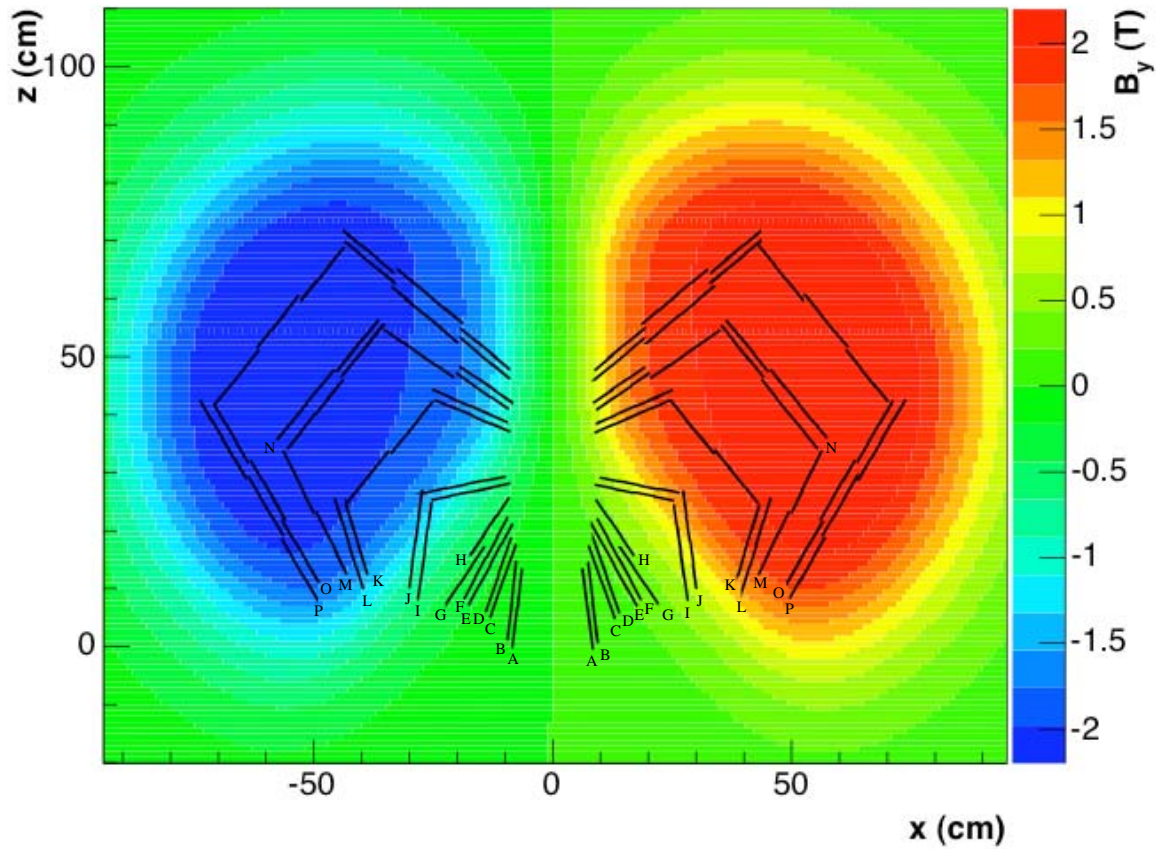


Figure 4.2: The y-component of the magnetic field (at $y = 0$) in the region of the spectrometer. Each layer of the spectrometer is identified using the letters shown next to the layer.

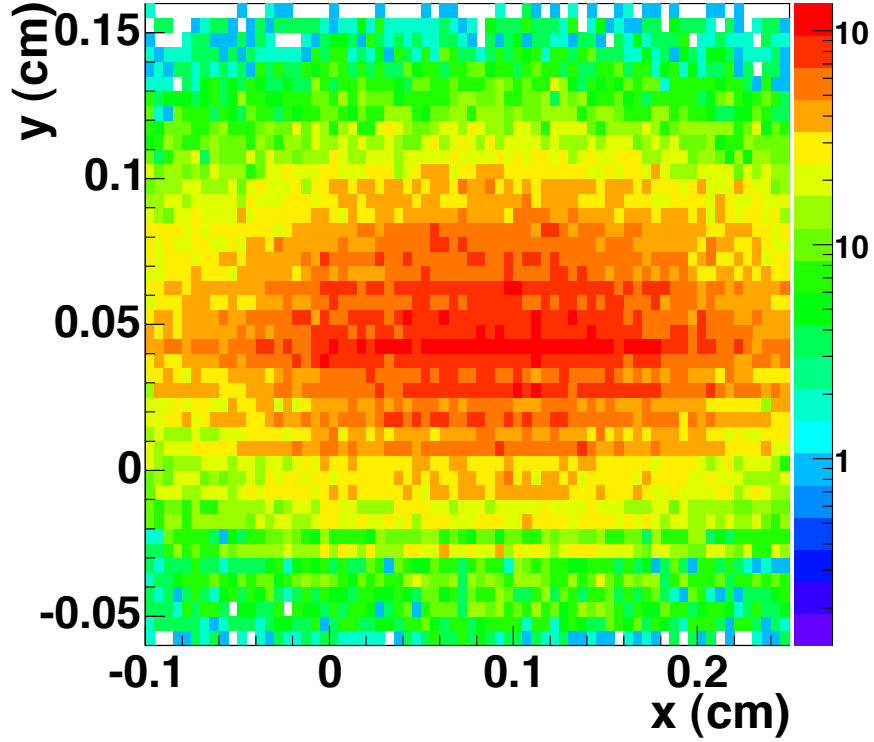


Figure 4.3: The reconstructed x and y collision vertex positions for a subset of the d+Au data set. A Gaussian fit of the x and y distributions gives the experimental beam orbit position.

illustrates the transverse cross section of the collision diamond. A Gaussian fit of the x and y coordinates of this cross section gives the mean position of the beam orbit. The beam orbit is calculated for each stable data collection period and is highly dependent upon the tune of the colliding beams.

The algorithm used to generate straight track candidates begins by finding all possible 2-hit combinations in spectrometer layers A and D that extrapolate back within 2.5 *cm* of the beam orbit. These are referred to as track seeds. For each seed, hits are found in the other spectrometer layers (B,C,E,F) that lie along the extrapolated line of the track. In spectrometer layers B and C, the hit which lies closest to the track is added to the track's hit list. In spectrometer layers E and F,

the hit which lies closest to the track and has an offset in the yz -plane that is less than the size of the silicon pad is added to the track's hit list. This additional cut requires that the hit lie in the correct vertical pad and accounts for the increased pad size in layers E and F. Only reconstructed tracks that contain a minimum of 4 hits are kept; therefore, all generated track seeds do not necessarily result in a straight track.

After constructing tracks from track seeds generated in layers A and D, a second set of seeds is produced using those hits in layers C and D that have not already been assigned to tracks. Hits in layers E and F are assigned to these tracks based upon the same criteria stated previously. Tracks reconstructed using this method have exactly 4 hits.

In the dAVertex data set an average of 1.1 straight tracks are found per selected event. This value falls to an average of 0.59 for the dAPeriph data set. In the p+p collision system, the average number of straight tracks found per selected ppVertex triggered event is 0.31. The observed trend (dAVertex>dAPeriph>ppVertex) is a result of the decreasing mean multiplicity of triggered events in each data set. The straight tracks found in the representative d+Au collision event are shown in red in Fig. 4.4.

4.3 Curved Tracking

The curvature of each charged particle track in the magnetic field must be measured to determine the charge sign, q , and momentum, p , of the particle. Due to the

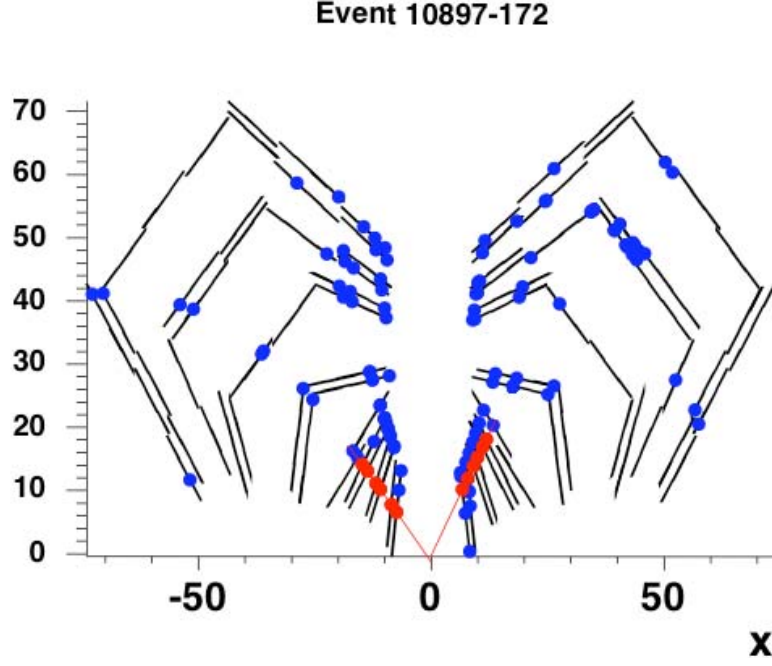


Figure 4.4: The reconstructed straight tracks found in d+Au collision event 10897-172.

geometry of the magnetic field, it is not possible to reconstruct tracks using an analytical track model, because layers A-F of the spectrometer lie in the field free region while layers K-P lie in the magnetic field. Instead, a Hough transform method [50] is used to relate the properties of a series of associated hits with variables that characterize the track as a whole. The track variables that are used are the inverse of the total momentum of the particle, $1/p$, and the angle at which the particle is produced with respect to the beam axis in the xz -plane, θ_0 . To make this conversion, two angles are determined for each pair of hits in a curved track, θ and α . The angle θ is defined with respect to the beam axis by the angle of the line extending from the collision vertex to the first hit in the track pair, as shown in green in Fig. 4.5. The angle between the line connecting the pair of hits and the line connecting the first

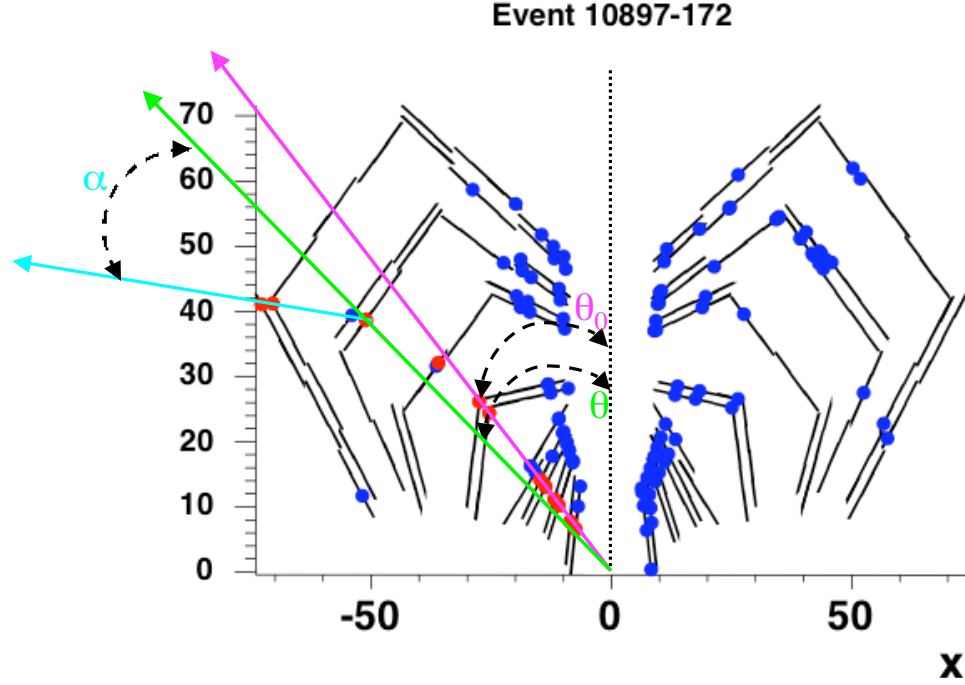


Figure 4.5: The angles θ_0 , θ and α defined for a hit pair in d+Au collision event 10897-172. The pink line represents the angle at which the particle is produced with respect to the beam axis. The green line extends from the collision vertex to the first hit in the track pair in layers (M,O). The blue line connects the hits between layers M and O.

hit with the event vertex is defined as α , see the blue line in Fig. 4.5. In practice, it is not practical to calculate the Hough parameters for each event. Instead, single track simulations are used to generate look up tables that translate (θ, α) coordinates into $(\theta_0, 1/p)$. These tables are referred to as Hough tables.

The curved tracking algorithm first steps through each spectrometer layer and generates pairs of hits, which are referred to as Hough sticks. The pairs of layers used are dependent upon whether the track traverses the central part of the spectrometer or the outer wing. For the central part of the spectrometer, Hough sticks are generated sequentially in layers (I,J), (J,K), (K,M), (M,N) and (N,O). For the outer wing of the spectrometer, Hough sticks are generated for pairs of hits in

layers (I,J), (J,K), (K,M), (M,O) and (O,P). For each Hough stick the coordinates of the two hits are used in conjunction with the vertex position to determine θ and α . The Hough tables are then used to determine the $1/p$ and θ_0 values associated with the stick.

After generating the individual Hough sticks, the curved tracking algorithm assembles the sticks into Hough chains. Chains are constructed from all sticks that contain overlapping hits, i.e. the last hit in the first stick is the same as the first hit in the second stick. Each time a stick is added to a chain the charge, momentum and angle properties of the stick must match those of the chain. The overall momentum and angle parameters of each curved track are the weighted averages of the individual stick values. A completed Hough chain contains 5 Hough sticks, one from each of the pairs of layers. Chain candidates that are missing one or more Hough sticks are discarded; therefore, all accepted chains contain exactly 6 hits. Finally, a series of selection cuts are applied to completed chains to ensure that the accepted chains meet a minimum quality level. These cuts restrict the vertical displacement of the hits and are determined based upon the vertical segmentation of the last layer of the spectrometer.

4.4 Straight and Curved Track Matching

Full tracks are reconstructed by matching straight tracks with curved tracks. Due to the low multiplicity of the d+Au and p+p collision environments it is not possible to reconstruct an event vertex for each collision. Instead, a line is extrapolated from

Table 4.1: Track Matching Criteria

Condition	Central Region	Outer Wing
$\Delta\theta$	0.015	0.03
$\Delta(dE/dx)$	0.8	0.8
χ^2	1.25	3.0
χ_y^2	5.0	5.0

each straight track to the beam orbit. This vertex is used to match straight tracks with Hough chains. The track matching code loops over each straight track and calculates the straight line fit probability of the track. If the fit probability exceeds a value of 0.01 the straight track is accepted and the search begins for a matching Hough chain.

A straight line track and Hough chain are matched if the joined track meets four criteria, the details of which are given in Table 4.1. The limiting cut values are dependent upon whether the track is reconstructed in the central part of the spectrometer or the outer wing. The inner wing, situated closest to the beam pipe and subject to the largest background contamination, has not yet been implemented in the tracking. The angle, θ , and the truncated mean energy deposition, dE/dx , of the straight and curved tracks must not differ by more than a maximum value. In addition, the χ^2 and the χ_y^2 fits of the track must not exceed a maximum value. The value of χ^2 is a measure of the track quality and the χ_y^2 fit is a measure of the deviation of the Hough chain from the straight track in the vertical, y , direction.

Combinations of straight and curved tracks that pass the selection criteria are saved. The matched tracks for the representative d+Au collision event are shown in red in Fig. 4.6. The preliminary momentum vector of the matched track is

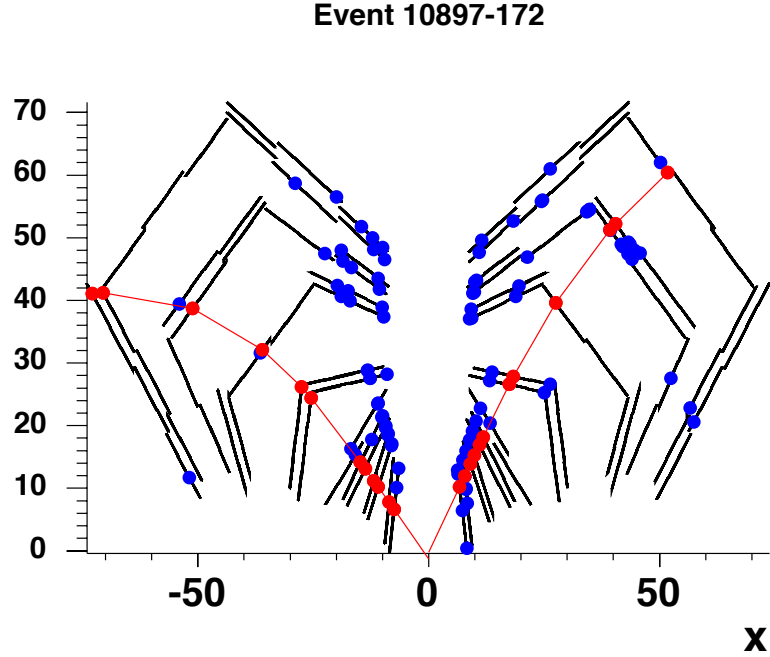


Figure 4.6: The reconstructed matched tracks found in d+Au collision event 10897-172.

determined from the angle of the straight line track and the total momentum of the Hough chain. The energy deposition, dE/dx , of the combined track is assigned based upon the truncated mean of the energy deposition of all of the hits that compose the track.

Reconstructed tracks are only allowed to contain a maximum of 2 overlapping hits and must have a total of 11 hits. These restrictions require that an additional level of selection criteria be applied to track candidates after the straight and curved tracks have been matched. Joined tracks containing fewer than 11 hits are discarded. If multiple tracks share more than 2 hits, the track which possesses the highest fit probability is accepted. An explanation of how the fit probability is determined can be found in Sec. 4.5.4. In the d+Au collision system only 12% of events contain 2 or

more tracks in the spectrometer. Of these events, 25% are found to have overlapping tracks; therefore, overall 3% of all matched tracks are rejected by this cut.

4.5 Momentum Reconstruction

The final step in the tracking procedure is the determination of the momentum vector for each reconstructed track. This is commonly done using an analytical track model and a simple χ^2 fit. The definition of χ^2 is based upon the assumptions that the measurements being related are uncorrelated and the errors in the measurements are Gaussian. Because the PHOBOS spectrometer contains silicon layers in a field free region, a field gradient and a 2 T magnetic field, an analytical track model cannot be used. In addition, multiple scattering induced in one layer of silicon affects subsequent layers; therefore, the measurements are correlated. Furthermore, the pixel segmentation in the silicon sensors and multiple scattering both generate non-Gaussian errors in the hit measurements. Thus, it is necessary to implement a numerical calculation of the trajectory of each track.

4.5.1 Numerical Track Model

A first order estimate of the track trajectory in the applied magnetic field is determined using the preliminary momentum vector calculated when the curved and straight tracks were joined. The particle is *swum* through the magnetic field and the path of the particle is predicted based upon the influence of the field strength. The fit algorithm uses a fixed step size of 10 cm in the central part of the spectrometer

and a variable step size in the outer wing that is dependent upon the momentum of the particle, $step [cm] = 2.5 cm + p [GeV]$. In the field gradient region the step size is reduced by half. A variable step size is used in the outer wing to accommodate particles that spend a large fraction of their trajectory in the field gradient region. Tracks that grossly deviate from the predicted trajectory are rejected using a residual RMS cut. In the central part of the spectrometer a maximum residual RMS of $0.04 cm$ is allowed, and a maximum of $0.12 cm$ is allowed in the outer wing.

4.5.2 Covariance Matrices

In addition to being influenced by the magnetic field, a particle that passes through the spectrometer is also affected by multiple scattering and energy loss. These affects are accounted for using a covariance matrix. The diagonal elements of the matrix represent the magnitude of the displacement between the track of a real particle and an ideal track. The off diagonal elements contain an estimate of the correlations between displacements in separate spectrometer layers. The correlation of the χ^2 fit parameters is omitted.

In the track fitting procedure, the covariance matrices are stored in a lookup table. A lookup table exists for each bin in phase space in the acceptance of the spectrometer. The bins are shown in Table 4.2. The covariance matrices are generated using 5000 randomly simulated tracks in each bin. First, the ideal trajectory of each track in the magnetic field is determined. Then a pion with the same initial parameters is swum through a GEANT simulation of the detector. The path

Table 4.2: Covariance Matrix Bins

Parameter	Range	Number of Bins
q	-1 - 1	2
$1/p_{tot}$	0.1 - 10	40
θ	0.25 - 1.75	30
$zvertex$	-20 - 10	60

of the simulated track incorporates the effects of pixelization, multiple scattering and energy loss. Finally, the residuals of the simulated track relative to the ideal trajectory are calculated. These values are used to fill the covariance matrices.

The amount of energy a particle loses as it interacts with the detector material is dependent upon both the mass of the particle and its momentum. Because the covariance matrices are generated using simulated pions, the energy loss of heavier particles is underestimated. This leads to an underestimation of the total momentum of reconstructed low momentum kaons and protons. The magnitude of this difference for protons is shown in Fig. 4.7, where the ratio of the reconstructed and true momenta is plotted versus the true momentum for simulated protons. In this analysis, the proton momentum acceptance extends down to 300 MeV . At this point the deviation of the reconstructed proton momentum from the true momentum is 10% and rapidly approaches zero as the momentum increases. The effect observed in the kaon momentum distribution is less than that of the protons because the mass of the kaon is closer to that of the pion than is the mass of the proton. Because the underestimation of the energy loss of protons and kaons is small in the acceptance range of the particle ratios measurement, it is not necessary to correct for the difference between the reconstructed and true momenta.

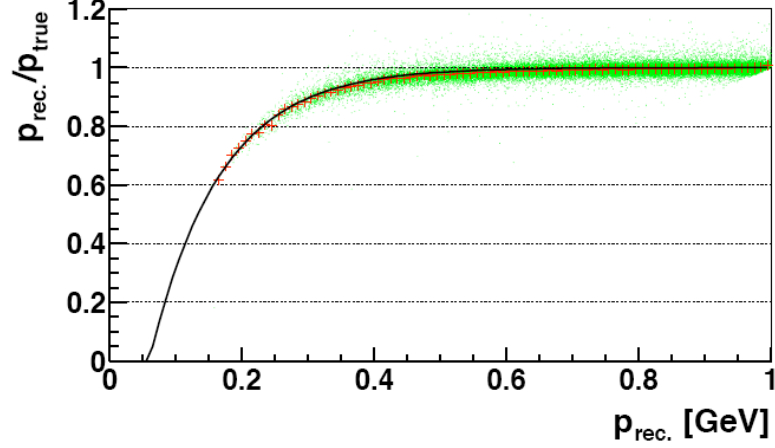


Figure 4.7: The ratio of the reconstructed and true momenta versus true momentum for simulated protons.

4.5.3 χ^2 Minimization

The parameters that characterize the trajectory of each particle are found using a χ^2 fitting routine that incorporates not only the affect of the magnetic field, but also multiple scattering and energy loss through the use of the covariance matrices. Because an analytical track model is not available, the Simplex minimization method is used. This technique utilizes a geometrical figure, referred to as a simplex, that contains $N+1$ points in N dimensions. Thus in three dimensional space the simplex figure is a tetrahedron. The initial positions of the simplex points are chosen randomly around the preliminary track parameters determined from the numerical track model, see Sec. 4.5.1. The fitting routine then minimizes the value of χ^2 by moving the simplex point that has the highest χ^2 through the opposite face of the simplex and contracting the volume of the figure. When the incremental improvement falls below a minimum value the fitting routine is terminated.

The trajectory of a particle in the PHOBOS spectrometer is characterized by

Table 4.3: Particle Trajectory Parameters

Parameter	Description
$1/p_{tot}$	track curvature
θ_0	track emission angle in the bending plane
z_0	the z coordinate at $x = 0$
ϕ	the dip angle perpendicular to the bending plane
y_0	the y coordinate at $x = 0$

the 5 parameters shown in Table 4.3. These parameters can be divided into two categories: those which characterize the track in the bending plane ($1/p_{tot}$, θ_0 and z_0), and those which characterize the track out of the bending plane (ϕ and y_0). The bending plane is defined in spatial coordinates as the xz-plane. The parameters in the bending plane are determined from the χ^2 fit. The parameters out of the bending plane are calculated from the hits found in the first 6 layers of the spectrometer, due to the poor vertical resolution of the outer spectrometer layers.

4.5.4 Fit Probability

The fit probability of a track represents the confidence level to which the fit parameters determined using the χ^2 minimization procedure describe the hit pattern of the given track. The fit probability is calculated using the known χ^2 probability distribution function $f(\chi^2)$, which is dependent only upon the number of degrees of freedom of the fit if Gaussian errors are assumed. For an ideal system, the distribution of the fit probability should be flat. Due to large angle scattering and the minimization routine converging on localized minima, the fit probability distribution in real tracks possesses a large peak at zero, as shown in Fig. 4.8. Tracks with a

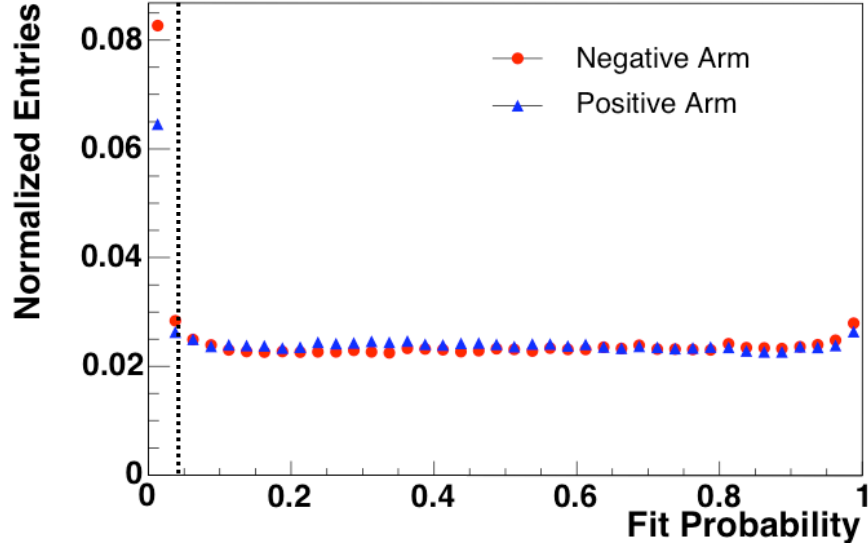


Figure 4.8: Fit probability distribution for tracks reconstructed from the data in the negative and positive spectrometer arms.

low fit probability are not removed in the track reconstruction procedure; however, a cut is applied in the analysis software that requires the fit probability be greater than 0.04, as indicated by the dashed line in Fig. 4.8.

4.6 Track Reconstruction Efficiency

The efficiency of the track reconstruction procedure is analyzed by reconstructing simulated single tracks that are generated within the acceptance of the spectrometer.

The reconstruction efficiency plotted as a function of transverse momentum, p_T , is shown in Fig. 4.9. A maximum efficiency of 94% is achieved at $p_T = 600$ MeV/c.

The efficiency at all momenta is stable and remains above 80%. Studies have shown that the reconstruction efficiency of simulated single tracks is slightly higher than that achieved in the data due to the fact that more than one track may be present

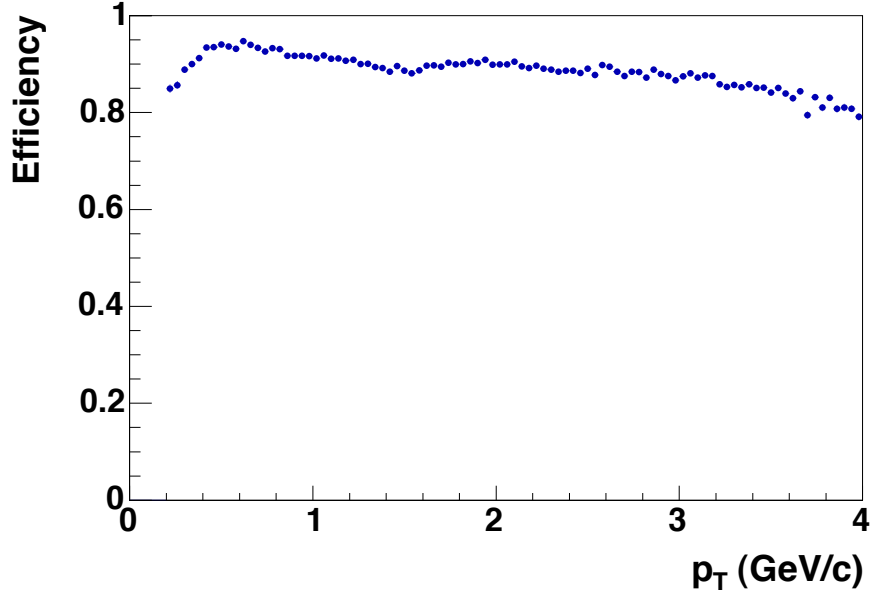


Figure 4.9: Track reconstruction efficiency plotted as a function of p_T .

in the spectrometer per event [51]. This effect is negligible in the d+Au and p+p collision systems because multiple tracks are rarely found in an event. Figure 4.10 shows the distribution of the number of tracks found per event for the d+Au and p+p collision systems. In both systems no more than 2 tracks are found per event and more than 90% of all events contain no tracks.

4.7 Momentum Resolution

The momentum resolution of the track reconstruction procedure is determined using the same simulated single tracks that are used for the track efficiency study. The momentum resolution of tracks with a fit probability greater than 0.04 is shown in Fig. 4.11 using the tracking procedure from the 2003 run. The resolution ranges from a minimum of 1% at 600 MeV/c to a maximum of 2.6% at 4 GeV/c. The

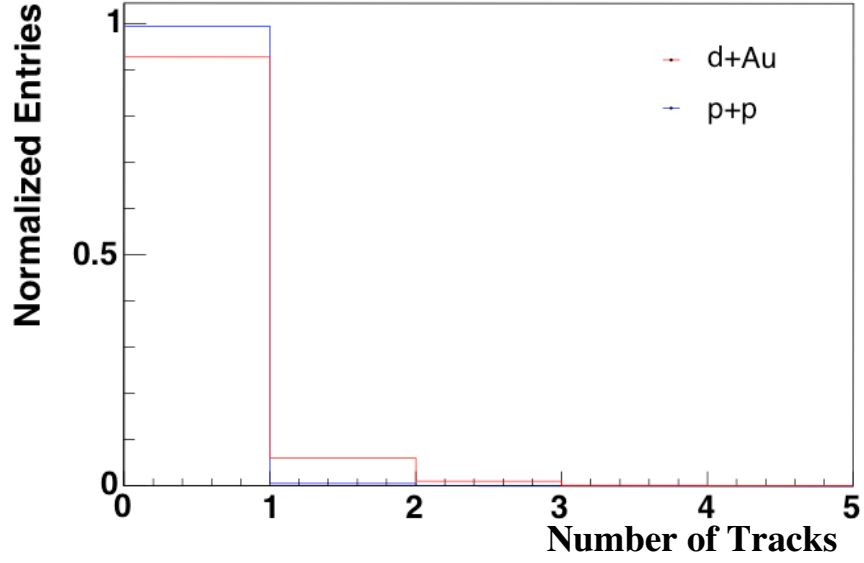


Figure 4.10: The number of tracks found per event in d+Au (red) and p+p (blue) collisions.

bumps observed in the distribution are statistically significant and are a result of the χ^2 minimization (Sec. 4.5.3) converging on local minima instead of the true minimum. When the number of minimization iterations is increased from 1 to 5 the structure is removed, as is shown in Fig. 4.12. This change was implemented in the 2004 run, but was not implemented for this analysis.

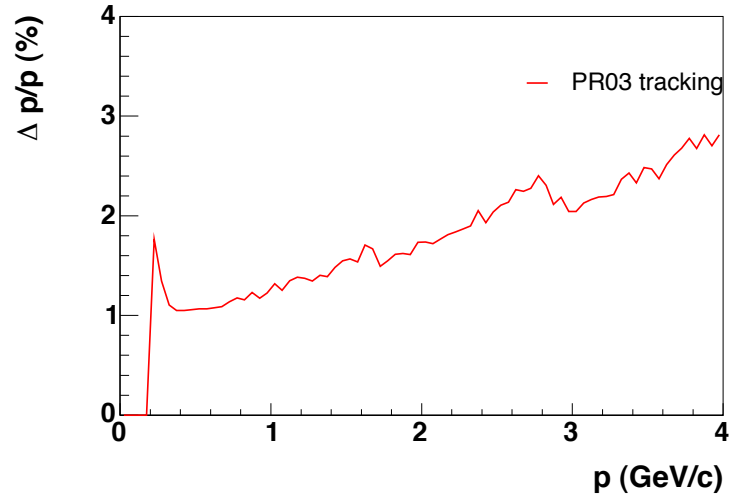


Figure 4.11: The momentum resolution of the track reconstruction plotted as a function of momentum for the PR03 tracking procedure.

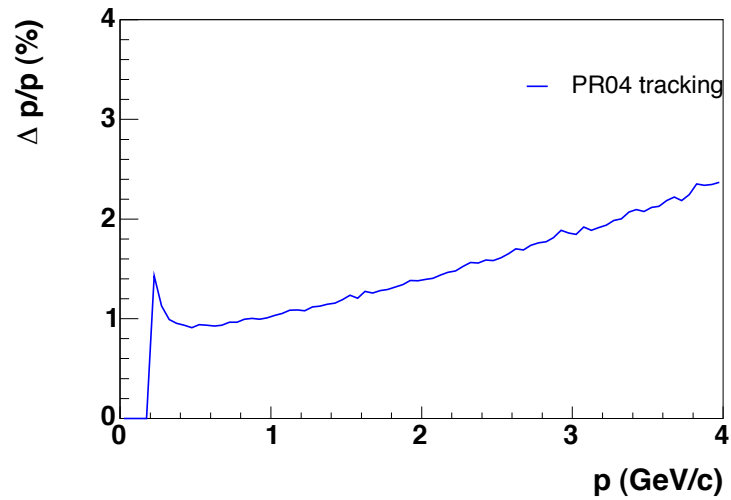


Figure 4.12: The momentum resolution of the track reconstruction plotted as a function of momentum for the PR04 tracking procedure.

Chapter 5

Particle Identification

Each track that is reconstructed in the spectrometer is uniquely characterized by two variables: momentum and energy deposition in the silicon detectors. The determination of the momentum of the particle has been discussed in detail in Chapter 4. The amount of ionization produced by the particle as it passes through the spectrometer provides a measure of the energy deposition. These two pieces of information, the momentum and the energy deposition, are sufficient to differentiate between pions, kaons and protons in the PHOBOS spectrometer. The same particle identification procedure is used for both the d+Au and p+p data sets.

5.1 Energy Loss in Matter

As the charged particles produced in a heavy ion collision traverse a detector they interact with its constituent material and transfer energy into the detector. The most common form of interaction is between the incident particle and atomic electrons in the detector materials. This interaction results in ionization or excitation of the detector material. The probability of interaction is statistical and can be characterized by the average amount of energy lost per unit path length, dE/dx . Experimentally dE/dx is measured in units of minimum ionizing particles, MIPS. A MIP is defined as the minimum value of the dE/dx for a given material and is applicable to particles traveling at relativistic velocities, $\geq 0.9c$ [52].

5.2 Bethe-Bloch Prediction

The mean rate of energy loss of a particle due to ionization in an absorber is described by the Bethe-Bloch formula, Eq. 5.1 [53]. It is dependent upon both the momentum of the incident particle and the physical properties of the absorber. Table 5.1 contains a summary of the symbols used in the Bethe-Bloch equation,

$$-\frac{dE}{dx} = 2\pi N_a r_e^2 m_e c^2 \rho \frac{Z}{A} \frac{z^2}{\beta^2} \left[\ln \left(\frac{2m_e c^2 \gamma^2 \beta^2 W_{max}}{I^2} \right) - 2\beta^2 - \delta - 2 \frac{C}{Z} \right], \quad (5.1)$$

with

$$W_{max} = \frac{2m_e c^2 \beta^2 \gamma^2}{1 + 2\gamma \frac{m_e}{M} + \frac{m_e^2}{M^2}} \simeq 2m_e c^2 \beta^2 \gamma^2. \quad (5.2)$$

Table 5.1: Bethe-Bloch Equation Symbols

Symbol	Definition	Value or Units
N_a	Avogadro's number	$6.022 \times 10^{23} \text{ mol}^{-1}$
r_e	electron radius	$2.817 \times 10^{-13} \text{ cm}$
m_e	electron mass	511 keV
ρ	absorber density	$2.33 \text{ g/cm}^2 \text{ (Si)}$
Z	absorber atomic number	14 (Si)
A	absorber atomic weight	28.09 g/mol (Si)
z	incident particle charge	± 1
β	incident particle velocity divided by the speed of light	unitless
γ	$1/\sqrt{1 - \beta^2}$	unitless
W_{max}	maximum energy transfer of a single collision	see Eq. 5.2
M	incident particle mass	keV
I	absorber mean excitation potential	173 eV (Si)
δ	density correction	see Section 5.2.1
C	shell correction	see Section 5.2.2

5.2.1 Density Correction

The density correction, δ , results from the interaction of the the electric field of the incident particle with the atoms of the absorber. As the incident particle passes through the detector it polarizes the atoms along its path. The polarization of near atoms shields those which are further away from the full effect of the electric field. This in turn reduces the amount of energy lost by the incident particle in the medium. The correction factor is dependent upon the density of the absorber and the momentum of the incident particle. The form of the correction is shown in Eq. 5.3 and each of the terms is defined in Table 5.2,

$$\delta = 4.6052X + C_\delta + a(X_1 - X)^m. \quad (5.3)$$

Table 5.2: Density Correction Equation Symbols [53]

Symbol	Source	Value
X	dependent upon incident particle	$\log(\beta\gamma)$
C_δ	physical property of absorber	-4.44 (Si)
a	empirical fit to data	0.1492 (Si)
X_1	empirical fit to data	2.87 (Si)
m	empirical fit to data	3.25 (Si)

As the density of the absorber increases so does the induced polarization and hence the degree of shielding. This results in a net decrease in the amount of energy that is deposited by the incident particle relative to the Bethe-Bloch prediction. As the momentum of the particle increases the relative contribution from distant atoms also increases. However, due to the effect of shielding, the rate of increase is less than expected; therefore, the magnitude of the energy deposition must be corrected downward.

5.2.2 Shell Correction

The shell correction to the Bethe-Bloch equation is a result of the fact that the electrons in the absorber atoms are not stationary. The magnitude of the correction is determined using an empirical calculation that is dependent upon the mean excitation potential of the absorber and the velocity of the incident particle [53]. It is necessary to apply the correction only when the velocity of the incident particle is equivalent to or smaller than that of the absorber electrons. This is only true for very low momentum particles and is a negligible effect in this analysis.

5.2.3 Application in PHOBOS

In the PHOBOS spectrometer the energy loss of a particle is estimated using the measured energy loss from the hits that constitute a track. Each track consists of 11 or 12 individual hits. If the distribution of the energy loss could be described by a Gaussian function, then the energy loss of the particle can be described by the average energy loss of the hits. This is true for particles traversing thick absorbers. However, because the silicon sensors are thin, only $300\ \mu m$, the energy loss distribution is more accurately described by a Landau function. This is a result of the finite probability that a particle experiences a collision in which large amounts of energy are transferred. Consequently, the measured energy distribution is asymmetric and has a long, high-energy tail. The mean energy loss is accurately represented by removing the effect of the Landau tail by measuring the truncated mean of the energy loss of the hits [54]. In practice, this is done by averaging the energy deposited in the hits that have the lowest energy loss. The truncated mean energy loss of tracks that contain 12 hits is calculated using the 8 lowest energy hits and for tracks containing 11 hits it is calculated using the 7 lowest energy hits.

As a charged particle traverses a thick absorber all of the ionized electrons that are released remain within the absorber. However, in a thin absorber there exists a finite probability that some of the ionized electrons will escape and not be measured. Because the silicon sensors that compose the PHOBOS spectrometer are very thin, they are subject to this effect. To accurately represent the experimentally observed energy loss, the Bethe-Bloch equation must be modified. A new term W_{upper} is

introduced into the equation and is equal to the minimum of W_{cut} and W_{max} . The term W_{cut} is a threshold cut that allows the correction to be neglected if the energy deposition is above a minimum value. Incorporating this into Eq. 5.3 gives,

$$-\frac{dE}{dx} = 2\pi N_a r_e^2 m_e c^2 \rho \frac{Z}{A} \frac{z^2}{\beta^2} \left[\ln \left(\frac{2m_e c^2 \gamma^2 \beta^2 W_{upper}}{I^2} \right) - \left(1 + \frac{W_{upper}}{W_{max}} \right) \beta^2 - \delta - 2\frac{C}{Z} \right]. \quad (5.4)$$

To determine a theoretical estimate of the energy loss experienced by charged particles traversing the PHOBOS spectrometer, Eq. 5.4 can be plotted as a function of incident particle momentum. This is done for protons, kaons, pions and electrons in Fig. 5.1. A comparison of the theoretical curves and the data can be made by drawing the curves on top of the energy deposition versus momentum distribution observed in the data. The results of this comparison for the d+Au data set can be seen in Fig. 5.2. The Bethe-Bloch curves provide an accurate representation of the data. The results of the same comparison for the p+p data set show no distinguishable differences.

5.3 Particle Identification Cuts

In order to identify a particle as a pion, kaon or proton, the energy loss and momentum of the particle must fall near one of the theoretical Bethe-Bloch curves. Cuts are applied around each of the particle bands in the dE/dx versus p distribution, as shown in Fig. 5.3. The widths of the bands are determined such that they allow for

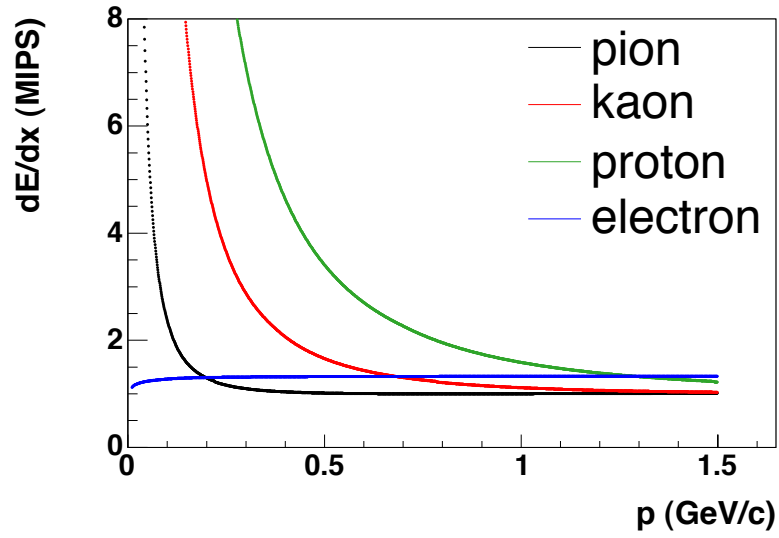


Figure 5.1: Theoretical Bethe-Bloch prediction of the distribution of energy deposition, dE/dx , as calculated from Eq. 5.4 versus particle momentum, p .

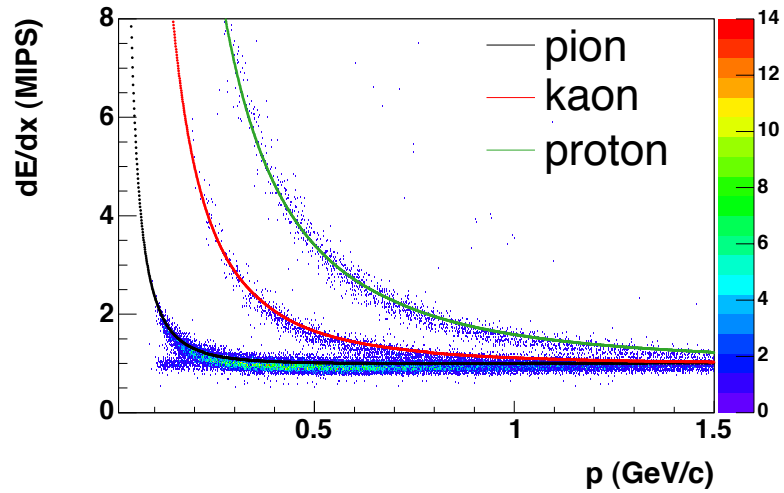


Figure 5.2: The average truncated energy loss expressed in MIPS versus reconstructed particle momentum for the d+Au data. The curves are the theoretical Bethe-Bloch prediction of the distribution for pions, kaons and protons calculated using Eq. 5.4 and shown in Fig. 5.1.

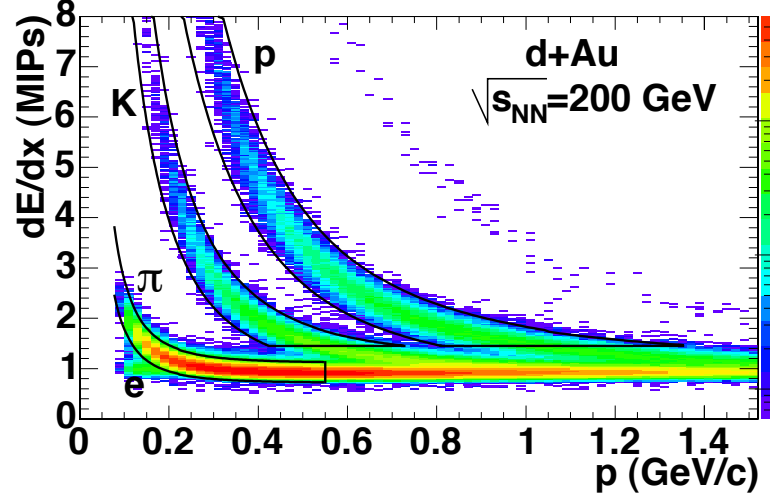


Figure 5.3: Distribution of the average truncated energy loss as a function of reconstructed particle momentum for the d+Au data set. The solid lines indicate the cut positions used for particle identification.

a 3 sigma deviation from the theoretical curve. An upper momentum cut is applied to the pion band at $p = 0.55$ GeV/c. This is the point where the pion and kaon 3 sigma bands intersect. The cut is necessary to minimize the number of kaons that are misidentified as pions. A lower dE/dx cut is applied to the kaon and proton bands at $dE/dx = 1.45$ MIPS. For the kaons this cut lies above the 4 sigma band of the pions and minimizes the number of pions that are misidentified as kaons. In addition, the dE/dx minimum cut lies near where the kaon and proton 3 sigma bands intersect. It is necessary to apply the minimum dE/dx cut to the proton band as well because above a momentum of 1.4 GeV/c it is not possible to distinguish between the different particle types. These particle identification cuts are used in the analysis of both the d+Au and p+p data sets.

5.4 Acceptance

Once the identity of the particles that leave tracks in the spectrometer is established, the acceptance of the sub-detector for each particle species can be determined. The acceptance for a given species is dependent upon the charge of the particle q and the polarity of the applied magnetic field B . The product of these two quantities determines the direction the track of the particle bends in the magnetic field. Particles of a given charge sign in a given magnetic field polarity bend in the same direction and have the same acceptance, as do oppositely charged particles in the opposite field configuration. Figure 5.4 shows the acceptance of the spectrometer in transverse momentum p_T and rapidity y space for pions, kaons and protons of both bending directions of the d+Au data set. The contours are drawn at the position where the acceptance falls to 10% of its maximal value. It should be noted that particles whose $q \times B$ product is positive bend towards the beam pipe while particles whose $q \times B$ product is negative bend away from the beam pipe.

5.5 Electron Contamination

The particle identification cuts are used to distinguish pions, kaons and protons from one another; however, the PHOBOS spectrometer is not optimized to resolve electrons. In Fig. 5.3 a small number of low momentum electrons can be identified at momenta less than 0.2 GeV/c, but they quickly become indistinguishable from pions as the momentum increases. For this reason, it is necessary to study the electron contamination in the pion band.

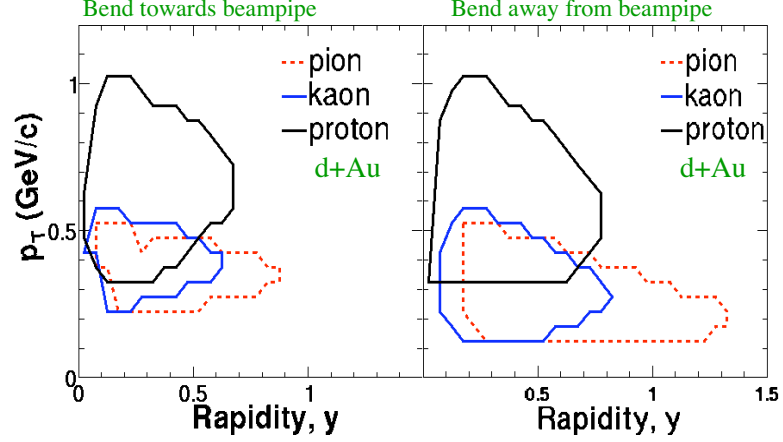


Figure 5.4: Spectrometer acceptance as a function of transverse momentum and rapidity, for each particle species in the two bending directions for the d+Au data set. The contours represent where the acceptance has fallen to 10% of the maximal value.

A closer examination of the region where the pion and electron bands intersect in the d+Au data set is shown in Fig. 5.5. If a cut is applied at $dE/dx = 1.1$ MIPS, the pion and electron bands remain separated up to a momentum of $p = 0.18$ GeV/c. The same distribution is shown for HIJING Monte-Carlo events in Fig. 5.6. For the purposes of this study all particles with an energy deposition less than 1.1 MIPS are considered to be electrons and all particles that fall within the range of $1.1 < dE/dx < 2.4$ MIPS are considered to be pions. Table 5.3 shows the resulting number of pions and electrons found in 0.02 GeV/c wide momentum bins in the region where pions and electrons can both be identified. A comparison of the ratio of electrons to pions found in the data and Monte-Carlo shows that the HIJING Monte-Carlo simulation accurately represents the relative fraction of each particle species found in the data. This allows the Monte-Carlo events, where the identity of each track is known, to be used to determine the electron contamination

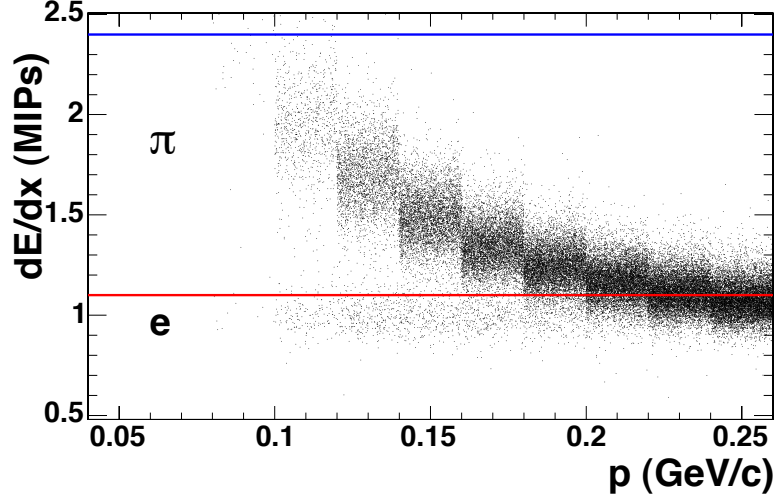


Figure 5.5: Distribution of the average truncated energy loss as a function of reconstructed particle momentum for the region in which pions and electrons can be resolved for the d+Au data set. The lower cut at $dE/dx = 1.1$ MIPS and the upper cut at $dE/dx = 2.4$ MIPS are indicated by lines.

Table 5.3: d+Au Data and Monte-Carlo Electron Contamination Comparison

Momentum (GeV/c)	Data $e^+ + e^-$	Data $\pi^+ + \pi^-$	Data e/π	MC $e^+ + e^-$	MC $\pi^+ + \pi^-$	MC e/π
0.10 - 0.12	430	2589	17%	20	104	19%
0.12 - 0.14	917	8971	10%	43	392	11%
0.14 - 0.16	997	14813	6.7%	46	650	7.1%
0.16 - 0.18	1246	19124	6.5 %	61	891	6.8%

in the identified pion band.

A upper estimate of the electron contamination in the pion band can be determined by measuring the relative fraction of electrons and pions that produce a track in the spectrometer over the momentum range for which pions are identified, $p < 0.55$ GeV/c. The results of this study using HIJING Monte-Carlo events are shown in Table 5.4. The contamination due to both positrons, e^+ , and electrons, e^- , is approximately 3%.

To account for the electron contamination in the pion band a correction factor

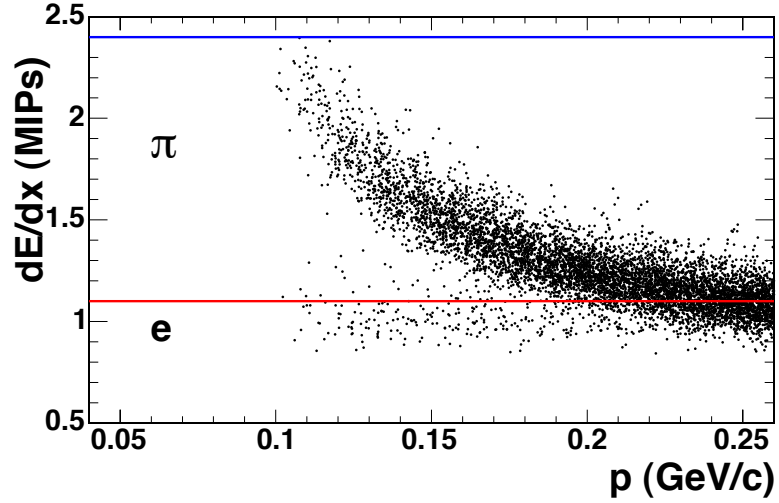


Figure 5.6: Distribution of the average truncated energy loss as a function of reconstructed particle momentum for the region in which pions and electrons can be resolved in d+Au HIJING Monte-Carlo events. The lower cut at $dE/dx = 1.1$ MIPS and the upper cut at $dE/dx = 2.4$ MIPS are indicated by lines.

Table 5.4: Relative Fraction of Electrons and Pions Found in the d+Au HIJING Monte-Carlo Simulation for $p < 0.55$ GeV/c

Charge	# Electrons	# Pions	e/π
+	706	24582	2.9%
-	822	26308	3.1%

to be applied to the data must be determined. Using the HIJING Monte-Carlo events it is found that the contaminant electrons are predominately secondary particles. They are produced via pair production from the decay of neutral pions, π^0 , and γ rays. Pair production results in equal numbers of electrons and positrons; therefore, the correction is symmetric for e^+ and e^- . Equations 5.5 through 5.9 show the details of how the correction factor is determined:

$$\frac{R_T}{R_M} = \frac{\frac{\pi_{prim}^-}{\pi_{prim}^+}}{\frac{\pi_{prim}^- + e_{symm}^-}{\pi_{prim}^+ + e_{symm}^+}}, \quad (5.5)$$

$$\frac{R_T}{R_M} = \frac{1}{1 + \frac{e_{symm}^-}{\pi_{prim}^-} \frac{\pi_{prim}^+}{1 + \frac{e_{symm}^+}{\pi_{prim}^+}}}, \quad (5.6)$$

$$\frac{R_T}{R_M} = \frac{1}{1 + \frac{e_{symm}^-}{\pi_{prim}^-} \frac{\pi_{prim}^+}{1 + R_T \frac{e_{symm}^+}{\pi_{prim}^+}}}, \quad (5.7)$$

$$\frac{R_T}{R_M} = \frac{1}{\frac{1+\alpha}{1+R_T\alpha}}, \quad (5.8)$$

$$R_T = \frac{R_M}{1 + \alpha(1 - R_M)}. \quad (5.9)$$

The definitions of the variables used in these equations can be found in Table 5.5.

Equation 5.9 shows that the true pion ratio corrected for electron contamination is dependent upon the measured pion ratio. Chapter 6 provides a description

Table 5.5: Definitions for the Derivation of the Electron Contamination Correction Factor, Equations 5.5 - 5.9

Symbol	Definition
R_T	true $\pi_{prim}^-/\pi_{prim}^+$ ratio
R_M	measured π^-/π^+ ratio
e_{symm}^-	measured electrons produced via pair production equal to e_{symm}^+
e_{symm}^+	measured positrons produced via pair production equal to e_{symm}^-
α	ratio of like charged electrons and pions equal to 3% from Table 5.4

Table 5.6: Estimated Correction Factors for the Measured π^-/π^+ Ratio

Trigger	Centrality	R_M	Correction
dAVertex	60-100%	0.996	0.9998
dAVertex	30-60%	1.005	1.0002
dAVertex	10-30%	1.008	1.0002
dAVertex	0-10%	1.016	1.0005
dAPeriph	60-100%	0.997	0.9999
dAPeriph	30-60%	1.014	1.0004
ppVertex	MinBias	0.9997	0.99999

of how the raw measured particle ratios are determined. The magnitude of the correction factors for each centrality bin of the d+Au data set and for the p+p data set are shown in Table 5.6. Because the correction is small, it will be applied as a systematic scale error to the pion ratio instead of as a correction factor.

The magnitude of the systematic scale error attributed to the measurement of the pion ratio due to electron contamination is determined based upon the extreme limits of the correction factor. The lower limit of the correction R_M^{lower} is determined by inserting the difference between the measured ratio and all of the statistical and

Table 5.7: Estimated Electron Contamination Correction Factors for the Measured π^-/π^+ Ratio

Trigger	Centrality	R_M^{lower}	Lower Correction	R_M^{upper}	Upper Correction
dAVertex	60-100%	0.973	0.9990	1.019	1.0006
dAVertex	30-60%	0.986	0.9996	1.024	1.0007
dAVertex	10-30%	0.989	0.9997	1.027	1.0008
dAVertex	0-10%	0.997	0.9999	1.035	1.0011
dAPeriph	60-100%	0.977	0.9993	1.017	1.0005
dAPeriph	30-60%	0.995	0.9999	1.033	1.0010
ppVertex	MinBias	0.978	0.9993	1.022	1.0007

systematic errors added in quadrature into Eq. 5.9 in place of R_M ,

$$R_M^{lower} = R_M - \sqrt{\sigma_{stat}^2 + \sigma_{sys}^2}. \quad (5.10)$$

The upper limit of the correction R_M^{upper} is determined using the sum of the measured ratio and all of the statistical and systematic errors added in quadrature,

$$R_M^{upper} = R_M + \sqrt{\sigma_{stat}^2 + \sigma_{sys}^2}. \quad (5.11)$$

Table 5.7 contains the results of these calculations. An explanation of how the statistical and systematic errors are determined can be found in Chapter 8. The maximum range of estimated correction factors is 0.002; therefore, a systematic scale error of ± 0.001 is assigned. Because identical particle identification bands are used in the analysis of the d+Au and p+p data sets, the same systematic scale error is assigned to both measurements of the π^-/π^+ ratio.

Chapter 6

Raw Particle Ratios

The raw particle ratios are calculated from the event normalized yields of each particle species. For each data set the selected events (Sec. 3.2) are divided according to centrality, beam orbit region and magnet polarity. The track selection cuts are applied (Sec. 6.1) and the particle identification bands (Sec. 5.3) are used to determine the particle species that generated each track. Finally, the yield of each particle species is normalized by the number of events and averaged over bending direction to correct for the acceptance of the spectrometer. The details of the track selection, event normalization and raw ratios calculation are described in this chapter.

Table 6.1: Track Selection Criteria for All Data Sets

Quantity	Cut Value	Description
Track Fit Probability	$prob > 0.04$	minimizes mismatched tracks
dca to Beam Orbit	$dca < 0.35$ cm	minimizes secondaries
TrkVtxVZ-OctDeVtxVZ	$ \text{Difference} < 6$ cm	3σ cut on OctDeVtxVZ resolution
dE/dx Maximum	$dE/dx < 16$ MIPS	removes wild dE/dx fluctuations
p_T Minimum	$p_T^\pi > 0.1$ GeV $p_T^K > 0.1$ GeV $p_T^p > 0.3$ GeV	minimizes secondaries

6.1 Track Selection

A series of cuts are applied to the tracks found in the spectrometer in order to minimize the number of secondary particles and mismatched tracks allowed in the analysis. This reduces the magnitude of the corrections that must be applied to the ratios and reduces the systematic error in the measurements. The details of the track selection cuts are listed in Table 6.1.

The fit probability of a track is determined in the curved tracking algorithm (Sec. 4.5.4). It is representative of the likelihood that all of the hits associated with the reconstructed track were actually generated by the same particle as it passed through the spectrometer. The distribution of the fit probability for the tracks found in beam orbit region 0 of the dAVertex data set is shown in Fig. 6.1. The line lies at the position of the track fit probability cut, $prob > 0.04$. This cut eliminates many of the tracks from the analysis that were improperly reconstructed.

The track selection cut applied to the distance of closest approach of the track to the mean position of the beam orbit, dca, is designed to reduce the number of

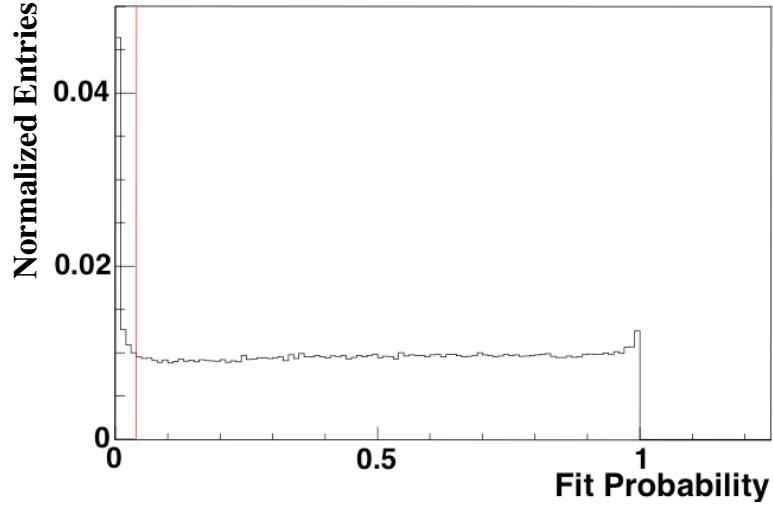


Figure 6.1: The fit probability of tracks in beam orbit region 0 of the dAVertex data set. The line lies at the cut position, $prob > 0.04$.

secondary particles accepted into the data sample. A study of HIJING Monte-Carlo events shows that above a dca of 0.35 cm the distribution is dominated by secondary particles. Figure 6.2 shows the distribution of the dca of primaries and secondaries; the line lies at the cut position. A more restrictive cut is not used because the width of the beam orbit is finite and the pointing resolution of the vertexing method used to determine the average position of the beam orbit is only known to within ± 0.1 cm. Because the dca distribution of all reconstructed particles in the data closely matches the Monte-Carlo distribution of all particles, as shown in Fig. 6.3, this cut can be used in the data analysis to reduce the contamination by secondaries by approximately a factor of 3.

A minimum p_T cut is applied to identified pions, kaons and protons to reduce the number of secondary particles incorporated into the analysis. A study of HIJING Monte-Carlo events shows that the number of accepted secondary particles increases

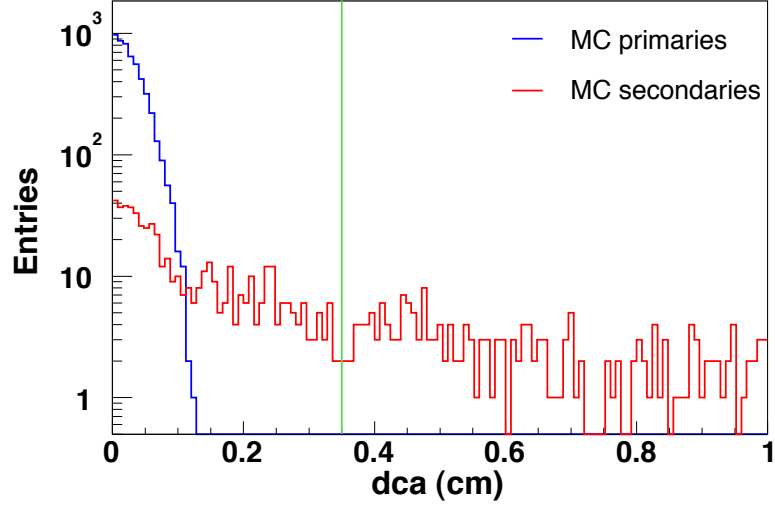


Figure 6.2: The distribution of the distance of closest approach of true HIJING Monte-Carlo tracks to the beam orbit. The blue distribution is for primaries and the red distribution is for secondaries. The green line lies at the position of the track selection cut, $dca < 0.35$ cm.

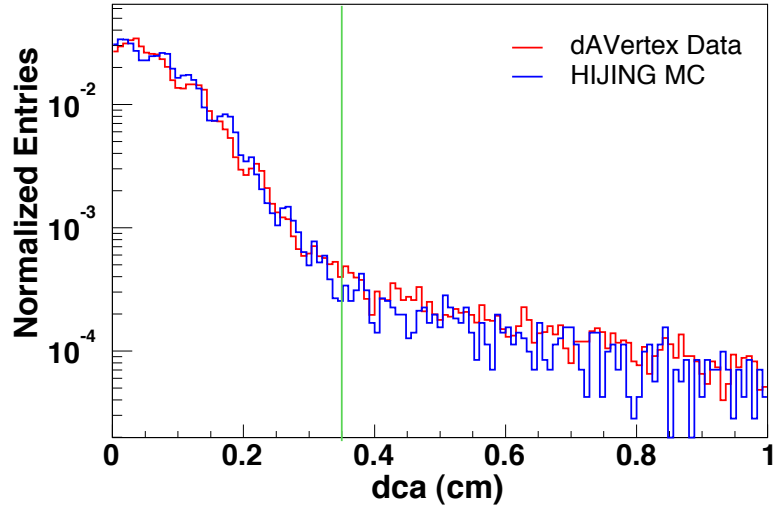


Figure 6.3: The distribution of the distance of closest approach of tracks to the beam orbit. The blue distribution is for true HIJING Monte-Carlo tracks, the red distribution is for reconstructed tracks in a subset of the dAVertex data set, and the green line lies at the position of the track selection cut, $dca < 0.35$ cm.

steeply as the transverse momentum approaches zero. For this reason, pions and kaons with transverse momenta less than 0.1 GeV/c and protons with transverse momenta less than 0.3 GeV/c are excluded from the analysis. The cut positions were chosen to keep the secondary contamination less than 5% for protons and less than 1% for pions and kaons.

6.2 Particle Yields & Normalization

The raw yields of each particle species are determined using the event selection, track selection, centrality, and particle identification criteria. Table 6.2 documents the event and particle species counts found for each data set. The data are divided according to magnet polarity B because the acceptance of the spectrometer for each species is dependent upon bending direction, as described in Sec. 5.4.

6.2.1 Event Normalization and Weighting

It is necessary to normalize the raw particle yields by the number of events before taking the ratios because different numbers of events were collected for each magnetic field polarity. The ratios of oppositely charged particles are calculated for each bending direction. This allows all acceptance dependent effects in the data to cancel and reduces the systematic uncertainty in the measurements. One effect that influences the yield of detected particles that does not cancel and hence must be accounted for is a consequence of different z-vertex distributions in the B^+ and B^- data sets. The difference in the distributions is shown in Fig. 6.4. The z-vertex

Table 6.2: Summary of Particle and Event Counts for Each Data Set

Trigger	Centrality	B	Events	π^-	π^+	K^-	K^+	\bar{p}	p
dAVertex	60-100%	-	1004052	2787	13879	163	537	310	556
		+	1120480	15320	3087	524	157	543	421
dAVertex	30-60%	-	2863440	14963	74941	824	2732	1604	3494
		+	3078602	81368	16164	2930	1011	2998	2282
dAVertex	10-30%	-	2444774	19663	95755	1113	3660	2198	4558
		+	2612126	103027	20641	3780	1237	3824	2903
dAVertex	0-10%	-	1291300	13628	64357	803	2497	1549	3077
		+	1378206	69664	14303	2675	864	2649	1958
dAPeriph	60-100%	-	3021106	8255	40530	455	1416	866	1841
		+	3222936	42931	8797	1509	461	1564	1085
dAPeriph	30-60%	-	3053872	13666	65799	737	2353	1461	3182
		+	3311696	71542	14435	2449	821	2707	2009
ppVertex	MinBias	-	2537906	5233	24478	287	899	506	1141
		+	1686214	16235	3500	551	190	585	396

distribution for B^+ events is shown in blue and the B^- distribution is shown in red, for a subset of the ppVertex data set. The ratio of the distributions for the two polarities is shown in Fig. 6.5 and can be fit with a linear function.

If the track weighted average z-vertex position for each particle species is the same for each bending direction, then the effect of the distribution on the acceptance will cancel when the average ratio over both bending directions is calculated. The track weighted average z-vertex position found in the dAVertex data set for each particle species is given in Table 6.3. It can be seen that the average position is not the same for the two bending directions. A correction must be applied to account for this because the magnitude of the observed difference is sufficient to shift the particle ratios by approximately 0.5%.

A correction factor is applied to the raw particle yields to weight the particle

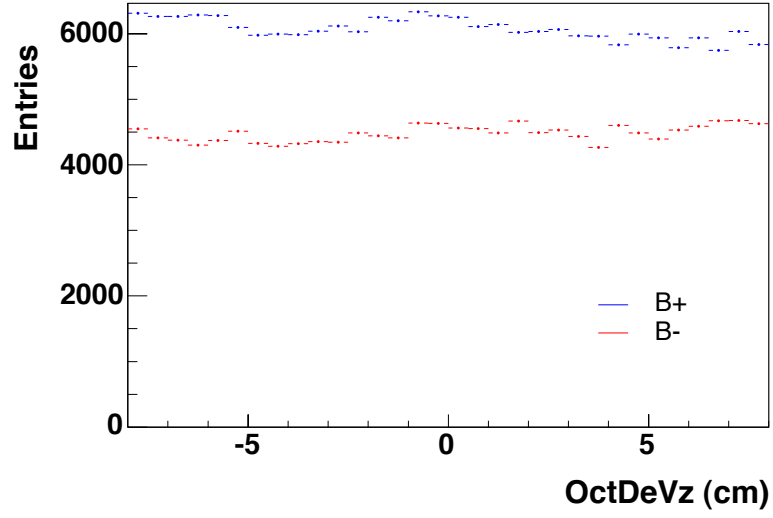


Figure 6.4: The z-vertex distribution observed in beam orbit region 0 of the ppVertex data set. The distribution for B^+ events is shown in blue and the B^- distribution is shown in red.

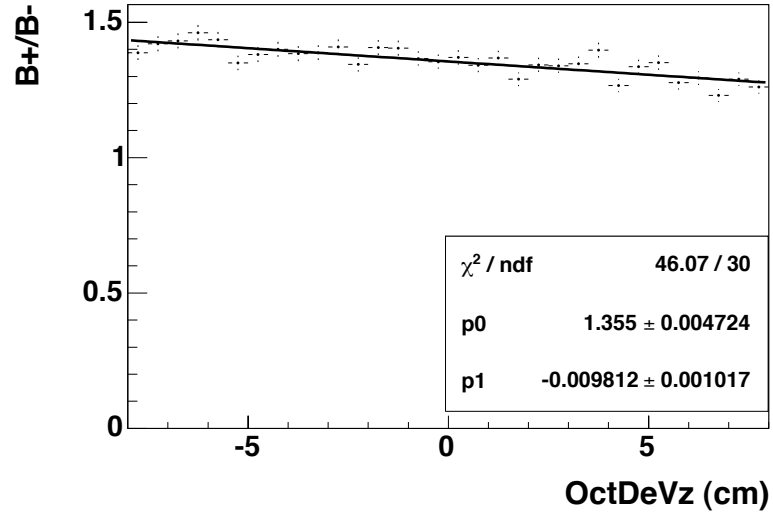


Figure 6.5: The ratio of the z-vertex distributions for B^+ and B^- events in beam orbit region 0 of the ppVertex data set. The parameters of the linear fit to the ratio are shown.

Table 6.3: Summary of Track Weighted Average Z-Vertex Position for Pions, Kaons and Protons in the dAVertex Data Set

Species	Bend (+) $\langle z \rangle$ (cm)	Bend (-) $\langle z \rangle$ (cm)	Difference
pion	0.82	1.55	-0.73
kaon	0.76	2.48	-1.72
proton	0.09	2.00	-1.91

counts by the normalized slope of the ratio of the number of events as a function of the z-vertex for opposite magnetic field polarities in each beam orbit region. The weighting functions are given by

$$\bar{p}(z)_{corr} = \bar{p}(z)_{meas} \left(1 - \frac{m}{2}z\right), \quad (6.1)$$

and

$$p(z)_{corr} = p(z)_{meas} \left(1 + \frac{m}{2}z\right). \quad (6.2)$$

The normalized slope values found for each beam orbit region of the dAVertex, dAPeriph and ppVertex data sets are listed in Table 6.4. Figure 6.5 illustrates how these numbers were obtained, with normalized slope = (p1/p0). As a result of this correction, non-integer numbers of each particle species are obtained.

6.3 Raw Ratios Calculation

The raw π^-/π^+ , K^-/K^+ and \bar{p}/p ratios for each data set are calculated using the z-vertex weighted particle counts. The data are further divided according to beam orbit region and spectrometer arm to determine if systematic effects due to

Table 6.4: Normalized Slope of the B^+/B^- Ratio of the Z-Vertex Distributions for All Data Sets

Trigger	BO Region	Normalized Slope
dAVertex	0	0.00513
dAVertex	1	0.000794
dAVertex	2	0.00266
dAVertex	3	-0.00671
dAPeriph	0	-0.00620
dAPeriph	1	0.00526
ppVertex	0	-0.00724
ppVertex	1	-0.00356

these variables are present in the data. The z-vertex weighted raw particle and event counts are given in Appendix B. The raw particle ratios for each species are calculated for each spectrometer arm and beam orbit region,

$$\left(\frac{\bar{p}}{p}\right)_{BO,arm} = \frac{1}{2} \left[\left(\frac{NTrack_{B^-}^{\bar{p}}/NEvent_{B^-}}{NTrack_{B^+}^p/NEvent_{B^+}} \right)_{BO,arm} + \left(\frac{NTrack_{B^+}^{\bar{p}}/NEvent_{B^+}}{NTrack_{B^-}^p/NEvent_{B^-}} \right)_{BO,arm} \right]. \quad (6.3)$$

The final raw ratio for each species is determined by the weighted average of all of the independently calculated spectrometer arm and beam orbit region ratios. The results are given in Table 6.5. It is found that the beam orbit regions and spectrometer arm divisions do not systematically influence the measurements.

6.4 Cross Checks

The method used to calculate the raw particle ratios assumes that the acceptance, tracking efficiency, and kinematic distributions for a given bending direction are the same for antiparticle and particles of each centrality. This eliminates the need to

Table 6.5: Raw Particle Ratios

Trigger	Centrality	$\langle \pi^- / \pi^+ \rangle$	$\langle K^- / K^+ \rangle$	$\langle \bar{p} / p \rangle$
dAVertex	60-100%	0.995	0.97	0.80
dAVertex	30-60%	1.004	0.95	0.77
dAVertex	10-30%	1.008	0.97	0.80
dAVertex	0-10%	1.016	0.97	0.82
dAPeriph	60-100%	0.996	1.02	0.82
dAPeriph	30-60%	1.014	0.97	0.79
ppVertex	MinBias	1.000	0.93	0.81

apply correction factors for each of these variables because their effects cancel when the ratio is taken. These assumptions can be confirmed by studying the kinematic distributions of the accepted particles and the stability of the magnetic field over the course of the data collection period.

6.4.1 Kinematic Distributions

The stability of each data set as a function of rapidity (y), transverse momentum (p_T) and transverse momentum squared (p_T^2) provides an estimate of the uniformity of the acceptance. This can be investigated by calculating the difference in the average values of each of these variables for antiparticles and particles. Ideally, the difference should be zero. The data are divided according to centrality bin, bending direction, spectrometer arm and beam orbit region, as in the ratios calculation. Figure 6.6 shows an example of the difference in the average transverse momenta of π^- and π^+ particles that bend away from the beam pipe as a function of centrality for the dAVertex data set. Table 6.6 lists the percentage difference between the average kinematic distributions for antiparticles and particles for each bending direction

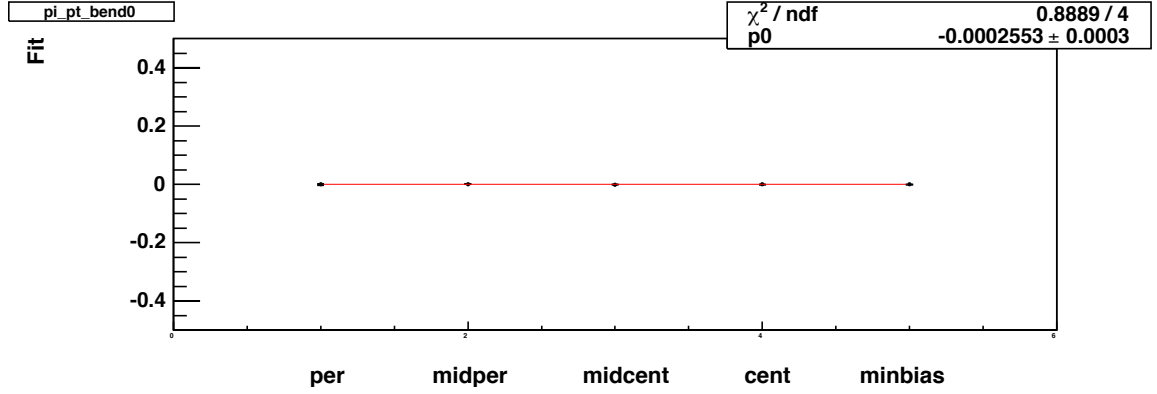


Figure 6.6: The difference in the average transverse momenta of π^- and π^+ particles that bend away from the beam pipe as a function of centrality for the dAVertex data set.

Table 6.6: Percentage Difference Between Average Kinematic Variables for Antiparticles and Particles of Both Bending Directions

Species	Bend Dir.	d+Au			p+p		
		$\langle p_T \rangle$	$\langle p_T^2 \rangle$	$\langle y \rangle$	$\langle p_T \rangle$	$\langle p_T^2 \rangle$	$\langle y \rangle$
pion	Neg.	0.18	0.34	0.50	0.54	1.1	0.53
pion	Pos.	0.22	0.42	0.15	0.41	0.69	1.0
kaon	Neg.	0.64	1.2	0.82	2.4	4.7	2.7
kaon	Pos.	1.1	2.1	0.71	4.1	5.1	4.8
proton	Neg.	0.44	0.90	0.61	1.5	3.4	2.2
proton	Pos.	0.37	0.75	2.1	2.1	3.4	2.9

of the d+Au and p+p data sets. In both the d+Au and p+p data the average kinematic distributions are all found to agree within $\pm 5\%$.

6.4.2 Magnetic Field Stability

Magnetic field instabilities can influence the particle acceptance and tracking efficiency; thus, it is important to ensure that the data used in the analysis were collected in a constant field environment. The stability of the magnetic field can be monitored during the course of the run using a Hall probe. Figure 6.7 shows the

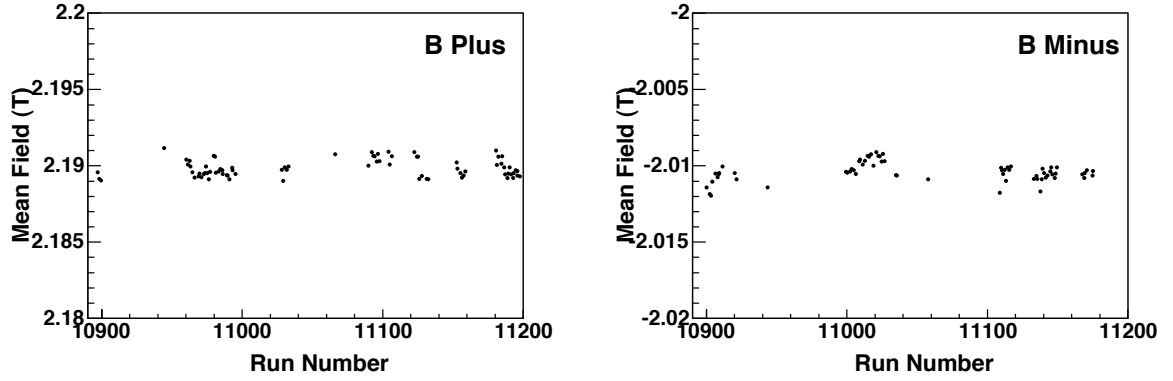


Figure 6.7: Magnetic field strength as a function of time for the dAVertex data set.

stability of the magnetic field over the course of the dAVertex data collection period for data collected in the positive and negative magnetic field configurations. The maximum deviation observed is $\pm 0.1\%$. For the dAPeriph and ppVertex data sets the maximum variation is $\pm 0.2\%$.

Chapter 7

Corrected Particle Ratios

To represent the relative yields of primary antiparticles and particles produced in the collision, the raw particle ratios calculated in Chapter 6 must be corrected for the inclusion of decay products and the results of interactions of the collision products with the material of the detector. As the collision products pass through the material of the detector some are absorbed in the beam pipe and spectrometer planes. Absorption results in a preferential loss of antiparticles and a subsequent decrease of the measured ratios. Furthermore, a correction must be applied to account for secondary particles produced as the collision products pass through the detector material, generating predominately particles. If left uncorrected for, each of these processes affects the measured antiparticle to particle ratios and could lead to an inaccurate conclusion about the properties of the collision system. It is critical

that correction factors be applied to the data. This chapter describes how the feed-down, secondary and absorption corrections are determined and applied to the measured raw ratios.

7.1 Feed-down Correction

Feed-down particles are produced when unstable primary collision products decay. If the half life of the collision product is small then it is possible to measure the decay products in the PHOBOS spectrometer. In principal, it is not possible to distinguish between primary particles and decay products of the same species. However, in practice it is possible to minimize the yield of decay products included in the antiparticle and particle measurements. Two scenarios exist in which feed-down particles pass through the spectrometer. First, if the decay occurs rapidly after the collision, the decay products may produce complete tracks in the spectrometer. Second, if the decay occurs after the primary particle has entered the spectrometer, the track reconstruction will be incomplete. The PHOBOS spectrometer is situated only 10 cm from the nominal interaction point; therefore, if it is assumed that the particles are moving at the speed of light, a decay product must be produced within 33 ns of the collision in order to be measured in the first plane of the spectrometer. A cut is applied to each reconstructed track that requires that the z-vertex position of the track lie within 0.35 cm of the beam orbit. Because decay products are not produced at the collision vertex their track vertices rarely lie within these cut parameters. In spite of these preventative measures some decay products are

included in the raw antiparticle and particle yields. The following sections examine the magnitude of this effect for protons, pions and kaons.

7.1.1 Proton Feed-down Correction Factor

Weak decays of hyperons, primarily Λ and $\bar{\Lambda}$ particles, generate daughter particles that can be detected. This decay mechanism predominantly influences the \bar{p}/p ratio as a result of the decay paths shown in Eq. 7.1 and Eq. 7.2,

$$\Lambda \rightarrow p + \pi^-, \quad (7.1)$$

$$\bar{\Lambda} \rightarrow \bar{p} + \pi^+. \quad (7.2)$$

The influence of feed-down on the pion ratio is much smaller because of the large relative yield of primary pions in the collision compared to primary protons and will be discussed in Sec. 7.1.5.

The true ratio of primary antiprotons to protons within the acceptance of the spectrometer is expressed as,

$$\frac{\bar{p}_{prim}^{acc}}{p_{prim}^{acc}} = C_{fd}^p * \left(\frac{\bar{p}_{meas}^{acc}}{p_{meas}^{acc}} \right), \quad (7.3)$$

where C_{fd}^p represents the feed-down correction factor for protons, the superscript *acc* indicates the particles are generated within the acceptance of the spectrometer, and the subscripts *meas* and *prim* refer to measured and primary particles, respectively.

If the measured number of particles is equal to the sum of primary particles and

feed-down products (fd) then,

$$\frac{\bar{p}_{prim}^{acc}}{p_{prim}^{acc}} = C_{fd}^p * \left(\frac{\bar{p}_{prim}^{acc} + \bar{p}_{fd}^{acc}}{p_{prim}^{acc} + p_{fd}^{acc}} \right). \quad (7.4)$$

Equation 7.4 can be rearranged to find the form of the correction factor,

$$C_{fd}^p = \frac{(\bar{p}_{prim}^{acc}/p_{prim}^{acc})}{(\bar{p}_{prim}^{acc} + \bar{p}_{fd}^{acc})/(p_{prim}^{acc} + p_{fd}^{acc})}, \quad (7.5)$$

$$C_{fd}^p = \frac{1 + (p_{fd}^{acc}/p_{prim}^{acc})}{1 + (\bar{p}_{fd}^{acc}/\bar{p}_{prim}^{acc})}. \quad (7.6)$$

The yield of feed-down protons produced as a result of Λ decay is equal to the product of the number of primary Λ particles produced in the collision and the branching ratio, br , for the decay path shown in Eq. 7.1. Similarly, an analogous relationship is true for $\bar{\Lambda}$'s and antiprotons. Applying this to Eq. 7.6 gives

$$C_{fd}^p = \frac{1 + \frac{\Lambda_{prim}^{prod} * br}{p_{prim}^{prod}} \frac{(p_{fd}^{acc}/p_{fd}^{prod})}{(p_{prim}^{acc}/p_{prim}^{prod})}}{1 + \frac{\bar{\Lambda}_{prim}^{prod} * br}{\bar{p}_{prim}^{prod}} \frac{(\bar{p}_{fd}^{acc}/\bar{p}_{fd}^{prod})}{(\bar{p}_{prim}^{acc}/\bar{p}_{prim}^{prod})}}. \quad (7.7)$$

If the acceptance factor for identifying a proton produced via decay as a primary particle, ϵ_{acc} , is defined as

$$\epsilon_{acc} = \frac{(p_{fd}^{acc}/p_{fd}^{prod})}{(p_{prim}^{acc}/p_{prim}^{prod})} = \frac{(\bar{p}_{fd}^{acc}/\bar{p}_{fd}^{prod})}{(\bar{p}_{prim}^{acc}/\bar{p}_{prim}^{prod})}, \quad (7.8)$$

then the correction factor, C_{fd}^p , can be rearranged as

$$C_{fd}^p = \frac{1 + \frac{\Lambda_{prim}^{prod}}{\bar{p}_{prim}^{prod}} * br\epsilon_{acc}}{1 + \frac{\Lambda_{prim}^{prod}}{\bar{p}_{prim}^{prod}} * br\epsilon_{acc}}, \quad (7.9)$$

$$C_{fd}^p = \frac{1 + br\epsilon_{acc} * \left(\frac{\bar{\Lambda}_{prim}^{prod}}{\bar{p}_{prim}^{prod}} \right) \left[\frac{(\bar{p}_{prim}^{prod}/p_{prim}^{prod})}{(\bar{\Lambda}_{prim}^{prod}/\Lambda_{prim}^{prod})} \right]}{1 + br\epsilon_{acc} * \left(\frac{\bar{\Lambda}_{prim}^{prod}}{\bar{p}_{prim}^{prod}} \right)}. \quad (7.10)$$

The magnitude of the correction function to be applied to the \bar{p}/p ratio can be determined by solving Equation 7.10. This equation contains three expressions whose values can be found using a combination of experimental data and theoretical model predictions. These quantities are investigated in the following sections.

7.1.1.1 Determination of $\frac{(\bar{p}_{prim}^{prod}/p_{prim}^{prod})}{(\bar{\Lambda}_{prim}^{prod}/\Lambda_{prim}^{prod})}$

The relative yields of primary \bar{p} 's to p 's and $\bar{\Lambda}$'s to Λ 's produced in 200 GeV d+Au and p+p collisions can be found using the principles of the Quark Coalescence model [55]. In this model the number of primary particles produced is assumed to be proportional to the product of the number of constituent quarks. The constant of proportionality is the same for antiparticles and particles of the same species and hence cancels in the ratio. Using the Quark Coalescence model the expression

$$\frac{\bar{\Lambda}}{\Lambda} = \frac{K^+}{K^-} * \frac{\bar{p}}{p} \quad (7.11)$$

can be written, where the symbol of each particle represents the number of that particle species present at hadronization. If each particle is expressed according to

its constituent quarks, Eq. 7.11 becomes

$$\frac{\bar{u}\bar{d}\bar{s}}{uds} = \frac{u\bar{s}}{\bar{u}s} * \frac{\bar{u}\bar{u}\bar{d}}{uud} \quad (7.12)$$

and it can be seen that the principles of the Quark Coalescence model are obeyed.

Using the relationship shown in Equation 7.11 an estimate of the magnitude of $\frac{(\bar{p}_{prim}^{prod}/p_{prim}^{prod})}{(\bar{\Lambda}_{prim}^{prod}/\Lambda_{prim}^{prod})}$ can be determined from the measured $\frac{K^-}{K^+}$ ratio, since the primary kaon yield is much larger than the Λ yield. In the d+Au collision system it is found that the kaon ratio is independent of centrality (Table 6.5); therefore, the weighted average is used, $\langle \frac{K^-}{K^+} \rangle = 0.97 \pm 0.03$. When calculating the average ratio the measured value for each centrality bin is weighted using the statistical and systematic errors added in quadrature. Chapter 8 provides a detailed explanation of how these errors are determined. In the p+p collision system the minimum bias kaon ratio is used, $\langle \frac{K^-}{K^+} \rangle = 0.93 \pm 0.03$. The quoted errors represent the systematic error in the measurement.

The systematic error attributed to the use of the kaon ratio to determine the relative yields of primary \bar{p} 's to p 's and $\bar{\Lambda}$'s to Λ 's is estimated using HIJING Monte-Carlo events. The upper bound to the $\frac{(\bar{p}_{prim}^{prod}/p_{prim}^{prod})}{(\bar{\Lambda}_{prim}^{prod}/\Lambda_{prim}^{prod})}$ ratio is taken to be the measured kaon ratio plus the systematic error, +0.03. The lower bound is the minimum of the measured kaon ratio minus the systematic error and the $\left(\frac{\bar{p}}{p}\right) / \left(\frac{\bar{\Lambda}}{\Lambda}\right)$ ratio as determined from HIJING Monte-Carlo events. The results of the HIJING Monte-Carlo study are given in Table 7.1.

In the 200 GeV p+p collision system the STAR Collaboration has reported

Table 7.1: Lower Bound to $\frac{(\bar{p}_{prim}^{prod}/p_{prim}^{prod})}{(\bar{\Lambda}_{prim}^{prod}/\Lambda_{prim}^{prod})}$ Estimate

Trigger	Centrality	MC $\left(\frac{\bar{p}}{p}\right) / \left(\frac{\bar{\Lambda}}{\Lambda}\right)$	$\langle K^-/K^+ \rangle_{meas} - 0.03$	lower bound
dAVertex	60-100%	0.94	0.94	0.94
dAVertex	30-60%	0.93	0.94	0.93
dAVertex	10-30%	0.91	0.94	0.91
dAVertex	0-10%	0.90	0.94	0.90
dAPeriph	60-100%	0.94	0.94	0.94
dAPeriph	30-60%	0.93	0.94	0.93
ppVertex	MinBias	0.97	0.90	0.90

preliminary measurements of both the primary $\frac{\bar{p}}{p}$ and $\frac{\bar{\Lambda}}{\Lambda}$ ratios. The preliminary ratios are reported by the STAR Collaboration to be equal to 0.82 ± 0.01 and 0.89 ± 0.03 , respectively [56]. The ratio of these values can be taken to find the experimental magnitude of the $\frac{(\bar{p}_{prim}^{prod}/p_{prim}^{prod})}{(\bar{\Lambda}_{prim}^{prod}/\Lambda_{prim}^{prod})}$ ratio, 0.92 ± 0.03 . The agreement between this value and the measured kaon ratio for 200 GeV p+p collisions supports the use of the Quark Coalescence model to estimate the value of $\frac{(\bar{p}_{prim}^{prod}/p_{prim}^{prod})}{(\bar{\Lambda}_{prim}^{prod}/\Lambda_{prim}^{prod})}$ in 200 GeV d+Au and p+p collisions.

7.1.1.2 Determination of $\frac{\bar{\Lambda}_{prim}^{prod}}{\bar{p}_{prim}^{prod}}$

The relative yields of primary $\bar{\Lambda}$'s and \bar{p} 's produced in 200 GeV d+Au and p+p collisions have not been experimentally measured. A comparison of the experimentally determined $\frac{\Lambda}{p}$ and $\frac{\bar{\Lambda}}{\bar{p}}$ ratios found in 130 GeV Au+Au collisions by the PHENIX Collaboration [57] with those found using HIJING Monte-Carlo events, listed in Table 7.2, reveals that it is difficult to make an accurate estimate of these ratios. The experimentally determined ratios reported by the Phenix collaboration are not corrected for feed-down from hyperons that are heavier than Λ and $\bar{\Lambda}$, but the p

Table 7.2: Experimental and HIJING Monte-Carlo Measurements of $\frac{dN}{dy}(\bar{\Lambda})$ and $\frac{dN}{dy}(\Lambda)$

Source	System	Centrality	$\frac{\frac{dN}{dy}(\Lambda)}{\frac{dN}{dy}(p)}$	$\frac{\frac{dN}{dy}(\bar{\Lambda})}{\frac{dN}{dy}(\bar{p})}$
Phenix [57]	130 GeV Au+Au	Central	0.90 ± 0.11	0.93 ± 0.15
Phenix [57]	130 GeV Au+Au	MinBias	0.89 ± 0.07	0.94 ± 0.10
HIJING	200 GeV Au+Au	Central	0.24	0.26
HIJING	200 GeV d+Au	MinBias	0.25	0.25
HIJING	200 GeV p+p	MinBias	0.25	0.25

and \bar{p} yields are corrected for feed-down from lambda decay. Due to the large differences in the experimental and simulated $\frac{\bar{\Lambda}}{\bar{p}}$ ratios, it is assumed that the ratio can vary from 0.2 to 1. An analysis of the effect of these two extreme values on the final correction factor reveals that, in spite of the large discrepancy, it has only a minimal affect on the final correction factor; therefore, the large uncertainty in the $\frac{\bar{\Lambda}}{\bar{p}}$ ratio does not translate into a large uncertainty in the final correction. The final value to be used in the calculation of the correction factor is $0.59 \pm 0.34(\text{syst.})$. This number is an average of the published result for 130 GeV Au+Au collisions [57] and the value obtained from studying 200 GeV d+Au and p+p HIJING Monte-Carlo events.

7.1.1.3 Determination of $br * \epsilon_{acc}$

The product of the branching ratio and acceptance factor can be expressed for protons as

$$br * \epsilon_{acc} = br * \frac{(p_{fd}^{acc}/p_{fd}^{prod})}{(p_{prim}^{acc}/p_{prim}^{prod})}. \quad (7.13)$$

Using the decay relationship between the number of primary produced Λ particles and the number of feed-down produced protons, $p_{fd}^{prod} = br * \Lambda_{prim}^{prod}$, the product of the branching ratio and acceptance factor can be rearranged to give

$$br * \epsilon_{acc} = \frac{(p_{fd}^{acc} / \Lambda_{prim}^{prod})}{(p_{prim}^{acc} / p_{prim}^{prod})}. \quad (7.14)$$

This expression shows that it is necessary to determine both $\frac{p_{fd}^{acc}}{\Lambda_{prim}^{prod}}$ and $\frac{p_{prim}^{acc}}{p_{prim}^{prod}}$ in order to find the magnitude of $br * \epsilon_{acc}$.

To evaluate Eq. 7.14, a Monte-Carlo simulation is used in which protons and Λ particles are propagated through the PHOBOS detector. This simulation is independent of collision system and depends only upon the input parameters of the particles being propagated through the detector. The input momentum distribution of the particles is flat in total momentum and angular cuts are applied to match the geometric acceptance of the spectrometer. A realistic beam spot size and track z-vertex distribution are also used. Finally, the simulated events are run through the standard tracking procedure. The results of this simulation are shown in Fig. 7.1. The distribution shown in black is the reconstruction efficiency of primary protons, $\left(\frac{p_{prim}^{acc}}{p_{prim}^{prod}}\right)$, and the red distribution is the reconstruction efficiency of feed-down protons generated from primary Λ particles, $\left(\frac{p_{fd}^{acc}}{\Lambda_{prim}^{prod}}\right)$. The ratio of the two distributions shown in Fig. 7.1 is used to solve Equation 7.14 as a function of transverse momentum and is shown in Fig. 7.2.

Due to the dependence of the particle reconstruction efficiency on the transverse momentum of the particle, a p_T dependent function of $br * \epsilon_{acc}$ is used to de-

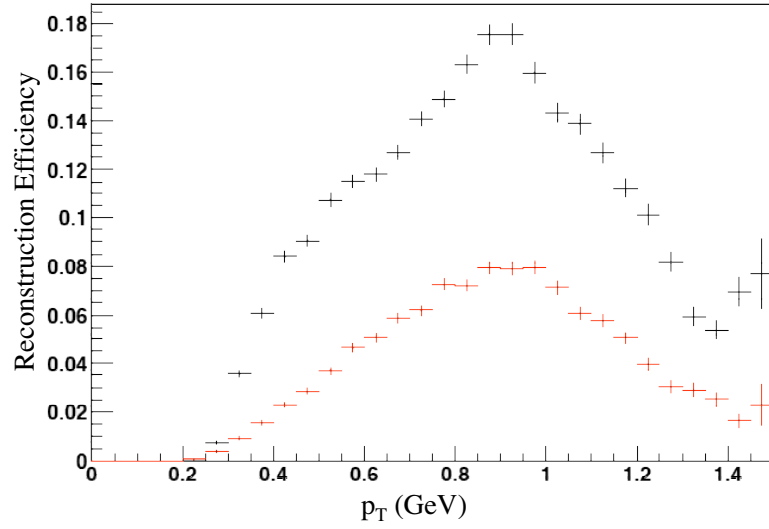


Figure 7.1: The distribution shown in black is the reconstruction efficiency of primary protons and the red distribution is the reconstruction efficiency of feed-down protons generated from primary Λ particles as a function of transverse momentum.

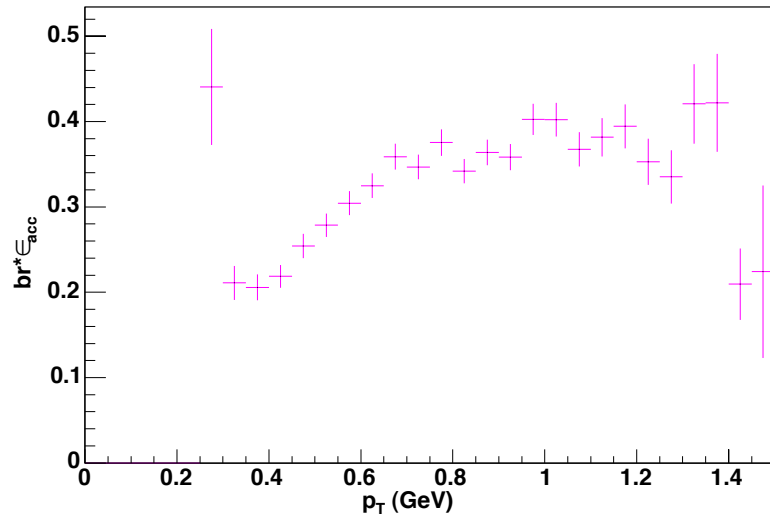


Figure 7.2: $br * \epsilon_{acc}$ as a function of transverse momentum.

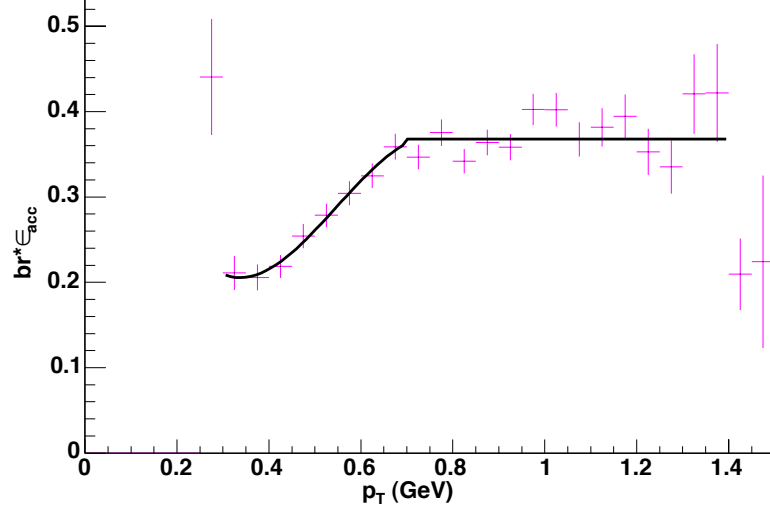


Figure 7.3: $br * \epsilon_{acc}$ as a function of transverse momentum fit with the functional form shown in Eq. 7.15.

termine the final feed-down correction. The functional form used to fit the $br * \epsilon_{acc}$ distribution is

$$br * \epsilon_{acc}(p_T) = \begin{cases} p_0 + p_1 p_T + p_2 p_T^2 + p_3 p_T^3 & \text{if } p_T < 0.7 \\ p_4 & \text{if } p_T > 0.7. \end{cases} \quad (7.15)$$

A polynomial fit is used for low momentum particles and a constant fit is used above $p_T = 0.7$ GeV/c to reduce the error introduced as a result of the statistical uncertainty of the measurement in the high momentum region. The fit function is shown plotted on top of the $br * \epsilon_{acc}$ distribution in Fig. 7.3.

7.1.1.4 Final Feed-down Correction Factor

The final feed-down correction factor to the \bar{p}/p ratio for each centrality bin is determined as a function of transverse momentum by weighting the correction function

Table 7.3: $\frac{\bar{p}}{p}$ Feed-down Correction Factors and Systematic Errors

Trigger Condition	Centrality	C_{fd}^p
dAVertex	60-100%	$0.995 \pm 0.001(\text{syst, scale}) \pm 0.006(\text{syst, pt-to-pt})$
dAVertex	30-60%	$0.995 \pm 0.001(\text{syst, scale}) \pm 0.006(\text{syst, pt-to-pt})$
dAVertex	10-30%	$0.995 \pm 0.001(\text{syst, scale}) \pm 0.01(\text{syst, pt-to-pt})$
dAVertex	0-10%	$0.995 \pm 0.001(\text{syst, scale}) \pm 0.01(\text{syst, pt-to-pt})$
dAPeriph	60-100%	$0.995 \pm 0.001(\text{syst, scale}) \pm 0.006(\text{syst, pt-to-pt})$
dAPeriph	30-60%	$0.995 \pm 0.001(\text{syst, scale}) \pm 0.006(\text{syst, pt-to-pt})$
ppVertex	MinBias	$0.995 \pm 0.01(\text{syst, total})$

by the p_T distribution of protons in that centrality bin. The feed-down correction factors for each centrality bin are given in Table 7.3. The scale systematic error is a result of the requirement that the track of an accepted particle point back to within 0.35 cm of the beam orbit. The point-to-point systematic error originates from the allowed range of values for the $\frac{\bar{\Lambda}_{prim}^{prod}}{\bar{p}_{prim}^{prod}}$ ratio and the determination of the $\frac{(\bar{p}_{prim}^{prod}/p_{prim}^{prod})}{(\bar{\Lambda}_{prim}^{prod}/\Lambda_{prim}^{prod})}$ ratio. In the p+p collision system no differentiation is made between point-to-point and scale systematic errors because only a minimum bias measurement is made.

7.1.2 Pion Feed-down Correction Factor

The sources of decay background that contribute to the measured π^-/π^+ ratio can be determined using d+Au HIJING Monte-Carlo events that are propagated through the PHOBOS detector. These events are subjected to the same kinematic cuts as is the data. Tables 7.4 and 7.5 list the particle species that generate pions upon decay and their relative contribution to the pion yield. The results obtained using p+p HIJING Monte-Carlo events are equivalent within errors.

Two categories of decay type exist, symmetric and asymmetric. Symmetric

Table 7.4: Sources of Decay Background for π^-

Species	Decay Channel	BR	MC Tracks	Decay Type
π^-	none	NA	43430	NA
K_{Short}^0	$\pi^+\pi^-$	68%	2733	Symmetric
η	$\pi^+\pi^-\pi^0$	23%	5	Symmetric
Λ	$p\pi^-$	64%	424	Asymmetric
Σ^-	$n\pi^-$	99%	243	Asymmetric
Ξ^-	$\Lambda\pi^-$	100%	72	Asymmetric
Σ^+	$\bar{n}\pi^-$	48%	133	Asymmetric
ϕ	$K_{\text{Long}}K_{\text{Short}} \rightarrow \pi^+\pi^-$	25%	137	Symmetric

Table 7.5: Sources of Decay Background for π^+

Species	Decay Channel	BR	MC Tracks	Decay Type
π^+	none	NA	41102	NA
K_{Short}^0	$\pi^+\pi^-$	68%	2513	Symmetric
η	$\pi^+\pi^-\pi^0$	23%	2	Symmetric
Σ^+	$n\pi^+$	48%	138	Asymmetric
Λ	$\bar{p}\pi^+$	64%	357	Asymmetric
Σ^-	$\bar{n}\pi^+$	100%	218	Asymmetric
Ξ^-	$\Lambda\pi^+$	100%	68	Asymmetric
ϕ	$K_{\text{Long}}K_{\text{Short}} \rightarrow \pi^+\pi^-$	25%	120	Symmetric

decay results in equal yields of positive and negative pions while asymmetric decay results in the production of only π^- or π^+ particles. An estimate of the yield of asymmetric pion production is provided by the $\frac{\bar{\Lambda}}{\Lambda}$ ratio. A preliminary measurement of this ratio has been reported by the Star collaboration to be 0.82 ± 0.01 in the p+p collision system [56]. The ratio of asymmetric to symmetric decay yield, f , found using the numbers reported in Tables 7.4 and 7.5 is approximately 1/3. The ratio of pions produced via symmetric decay to primary pions, α^π , is approximately 0.065.

The feed-down correction to the π^-/π^+ ratio can be expressed as

$$C_{fd}^\pi = \frac{\frac{\pi_{prim}^-}{\pi_{prim}^+}}{\frac{\pi_{prim}^- + \pi_{sym}^- + \pi_{asym}^-}{\pi_{prim}^+ + \pi_{sym}^+ + \pi_{asym}^+}}. \quad (7.16)$$

This equation can be rearranged to give

$$C_{fd}^\pi = \left(1 + \alpha^\pi [1 + f - R_M^\pi (1 + \frac{\bar{\Lambda}}{\Lambda} f)] \right)^{-1}, \quad (7.17)$$

where R_M^π is defined as the measured π^-/π^+ ratio. Using Eq. 7.17, the correction factor to the pion ratio for each data set and centrality bin can be calculated. The results of this calculation are given in Table 7.6. Because the correction is small, it will be applied as a systematic scale error to the pion ratio instead of as a correction factor.

The magnitude of the systematic scale error attributed to the measurement of the pion ratio due to feed-down is determined in the same manner as described for the electron contamination systematic error, Sec. 5.5. The maximum range

Table 7.6: Feed-down Correction Factors for the Measured $\frac{\pi^-}{\pi^+}$ Ratio

Trigger	Centrality	R_M^π	$C_{fd}^{\pi i}$
dAVertex	60-100%	0.996	0.996
dAVertex	30-60%	1.005	0.997
dAVertex	10-30%	1.008	0.997
dAVertex	0-10%	1.016	0.997
dAPeriph	60-100%	0.997	0.996
dAPeriph	30-60%	1.014	0.997
ppVertex	MinBias	1.000	0.996

Table 7.7: Sources of Decay Background for K^- and K^+

Species	Decay Channel	BR	MC Tracks	Decay Type
K^-	none	NA	2519	NA
K^+	none	NA	2913	NA
ϕ	K^+K^-	49.5%	250	Symmetric

of allowed correction factors is ± 0.005 ; therefore, a systematic scale error of this magnitude is assigned.

7.1.3 Kaon Feed-down Correction Factor

The feed-down correction factor to the K^-/K^+ is found in an analogous manner to that of the π^-/π^+ ratio with one key difference. Because the only source of decay kaons is from symmetric decay channels, the contribution from asymmetric decay need not be considered. Table 7.7 contains the results of the d+Au HIJING Monte-Carlo study of the kaon decay background. The results obtained using p+p HIJING Monte-Carlo events are equivalent within errors.

Because only symmetric decay contributes to the kaon feed-down correction,

Table 7.8: Feed-down Correction Factors for the Measured $\frac{K^-}{K^+}$ Ratio

Trigger	Centrality	R_M^K	C_{fd}^K
dAVertex	60-100%	0.97	0.997
dAVertex	30-60%	0.95	0.995
dAVertex	10-30%	0.97	0.997
dAVertex	0-10%	0.97	0.997
dAPeriph	60-100%	1.02	1.002
dAPeriph	30-60%	0.97	0.997
ppVertex	MinBias	0.93	0.993

the equation for the correction factor, C_{fd}^K , can be simplified to

$$C_{fd}^K = \frac{\frac{K_{prim}^-}{K_{prim}^+}}{\frac{K_{prim}^- + K_{sym}^-}{K_{prim}^+ + K_{sym}^+}}. \quad (7.18)$$

This equation can be rearranged to give

$$C_{fd}^K = \left[1 + \alpha^K (1 - R_M^K) \right]^{-1}, \quad (7.19)$$

where R_M^K is defined as the measured K^-/K^+ ratio and α^K is equal to 0.1. Using Eq. 7.19, the correction factor to the kaon ratio for each data set and centrality bin can be calculated. The results of this calculation are listed in Table 7.8. Because the correction is small, it will be applied as a systematic scale error of ± 0.01 to the kaon ratio instead of as a correction factor.

7.2 Secondary Correction

As the primary collision products pass through the beam pipe and detector materials secondary particles are produced. Those which pass through the spectrometer may be reconstructed and identified along with the primary particles. Cuts are applied in the track selection stage of the analysis to reduce the number of secondary particles that are accepted, but a finite number still satisfy the selection criteria and their effect must be removed from the final antiparticle to particle ratios. The inclusion of secondary particles influences the ratios because particles are preferentially generated over antiparticles. For example, HIJING Monte-Carlo studies of p+p collision events that occur within the spectrometer acceptance and pass the event and track selection cuts show that the relative yields of secondary antiprotons and protons are 3 to 100, respectively. The most significant effect is observed in the \bar{p}/p ratio and the proton secondary correction factor is derived in this section. HIJING Monte-Carlo studies show that pion and kaon secondaries are symmetrically generated in both charge signs; therefore, no correction is necessary and a systematic scale error will be assigned to account for the inclusion of secondary particles.

7.2.1 Proton Secondary Correction

If it is assumed that the contribution from secondary antiprotons is negligible as found in HIJING Monte-Carlo simulations of p+p collisions, the true ratio of pri-

mary antiprotons to protons is given by

$$\frac{\bar{p}_{prim}}{p_{prim}} = C_{sec} * \left(\frac{\bar{p}_{meas}}{p_{meas}} \right) \approx C_{sec} * \left(\frac{\bar{p}_{prim}}{p_{prim} + p_{sec}} \right), \quad (7.20)$$

where the subscripts *prim*, *sec* and *meas* refer to primary, secondary and measured particles, respectively. Equation 7.20 can be rearranged to solve for the secondary correction factor C_{sec} ,

$$C_{sec} = \frac{(\bar{p}_{prim}/p_{prim})}{(\bar{p}_{prim})/(p_{prim} + p_{sec})}. \quad (7.21)$$

and reduces to

$$C_{sec} = 1 + \frac{p_{sec}}{p_{prim}}. \quad (7.22)$$

The ratio of secondary to primary protons and, hence the secondary correction factor can be determined using simulated collision events.

The yield of secondary protons accepted in the analysis was studied using d+Au and p+p HIJING Monte-Carlo events that were treated in an analogous manner to the data. The simulated events were processed using the same tracking algorithm as the data and the same event and track selection cuts were applied. The results of the study are shown in Fig. 7.4. In this figure the ratio of secondary to primary protons observed in d+Au collisions is shown for four centrality bins. The secondary to primary proton ratio can be fit with the functional form

$$\frac{p_{sec}}{p_{prim}}(p_T) = p_0 + e^{-(p_1 + p_2 * p_T)}. \quad (7.23)$$

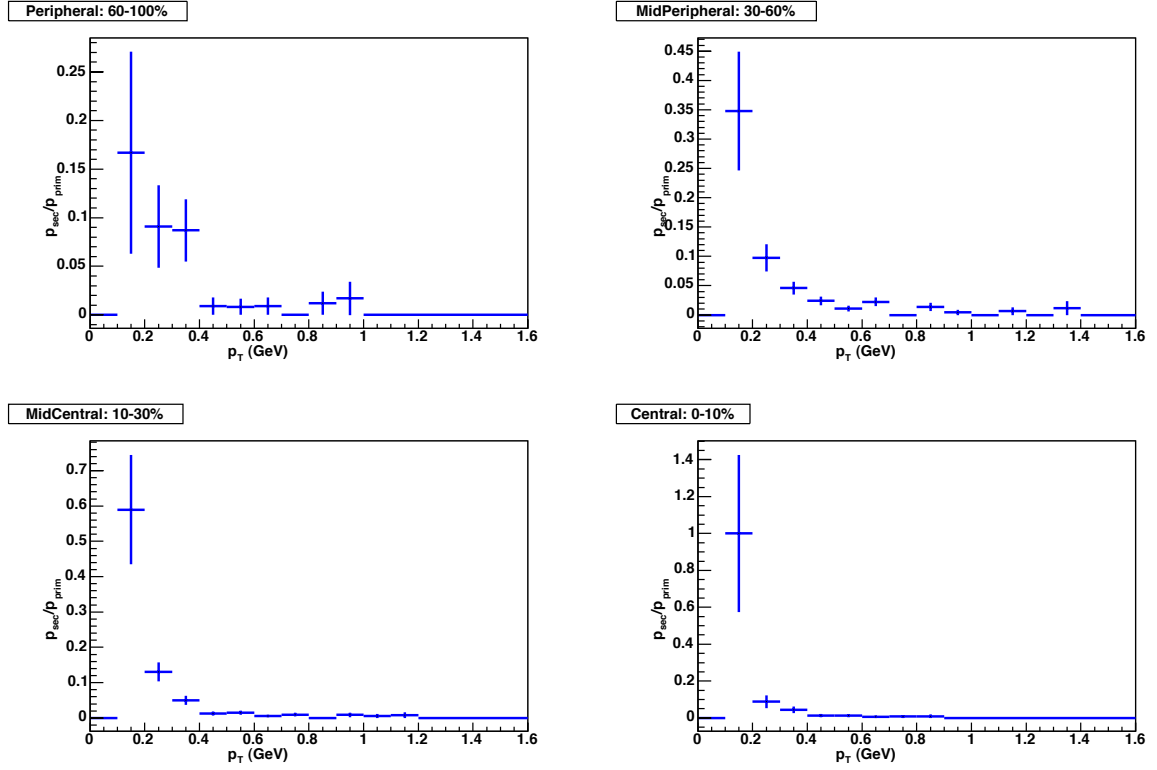


Figure 7.4: Ratio of secondary protons to primary protons in simulated d+Au HIJING Monte-Carlo events for four centrality bins.

This function is used to determine the secondary correction factor as a function of transverse momentum. A similar procedure is followed for p+p collisions. The fit parameters for Eq. 7.23 are given in Table 7.9 for the d+Au and p+p collision systems.

The final secondary correction factors for each centrality bin of the dAVertex and dAPeriph data sets are determined by weighting the fit functions of the $\frac{p_{sec}}{p_{prim}}(p_T)$ ratio by the proton transverse momentum distribution in each centrality bin. Due to the uncertainty in the determination of the $\frac{p_{sec}}{p_{prim}}(p_T)$ ratio for each centrality bin, as demonstrated by the large statistical error bars in Fig. 7.4, the minimum bias secondary correction function is applied uniformly to all of the bins.

Table 7.9: Fit Parameters for the Ratio of Secondary Protons to Primary Protons for d+Au and p+p Collisions

Collision System	Centrality	p_0	p_1	p_2	χ^2/ndf
d+Au	60-100%	0.00792	-0.826	12.7	3.7/4
d+Au	30-60%	0.00803	0.219	8.78	4.7/6
d+Au	10-30%	0.00696	-1.17	12.9	2.6/6
d+Au	0-10%	0.00691	-0.373	11.3	0.64/4
d+Au	MinBias	0.00479	-0.0600	9.28	7.0/8
p+p	MinBias	0.00617	-0.743	10.6	4.1/6

The final values of C_{sec} for the d+Au data sets and the p+p data set are

$$C_{sec} = \begin{cases} 1.016 \pm 0.003(stat, pt \text{ to } pt) \pm 0.002(syst, scale) & \text{if d+Au} \\ 1.021 \pm 0.003(stat) \pm 0.003(syst) & \text{if p+p.} \end{cases} \quad (7.24)$$

The systematic errors are a result of the dependence of the correction factor on the placement of the track selection cut that requires that each accepted track point back within 0.35 cm of the beam orbit and the dependence of the secondary study on the HIJING model. The statistical error is a result of the number of simulated HIJING events available for this study.

7.2.2 Pion and Kaon Secondary Correction

The effect of secondaries on the pion and kaon antiparticle to particle ratios can be investigated using simulated HIJING Monte-Carlo events. The ratios of the yields of primary and secondary pions and kaons as a function of transverse momentum are shown in Fig. 7.5 for minimum bias d+Au collisions. Vertex and trigger biases similar to those observed in the data have been applied to the simulated events. In

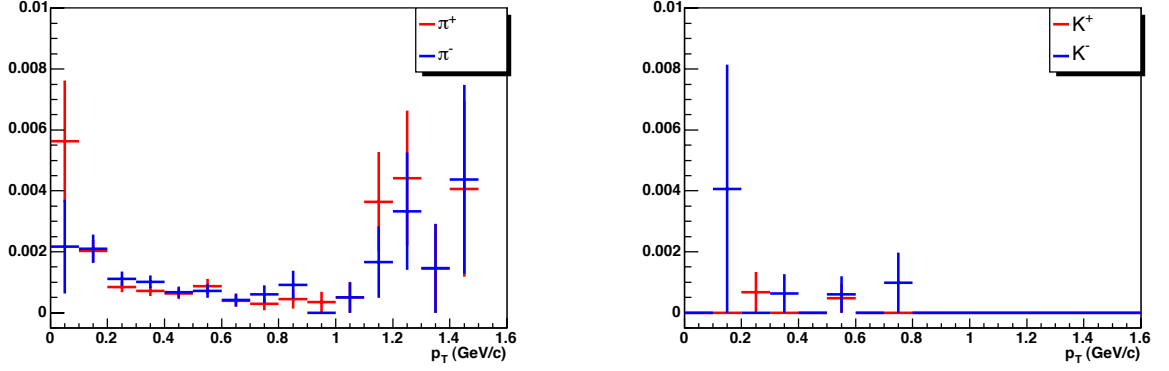


Figure 7.5: Secondary to primary ratio as a function of p_T for pions (left) and kaons (right) in simulated minimum bias d+Au HIJING Monte-Carlo events.

addition, the kinematic acceptance of the spectrometer and track selection dca cut have been applied. The fraction of pion secondaries is approximately 0.001 in the p_T range over which the π^-/π^+ ratio is measured, $0.1 < p_T < 1$ GeV/c. In the absence of the track selection dca cut the pion secondary fraction increases to 0.005, therefore a conservative scale systematic of ± 0.003 is assigned to the π^-/π^+ ratio. The fraction of kaon secondaries is less than 0.001 in the p_T range over which the K^-/K^+ ratio is measured, $0.1 < p_T < 1$ GeV/c. A scale systematic error of this magnitude is assigned to the ratio. The same results were obtained for both the d+Au and p+p collisions systems.

7.3 Absorption Correction

As a result of hadronic interactions within the detector materials some primary collision products are absorbed and never measured. These interactions predominantly effect the measured \bar{p}/p ratio. To account for this detector dependent process an

absorption correction C_{absorp} must be applied to the raw particle ratios. This correction is independent of the collision system; therefore, the following discussion applies to both the d+Au and p+p data sets. The magnitude of the absorption correction is determined by studying simulated particles that are projected through the detector using GEANT. Two different hadronic interaction packages are used to estimate the absorption, GEISHA [58] and FLUKA [59]. It is found that both packages produce similar absorption results for protons, but differ in their antiproton absorption correction.

The percentage of a given particle type that is absorbed in the detector material can be studied by comparing the results of simulations with and without including the effects of hadronic interactions. The proton absorption fraction is defined as the ratio of the number of proton tracks found when hadronic interactions are applied to the number of proton tracks found when no interactions are allowed,

$$A(p_T) = \left(\frac{p_{meas}^{had\ inter}}{p_{meas}^{no\ inter}} \right). \quad (7.25)$$

The proton absorption fraction as a function of transverse momentum for both magnetic field polarities is shown in Fig. 7.6. The points shown in red represent the absorption fraction determined using the FLUKA interaction package and the points shown in blue represent the absorption fraction determined using the GEISHA interaction package. No statistically significant difference is observed between the two different methods. The absorption fraction can be fit with a curve of the functional

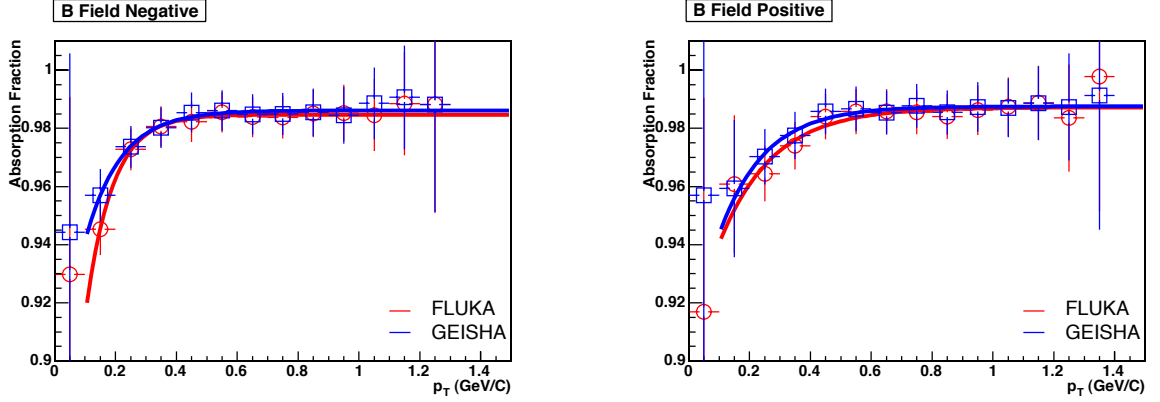


Figure 7.6: The proton absorption fraction as a function of transverse momentum for magnetic field polarity negative (left) and magnetic field polarity positive (right). The results in red are for the FLUKA hadronic interaction package and the results in blue are for GEISHA. The fit curves have the functional form shown in Eq. 7.26.

form,

$$A(p_T) = p_0 - e^{p_1 + p_2 p_T}. \quad (7.26)$$

The antiproton absorption fraction as a function of transverse momentum is shown in Fig. 7.7. A statistically significant difference is observed between the two interaction packages, particularly at low transverse momentum. This difference originates from different methods of determining interaction cross-sections [51] and will be accounted for when the final correction factor is calculated.

The absorption correction factor for each particle species is inversely related to the absorption factor,

$$C_{absorp}^{proton}(p_T) = [A^{proton}(p_T)]^{-1}. \quad (7.27)$$

To determine the net absorption correction factor that is used to correct the raw particle counts of each species, the absorption correction function must be weighted

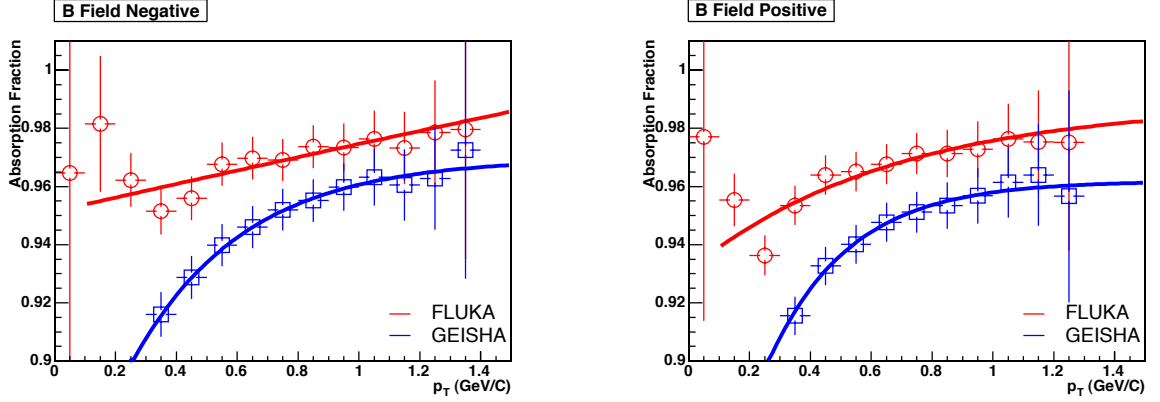


Figure 7.7: The antiproton absorption fraction as a function of transverse momentum for magnetic field polarity negative (left) and magnetic field polarity positive (right). The results in red are for the FLUKA hadronic interaction package and the results in blue are for GEISHA. The fit curves have the functional form shown in Eq. 7.26.

by the observed raw transverse momentum spectrum for that particle species. The final absorption correction to the \bar{p}/p ratio is the ratio of the correction factors for antiprotons and protons.

Studies of proton and antiproton absorption as a function of centrality indicate that the process is independent of collision centrality; therefore, the same correction function is applied to all centrality bins of the d+Au data sets. Furthermore, absorption is also found to be independent of the polarity of the applied magnetic field, thus the same correction is applied to particles of both bending directions. To account for the difference in the simulated antiproton absorption predicted by the two hadronic interaction packages, the final absorption correction factor is taken to be the average of the two. A systematic scale error equal to half the difference between the two packages is assigned to the correction. The final absorption correction

Table 7.10: Antiparticle to Particle Ratios for Each Centrality Bin

Trigger	Centrality	$\langle\pi^{-}\rangle/\langle\pi^{+}\rangle$	$\langle K^{-}\rangle/\langle K^{+}\rangle$	$\langle\bar{p}\rangle/\langle p\rangle$
dAVertex	60 – 100	0.995	0.97	0.84
dAVertex	30 – 60	1.004	0.95	0.80
dAVertex	10 – 30	1.008	0.97	0.83
dAVertex	0 – 10	1.016	0.97	0.86
dAPeriph	60 – 100	0.996	1.02	0.86
dAPeriph	30 – 60	1.014	0.97	0.82
ppVertex	MinBias	1.000	0.93	0.85

function is,

$$C_{absorp} = 1.035 \pm 0.014(\text{syst, scale}). \quad (7.28)$$

7.4 Final Particle Ratios

The final particle ratios are determined by multiplying the raw ratios by each of the correction factors,

$$R_{final} = R_{raw} * C_{fd} * C_{sec} * C_{absorp}. \quad (7.29)$$

The feed-down, secondary and absorption corrections need only to be applied to the antiproton to proton ratios. Because the correction factors determined for the pion and kaon ratios are small, they will be applied as systematic errors in Sec. 8.2, thus there is no difference between the raw and final pion and kaon ratios. The final ratios with all corrections applied are listed in Table 7.10. The product of each of the correction factors leads to a small increase in the final antiproton to proton ratios relative to the raw ratios.

Chapter 8

Error Analysis

Antiparticle to particle ratios are able to provide a sensitive measure of the properties of a collision system only if the statistical and systematic errors associated with the measurements are small. The statistical error is directly related to the amount of data collected, but the magnitude of the systematic error is dependent upon the detector system and analysis method used to make the antiparticle to particle ratios measurement. In this chapter a description of how the statistical and systematic errors of each measurement are determined is provided.

8.1 Statistical Error Calculation

The statistical error associated with a series of counting measurements that can be represented by a Poisson distribution is considered to be random and is equivalent to the standard deviation,

$$\sigma_N = \sqrt{N}, \quad (8.1)$$

where N is the number of counts recorded. The statistical error in the antiparticle to particle ratios is found by propagating the statistical error in the measurement of the number of events and the number of each individual particle species through to the final ratio. The formula used to determine the error in the event normalized particle yields, $\sigma_{species}^{norm}$, is

$$\sigma_{species}^{norm} = N_{species}^{norm} \left[\left(\frac{\sigma_{N_{species}}}{N_{species}} \right)^2 + \left(\frac{\sigma_{N_{event}}}{N_{event}} \right)^2 \right]^{1/2}, \quad (8.2)$$

where $N_{species}$ is the number of particles of a given species (π^+ , π^- , K^+ , K^- , p , \bar{p}) detected, N_{event} is the number of events detected and $N_{species}^{norm}$ is the event normalized number of particles of a given species. The statistical error in the event normalized particle yields is then used to determine the error in the antiparticle to particle ratios, $\sigma_{species}^R$, as given in Eq. 8.3 for the \bar{p}/p ratio,

$$\sigma_p^R = \frac{N_{\bar{p}}^{norm}}{N_p^{norm}} \left[\left(\frac{\sigma_p^{norm}}{N_p^{norm}} \right)^2 + \left(\frac{\sigma_{\bar{p}}^{norm}}{N_{\bar{p}}^{norm}} \right)^2 \right]^{1/2}. \quad (8.3)$$

An additional contribution to the statistical error of the \bar{p}/p ratio originates

Table 8.1: Antiparticle to Particle Ratios and Statistical Errors for Each Centrality Bin

Trigger	Centrality	$\langle\pi^{-}\rangle/\langle\pi^{+}\rangle$	$\langle K^{-}\rangle/\langle K^{+}\rangle$	$\langle\bar{p}\rangle/\langle p\rangle$
dAVertex	60 – 100	0.995 ± 0.015	0.97 ± 0.07	0.84 ± 0.04
dAVertex	30 – 60	1.004 ± 0.007	0.95 ± 0.03	0.80 ± 0.02
dAVertex	10 – 30	1.008 ± 0.006	0.97 ± 0.02	0.83 ± 0.02
dAVertex	0 – 10	1.016 ± 0.007	0.97 ± 0.03	0.86 ± 0.02
dAPeriph	60 – 100	0.996 ± 0.008	1.02 ± 0.04	0.86 ± 0.03
dAPeriph	30 – 60	1.014 ± 0.007	0.97 ± 0.03	0.82 ± 0.02
ppVertex	MinBias	1.000 ± 0.012	0.93 ± 0.05	0.85 ± 0.04

from the secondary correction to the ratio. The magnitude of this error, ± 0.003 , is derived in Section 7.2. The total statistical error in the \bar{p}/p ratio measurement is found by adding in quadrature the statistical error in the secondary correction and σ_p^R . The corrected antiparticle to particle ratios and the associated statistical errors in each of the measurements are shown in Table 8.1.

8.2 Systematic Error Calculation

The systematic errors associated with each antiparticle to particle ratio measurement are determined by examining the effects of varying the cuts used in the analysis on the final ratios. Four categories of cut systematics are investigated: event selection, track selection, centrality and particle identification. Tables 8.2 and 8.3 contain the details of each cut variation.

For each systematic variation and particle species the antiparticle to particle ratio and statistical error is calculated. The *variation ratios* can be compared to the standard antiparticle to particle ratios to determine if they deviate significantly

Table 8.2: Systematic Error Cut Variations

Event Selection Systematics dAVertex & dAPeriph		
Variable	Standard	Variation
Bunch Selectivity	AllT0Diagonal	AllT0Double
PileUp	PileUpRejection	NoPileUpRejection
OctDeVz Status	OctT0De	OctDeHpar OctDeTopo
OctDeVz Ranges	$ \text{OctDeVz} \leq 8 \text{ cm}$	$ \text{OctDeVz} \leq 7 \text{ cm}$ $ \text{OctDeVz} \leq 9 \text{ cm}$ $\text{OctDeVz} < 0 \text{ cm}$ $\text{OctDeVz} > 0 \text{ cm}$
Event Selection Systematics ppVertex		
Variable	Standard	Variation
Paddle Time	$ \text{PaddleTime} < 5 \text{ ns}$	$ \text{PaddleTime} < 4 \text{ ns}$ $ \text{PaddleTime} < 6 \text{ ns}$ $\text{PaddleTime} < 0 \text{ ns}$ $\text{PaddleTime} > 0 \text{ ns}$
Pile up	PileUpRejection	NoPileUpRejection
OctDeStatus	OctDeTopo	OctDeHpar
OctDeVz Ranges	$ \text{OctDeVz} \leq 8 \text{ cm}$	$ \text{OctDeVz} \leq 7 \text{ cm}$ $ \text{OctDeVz} \leq 9 \text{ cm}$ $\text{OctDeVz} < 0 \text{ cm}$ $\text{OctDeVz} > 0 \text{ cm}$
Centrality Determination Systematics dAVertex & dAPeriph		
Variable	Standard	Variation
Centrality Measure	ERing	EOct EPCAL
Centrality Cut	ERing	ERing*1.02 ERing*0.98 ERingBP*1.02 && ERingBM*0.98 ERingBP*0.98 && ERingBM*1.02
Centrality Scaling	ERing	ERing*1.02 ERing*0.98 ERingBP*1.02 && ERingBM*0.98 ERingBP*0.98 && ERingBM*1.02

Table 8.3: Systematic Error Cut Variations, continued

Track Selection Systematics		
Variable	Standard	Variation
Track Fit Probablity	Prob> 0.04	NoTrkFitCut Prob> 0.02 Prob> 0.06
Dca Cut	$ dca < 0.35 \text{ cm}$	NoDcaCut $ dca < 0.25 \text{ cm}$ (tight) $ dca < 0.45 \text{ cm}$ (loose)
Vertex Agreement	$ \text{TrkVz-OctDeVz} < 6 \text{ cm}$	NoVzAgreeCut $ \text{TrkVz-OctDeVz} < 4 \text{ cm}$ $ \text{TrkVz-OctDeVz} < 8 \text{ cm}$
p_T Cut	$p_T > 0.1 \text{ } (\pi, K)$ $p_T > 0.3 \text{ (p)}$	$p_T > 0.0$ $p_T > 0.1$ $p_T > 0.2$ $p_T > 0.3$ $p_T > 0.4$
Particle Identification Systematics		
Variable	Standard	Variation
dE/dx Cut:	$dE/dx > 1.45$	$\sigma = 2$
Band Sigma Variation	$\sigma = 3$	$\sigma = 4$
dE/dx Cut:	$dE/dx > 1.45$	$dE/dx > 1.5$
dE/dx Cut Variation	$\sigma = 3$	$dE/dx > 1.4$
P Cut:	$p_\pi < 0.55$	$\sigma = 2$
Band Sigma Variation	$p_K < 0.45$ $p_p < 0.85$ $\sigma = 3$	$\sigma = 4$
p Cut:	$p_\pi < 0.55$	$p_\pi < 0.50, p_\pi < 0.65$
p Cut Variation	$p_K < 0.45$ $p_p < 0.85$ $\sigma = 3$	$p_K < 0.43, p_K < 0.47$ $p_p < 0.83, p_p < 0.87$
Other Systematics		
Variable	Standard	Variation
Vz Counts Correction	Corrected	NotCorrected
Dead Channel Map	NotApplied	Applied
Spectrometer Arm	SpecArmN && SpecArmP	SpecArmN SpecArmP
Beam Orbit Region: dAVertex	All Regions	Region 0, Region 1 Region 2, Region 3
Beam Orbit Region: dAPeriph & ppVertex	All Regions	Region 0 Region 1

from the standard. This is done by calculating the relative ratio, which is defined as the difference between the variation ratio and the standard ratio. If the variation ratio does not deviate significantly from the standard ratio, then the relative ratio will lie within the statistical error of zero; however, if the variation ratio does deviate significantly then a systematic error is assigned. As an example, Figure 8.1 contains the relative ratio plots for the Track Selection Systematic DCA Cut for the dAVertex data set. For the pion and kaon ratios the loose and tight dca cuts do not cause the ratios to vary significantly from the standard. Conservatively, a maximum systematic scale error of ± 0.001 can be assigned to the pion and kaon ratios. In contrast, the tight dca cut does cause the proton variation ratio to deviate significantly from the standard ratio. A systematic scale error is assigned to the proton ratio that is equal to the magnitude of the deviation, ± 0.005 . A scale error is assigned because the tight dca cut variation consistently results in a lower relative ratio than the standard for all centrality classes. A point-to-point systematic error is assigned when the relative ratio deviates significantly from the standard, but is not consistently lower or higher than the standard for each centrality bin. The distinction between point-to-point and scale systematic errors cannot be made for the ppVertex data set because the ratios are not measured as a function of centrality. Due to the limited number of kaons and protons in the ppVertex data, the systematic error estimate from the pions is used when the kaon and proton measurements are statistically limited. The procedure outlined is followed for each systematic variable listed in Tables 8.2 and 8.3. The resulting systematic errors are documented in Appendix C for the dAVertex and dAPeriph data sets and in Appendix D for the ppVertex data

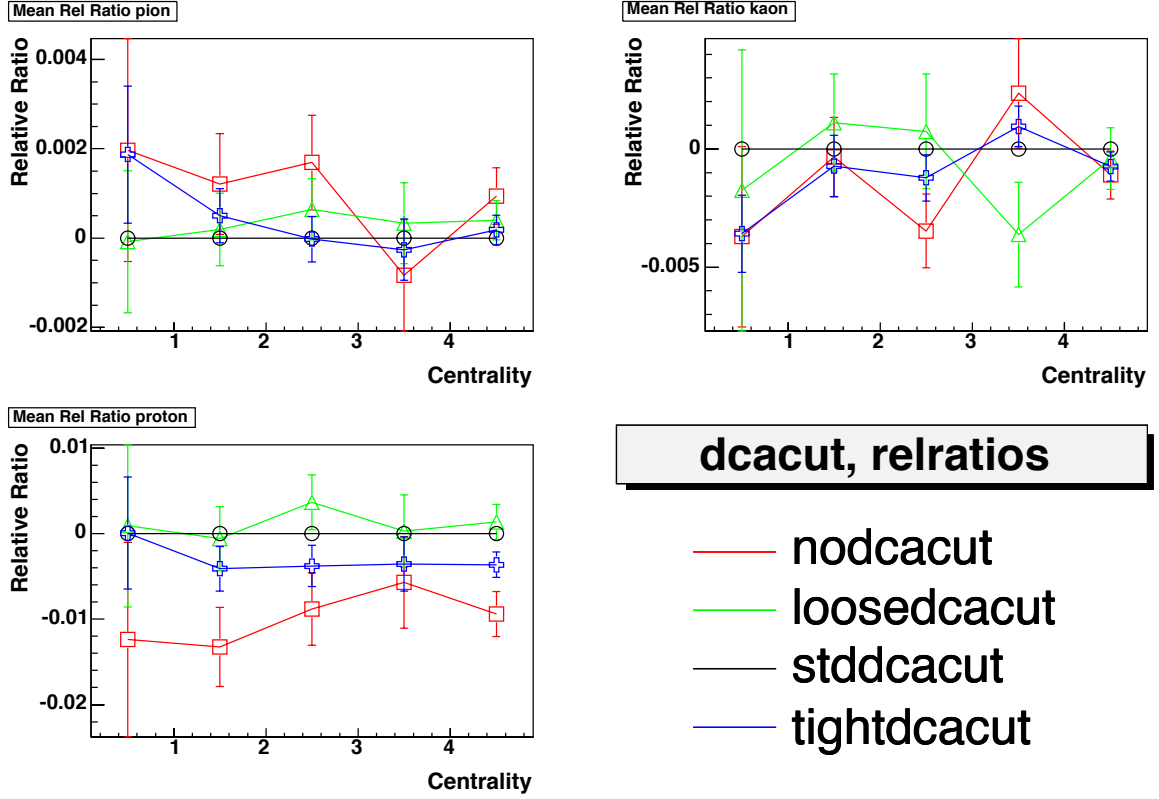


Figure 8.1: Relative ratio plots for pions (upper left), kaons (upper right) and protons (lower left) for the Track Selection Systematic DCA Cut for the dAVertex data set. The x-axis represents centrality, with $x=0.5$ peripheral, $x=1.5$ midperipheral, $x=2.5$ midcentral, $x=3.5$ central, and $x=4.5$ minimum bias.

set.

An additional source of systematic error exists in the analysis. This error originates from the correction factors that are applied to the raw ratios. The systematic errors associated with each correction factor are determined in Chapter 7. Table 8.4 contains a summary of these errors.

The final systematic error associated with each measured antiparticle to particle ratio is calculated independently for each data set by adding the contribution from each individual source shown in Appendix C, Appendix D and Table 8.4 in

Table 8.4: Systematic Error from Correction Factors

Correction	Species	dAVertex		dAPeriph		ppVertex Total
		Pt-to-Pt	Scale	Pt-to-Pt	Scale	
Feed-down	π	0	± 0.005	0	± 0.005	± 0.005
	K	0	± 0.01	0	± 0.01	± 0.01
	p	± 0.01	± 0.001	± 0.006	± 0.001	± 0.010
Secondary	π	0	± 0.003	0	± 0.003	± 0.003
	K	0	± 0.001	0	± 0.001	± 0.001
	p	0	± 0.002	0	± 0.002	± 0.003
Absorption	π	0	0	0	0	0
	K	0	0	0	0	0
	p	0	± 0.014	0	± 0.014	± 0.014
Electron Contamination	π	0	± 0.001	0	± 0.001	± 0.001
	K	0	0	0	0	0
	p	0	0	0	0	0

quadrature as shown in Eq. 8.4,

$$\sigma_{sys} = \left(\sigma_1^2 + \sigma_2^2 + \sigma_3^2 + \dots + \sigma_i^2 \right)^{1/2}. \quad (8.4)$$

The final antiparticle to particle ratios are shown with their associated statistical and systematic errors in Table 8.5. For the d+Au data sets the point-to-point and scale systematic errors have been added in quadrature.

Table 8.5: Antiparticle to Particle Ratios, Statistical Errors and Systematic Errors for Each Centrality Bin.

Trigger	Centrality	$\langle\pi^{-}\rangle/\langle\pi^{+}\rangle$	$\langle K^{-}\rangle/\langle K^{+}\rangle$	$\langle\bar{p}\rangle/\langle p\rangle$
dAVertex	60 – 100	$0.995 \pm 0.015 \pm 0.017$	$0.97 \pm 0.07 \pm 0.03$	$0.84 \pm 0.04 \pm 0.04$
dAVertex	30 – 60	$1.004 \pm 0.007 \pm 0.017$	$0.95 \pm 0.03 \pm 0.03$	$0.80 \pm 0.02 \pm 0.03$
dAVertex	10 – 30	$1.008 \pm 0.006 \pm 0.017$	$0.97 \pm 0.02 \pm 0.03$	$0.83 \pm 0.02 \pm 0.03$
dAVertex	0 – 10	$1.016 \pm 0.007 \pm 0.017$	$0.97 \pm 0.03 \pm 0.03$	$0.86 \pm 0.02 \pm 0.03$
dAPeriph	60 – 100	$0.996 \pm 0.008 \pm 0.017$	$1.02 \pm 0.04 \pm 0.04$	$0.86 \pm 0.03 \pm 0.03$
dAPeriph	30 – 60	$1.014 \pm 0.007 \pm 0.017$	$0.97 \pm 0.03 \pm 0.04$	$0.82 \pm 0.02 \pm 0.03$
ppVertex	MinBias	$1.000 \pm 0.012 \pm 0.019$	$0.93 \pm 0.05 \pm 0.03$	$0.85 \pm 0.04 \pm 0.03$

Chapter 9

Results and Discussion

The final antiparticle to particle ratios in 200 GeV p+p and d+Au collisions can be used to examine the underlying dynamics of the collision systems. Comparison of the measured ratios with model predictions and more complicated heavy ion collisions provides insight into the differences between the collision systems and the amount of baryon number transport that occurs. In this chapter the centrality dependence of the antiparticle to particle ratios is investigated and the evolution of the $\langle \bar{p}/p \rangle$ ratio as a function of collision energy in p+p and heavy ion collisions is examined. Furthermore, the implications of these results on the physical collision processes are discussed.

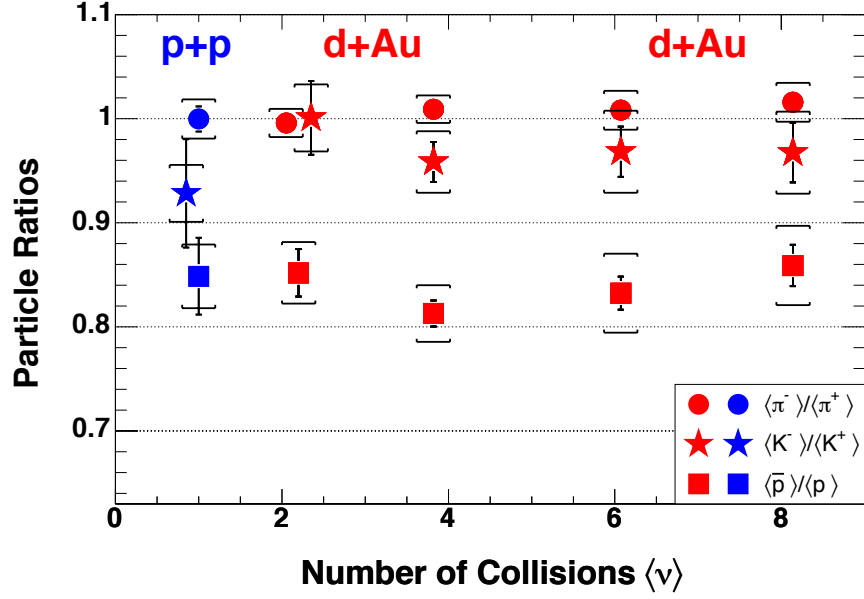


Figure 9.1: Particle ratios plotted versus centrality for the d+Au and p+p 200 GeV collision systems. The blue symbols represent the results obtained for the p+p collision system and the red symbols are for the d+Au collision system.

9.1 Results

9.1.1 Centrality Dependence of Ratios

The ratios of the yields of primary antiparticles to particles produced in 200 GeV p+p and d+Au collisions are plotted as a function of collision centrality, represented by $\langle \nu \rangle$, in Fig. 9.1. Table 3.8 lists the values of $\langle \nu \rangle$ for each centrality bin. In the d+Au collision system, the points shown for the peripheral and mid-peripheral centrality bins represent the statistically weighted average of the results obtained from the dAVertex and dAPeriph data sets. The square brackets represent the total systematic error in the measurements. For the d+Au measurements the total systematic error is found by adding the point-to-point and scale systematic errors in quadrature. In the d+Au collision system, within the statistical and systematic

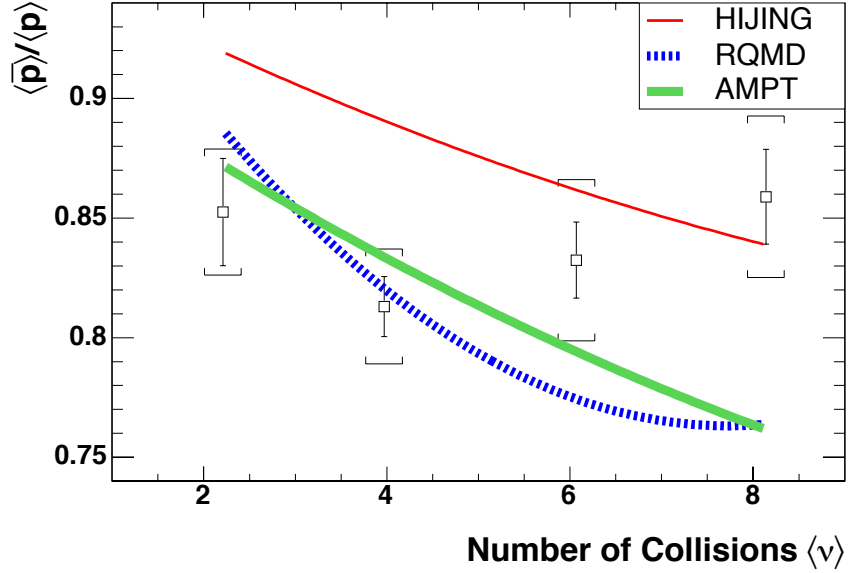


Figure 9.2: The antiproton to proton ratio plotted versus number of collisions $\langle \nu \rangle$ for 200 GeV d+Au collisions is shown as open squares. The brackets represent the point-to-point systematic error in the measurements. The lines represent fits to the model predictions. The statistical error in the models is less than 2%.

errors, the ratios of all three species appear to be independent of centrality. In addition, it is observed that the results obtained for the p+p collision system are consistent with those obtained for the d+Au collision system at all centralities.

9.1.2 Comparison with Models

The measured $\langle \bar{p} \rangle / \langle p \rangle$ ratio in d+Au collisions as a function of centrality is shown compared to the results from HIJING [12], RQMD [22] and AMPT [14, 15] in Fig. 9.2. The d+Au collision events generated by the models were subjected to a simulation of the PHOBOS detector and the same trigger, event, and particle selection biases as used in the data analysis. All of the models demonstrate a decreasing $\langle \bar{p} \rangle / \langle p \rangle$ ratio with increasing $\langle \nu \rangle$. However, the suppression of the ratio

with increasing centrality seen in the models is not observed in the data.

9.2 Discussion

To interpret the results obtained in this thesis it is necessary to compare the values with measurements obtained from other collision systems and energies. The antiparticle to particle ratios in Au+Au collisions at RHIC energies have also been reported at a variety of energies and centralities. In addition, measurements conducted at the AGS, SPS and ISR can be used to study the evolution of the $\langle\bar{p}\rangle/\langle p\rangle$ ratio as a function of collision energy in heavy ion and p+p collisions.

9.2.1 RHIC $\langle\bar{p}\rangle/\langle p\rangle$ Ratio

A comparison of the $\langle\bar{p}\rangle/\langle p\rangle$ ratio measured by the RHIC experiments for a wide range of collision species and energies is shown in Fig. 9.3. Remarkable agreement is observed between the independently obtained results from each of the experiments. Within the statistical and systematic uncertainties in the measurements, the reported values for the 200 GeV Au+Au and d+Au collisions all agree. In the 130 GeV Au+Au and 200 GeV p+p collision systems some small discrepancies remain to be resolved. It should be noted that all of the PHOBOS measurements have been fully corrected for non-primary contaminates, whereas many of the other experiments do not correct for feed-down particles from weak decays. Depending upon the acceptance of the experiment, feed-down products from weak decays can account for as much as 33% of the measured p and \bar{p} yields [39]. The Brahms exper-

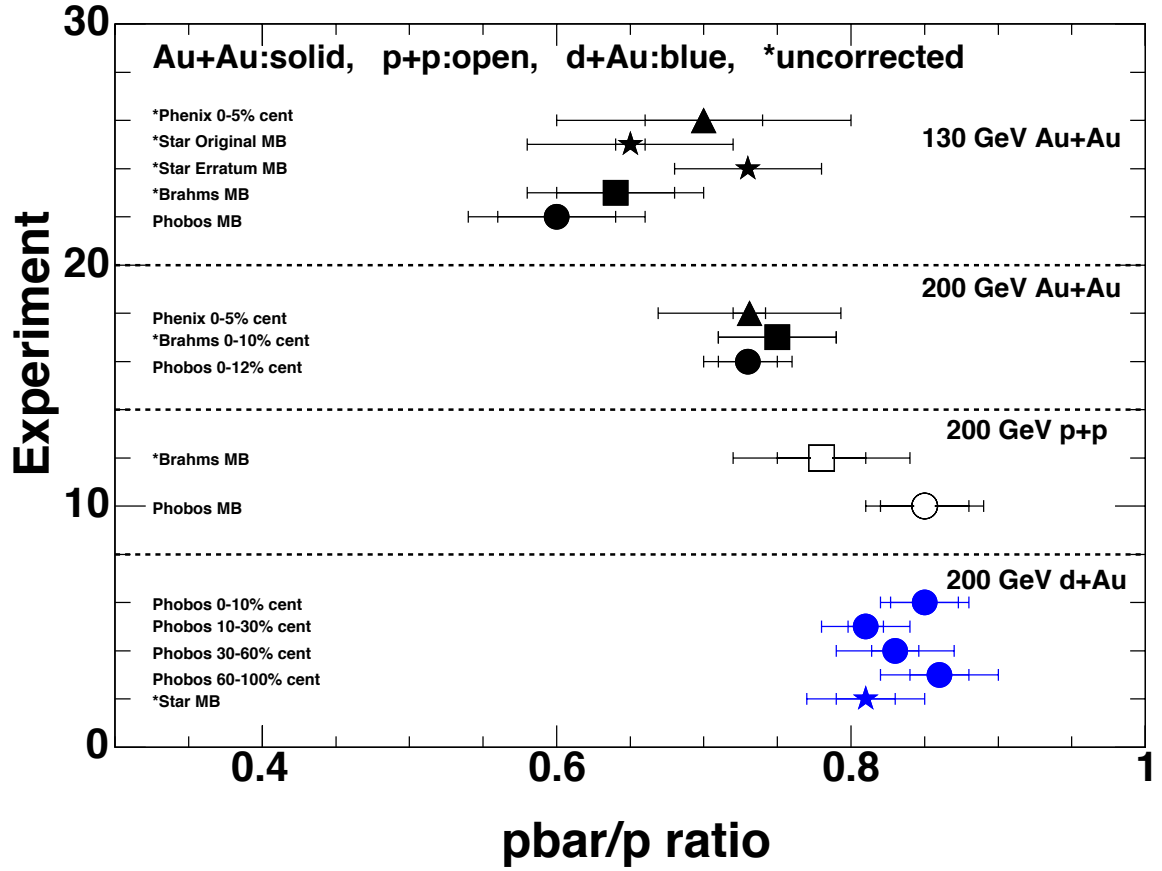


Figure 9.3: The $\langle \bar{p} \rangle / \langle p \rangle$ ratio reported by all of the RHIC experiments for a variety of collision species and energies. The Au+Au collision system is represented by solid black symbols, the open symbols are used for the p+p system and the d+Au system is represented by solid blue symbols. Results labeled with an asterisk have not been corrected for feed-down products from weak decays. [30, 31, 33, 34, 35, 36, 39, 46, 60, 61, 62]

iment has estimated that inclusion of feed-down products increases their measured $\langle \bar{p} \rangle / \langle p \rangle$ ratios by less than 5% [30, 35, 61].

9.2.2 Comparison with Au+Au Collisions

The antiparticle to particle ratios as a function of collision centrality for 0-50% central 200 GeV Au+Au collisions divided into five centrality bins representing 0-10% most central, 10-20%, 20-30%, 30-40% and 40-50% central collisions as detected

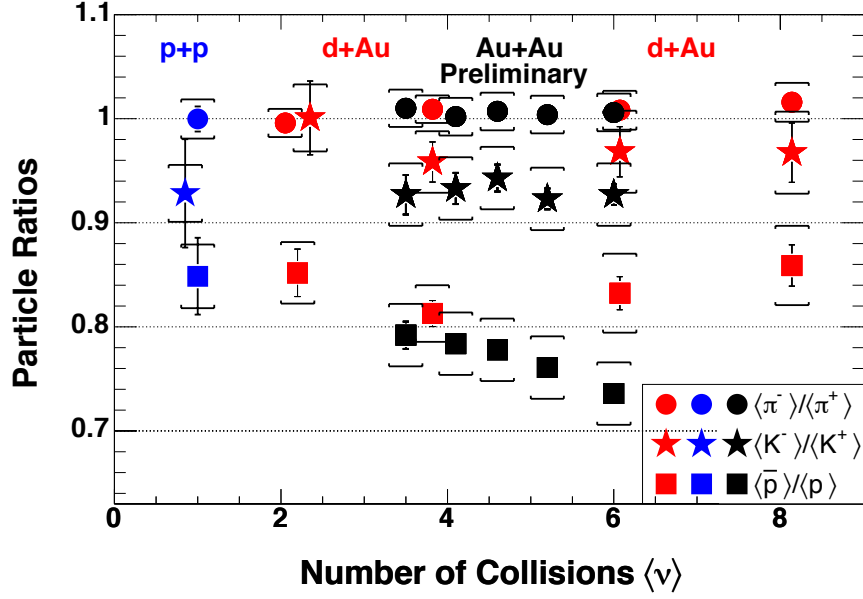


Figure 9.4: Particle ratios measured in the PHOBOS detector plotted versus centrality for the d+Au, p+p and Au+Au collisions at 200 GeV. The Au+Au data, shown as black points, is divided into five centrality bins representing 0-10% most central, 10-20%, 20-20%, 30-40% and 40-50% central collisions. [37]

in the PHOBOS experiment have been reported [37]. The values of $\langle \nu \rangle$ for each of these bins are 6.0, 5.2, 4.6, 4.1, and 3.5, respectively. These ratios provide insight into the different collision conditions in Au+Au collisions as compared to the more simple d+Au and p+p collision systems. Figure 9.4 shows the particle ratios for all three collision systems plotted as a function of $\langle \nu \rangle$. The pion and kaon ratios agree between the three systems at all centralities. In contrast, the 0-10% central Au+Au proton ratio is significantly lower than the ratios measured in p+p collisions and in all of the centrality bins in the d+Au collisions. However as $\langle \nu \rangle$ decreases, the results reported for Au+Au collisions approach the values measured in p+p and d+Au collisions. This is discussed further in Sec. 9.2.4.

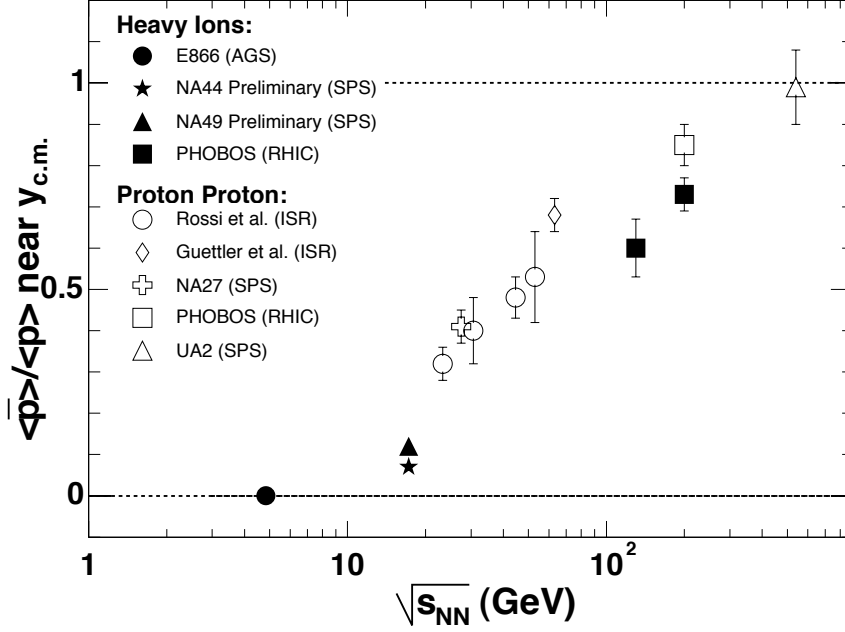


Figure 9.5: Antiproton to proton ratio near midrapidity plotted versus center-of-mass collision energy for p+p (open symbols), central Pb+Pb (solid star and triangle) and central Au+Au (solid circle and squares) collisions. The error bars represent the statistical and systematic errors in the measurements added in quadrature. [31, 34, 63, 64, 65, 66, 67, 68, 69, 70]

9.2.3 Energy Dependence of Ratios

The difference in the $\langle \bar{p} \rangle / \langle p \rangle$ ratio in p+p and Au+Au collisions can be investigated further by examining the evolution of the ratio as a function of collision energy. The $\langle \bar{p} \rangle / \langle p \rangle$ ratio near midrapidity as a function of center-of-mass energy for p+p collisions is shown in Fig. 9.5 using open symbols [69, 70, 65, 66]. The data indicate a smooth evolution from low to high energy. Also shown in Fig. 9.5 as solid symbols is the $\langle \bar{p} \rangle / \langle p \rangle$ ratio near midrapidity for central heavy ion collisions [31, 34, 63, 64, 67, 68]. The results from PHOBOS for 130 and 200 GeV Au+Au collisions [31, 34] have similar acceptances as reported here for 200 GeV p+p collisions (Sec. 5.4). A suppression of the $\langle \bar{p} \rangle / \langle p \rangle$ ratio is observed in the heavy ion data relative to p+p

over approximately an order of magnitude in the collision energy. The evolution of the ratio as a function of center-of-mass energy seems to be similar in shape for the two systems, with the heavy ion data offset by a factor of about two in collision energy.

9.2.4 Baryon Number Transport

The $\langle\bar{p}\rangle/\langle p\rangle$ ratio measured for 200 GeV p+p, d+Au and Au+Au collisions reveals that a net baryon free region is not achieved because the yield of primary protons continues to be greater than that of primary antiprotons. Because the particle yields are measured at midrapidity, the relative fraction of transported to produced protons can be determined using the measured $\langle\bar{p}\rangle/\langle p\rangle$ ratio. To be observed at midrapidity, a particle must either be produced in the collision at midrapidity or transported to midrapidity from beam rapidity, since the momentum of the incident nucleons is directed longitudinally with the beam. Assuming that the total yield of protons produced in a collision is the sum of a transported component and a produced component, the $\langle\bar{p}\rangle/\langle p\rangle$ ratio can be expressed as

$$\frac{\langle\bar{p}\rangle}{\langle p\rangle} = \frac{\bar{p}_{prod}}{p_{prod} + p_{trans}}, \quad (9.1)$$

where the subscripts *prod* and *trans* indicate the produced and transported yields, respectively. The pair production mechanism is symmetric; therefore, \bar{p}_{prod} is equal

to p_{prod} . This allows Eq. 9.1 to be rearranged

$$\frac{p_{trans}}{p_{prod}} = \frac{\langle p \rangle}{\langle \bar{p} \rangle} - 1. \quad (9.2)$$

Equation 9.2 reveals that the value $\langle p \rangle / \langle \bar{p} \rangle - 1$ is a measure of the relative fraction of transported protons to produced protons.

The relative fraction of transported protons in a central d+Au and Au+Au collisions can be calculated using Eq. 9.2. For the 0-10% most central d+Au collisions $p_{trans}/p_{prod} = 0.16$, and for the 0-10% most central Au+Au collisions $p_{trans}/p_{prod} = 0.35$ [37]. A comparison of the d+Au and Au+Au results shows that the relative fraction of transported protons in a central d+Au collision is approximately half that observed in a central Au+Au collision, despite the larger value of $\langle \nu \rangle$ in the central d+Au collisions. In addition, the relative fraction of transported protons in central d+Au collisions is the same as that found in p+p collisions. Both of these results are in contrast with the expectation that the more collisions a participating nucleon suffers, the greater the baryon number transport to midrapidity [40, 41]. This discrepancy calls into question whether the mechanism by which baryon number transport occurs can be modeled as a simple series of nucleon-nucleon collisions that divert the trajectory of the incident proton away from beam rapidity.

9.3 Conclusions

Comparison of the results obtained in this thesis with the antiparticle to particle ratios measured in Au+Au collisions at the same energy allows the influence of final state interactions and baryon number transport to be investigated. The antiparticle to particle ratios measured in 200 GeV p+p and d+Au collisions represent the initially produced yields of each particle species since little reinteraction is expected to occur in these systems. However, in the 200 GeV Au+Au collision system evidence of final state interactions has been found. The agreement of the $\langle\pi^- \rangle/\langle\pi^+ \rangle$ and $\langle K^- \rangle/\langle K^+ \rangle$ ratios for all three collision systems at all centralities suggests that any final state interactions present in Au+Au collisions do not modify the ratio of the initially produced meson yields. In contrast, comparison of the $\langle\bar{p} \rangle/\langle p \rangle$ ratio measured in each of the collision systems potentially provides evidence of collective behavior that affects baryons in central Au+Au collisions that is not present in p+p and d+Au collisions.

Contrary to model predictions, it is found that the relative amount of baryon number transport in d+Au collisions does not increase as the average number of collisions each participating nucleon suffers increases. Surprisingly, it is found that the relative fraction of transported to produced protons in central d+Au collisions is half that observed in central Au+Au collisions and the same as in p+p collisions. Furthermore, comparison of the $\langle\bar{p} \rangle/\langle p \rangle$ ratio in p+p collisions versus Pb+Pb and Au+Au collisions as a function of collision energy reveals a smooth evolution of the ratio from low to high energy.

The results reported in this thesis provide input to theoretical comparisons of the relative degree of baryon number transport and antibaryon-baryon pair formation observed in p+p, d+Au and heavy ion collisions and provide further information concerning the different dynamics that influence the evolution of each system. The disagreement between the results reported here and the model predictions suggests that the baryon number transport mechanism implemented in the model calculations must be modified for these collision regimes. A useful probe of the baryon number transport process will be the measurement of the $\langle \bar{p} \rangle / \langle p \rangle$ ratio over the full range in centrality for 200 GeV Cu+Cu and Au+Au collisions. These measurements will reveal whether ultra-peripheral Au+Au collisions resemble p+p collisions and could provide information concerning the onset of final state interactions.

Appendix A

PHOBOS Collaboration List

B.B.Back¹, M.D.Baker², M.Ballintijn⁴, D.S.Barton², B.Becker², R.R.Betts⁶, A.A.Bickley⁷, R.Bindel⁷, W.Busza⁴, A.Carroll², M.P.Decowski⁴, E.García⁶, T.Gburek³, N.George², K.Gulbrandsen⁴, S.Gushue², C.Halliwell⁶, J.Hamblen⁸, A.S.Harrington⁸, C.Henderson⁴, D.J.Hofman⁶, R.S.Hollis⁶, R.Hołyński³, B.Holzman², A.Iordanova⁶, E.Johnson⁸, J.L.Kane⁴, N.Khan⁸, P.Kulinich⁴, C.M.Kuo⁵, J.W.Lee⁴, W.T.Lin⁵, S.Manly⁸, A.C.Mignerey⁷, R.Nouicer^{2,6}, A.Olszewski³, R.Pak², I.C.Park⁸, H.Pernegger⁴, C.Reed⁴, C.Roland⁴, G.Roland⁴, J.Sagerer⁶, P.Sarin⁴, I.Sedykh², W.Skulski⁸, C.E.Smith⁶, P.Steinberg², G.S.F.Stephans⁴, A.Sukhanov², M.B.Tonjes⁷, A.Trzupek³, C.Vale⁴, G.J.van Nieuwenhuizen⁴, R.Verdier⁴, G.I.Veress⁴, F.L.H.Wolfs⁸, B.Wosiek³, K.Woźniak³, B.Wysłouch⁴, J.Zhang⁴

¹ Argonne National Laboratory, Argonne, IL 60439-4843, USA

² Brookhaven National Laboratory, Upton, NY 11973-5000, USA

³ Institute of Nuclear Physics, Kraków, Poland

⁴ Massachusetts Institute of Technology, Cambridge, MA 02139-4307, USA

⁵ National Central University, Chung-Li, Taiwan

⁶ University of Illinois at Chicago, Chicago, IL 60607-7059, USA

⁷ University of Maryland, College Park, MD 20742, USA

⁸ University of Rochester, Rochester, NY 14627, USA

Appendix B

Raw Particle and Event Counts

Table B.1: Summary of Weighted π^- and Event Counts for All Data Sets

Trigger	Centrality	BO	nEvents B^+	nTracks B^+		nEvents B^-	nTracks B^-	
				arm N	arm P		arm N	armP
dAVertex	60-100%	0	253107	3526.9	4159.3	73873	249.0	307.0
		1	141599	2043.2	2338.2	225234	812.5	952.7
		2	287792	4207.9	4702.3	197822	648.2	795.8
		3	153573	2230.7	2371.6	263854	918.2	1021.2
dAVertex	30-60%	0	456294	13776.1	16360.0	132953	936.7	1232.9
		1	262671	8140.0	9297.9	415791	3133.3	3601.6
		2	534937	17132.3	19052.7	375660	2704.0	3303.8
		3	287727	9190.5	10059.4	507318	3839.8	4454.0
dAVertex	10-30%	0	349935	16400.9	19487.9	101571	1221.4	1438.1
		1	202633	9656.0	10807.3	320457	3859.0	4414.7
		2	412234	20006.2	22318.1	292193	3371.5	3982.3
		3	221285	11036.8	11851.7	396562	4630.0	5474.2
dAVertex	0-10%	0	167952	10529.7	12458.6	48801	745.0	934.5
		1	98475	6209.5	7118.4	154719	2488.0	2817.5
		2	200990	12960.9	14709.4	143321	2297.3	2566.1
		3	108846	7128.0	7811.9	197049	3158.0	3725.4
dAPeriph	60-100%	0	405257	5094.9	5903.1	362144	893.1	1050.7
		1	1206211	14875.1	17057.9	1148409	2930.9	3380.3
dAPeriph	30-60%	0	425050	8617.1	9884.7	396956	1538.1	1923.5
		1	1230798	24598.3	28441.8	1129980	4732.4	5471.7
ppVertex	MinBias	0	194378	1762.2	1981.3	143230	270.0	347.3
		1	648729	5835.8	6655.3	1125723	2202.9	2413.0

Table B.2: Summary of Weighted π^+ and Event Counts for All Data Sets

Trigger	Centrality	BO	nEvents B^+	nTracks B^+		nEvents B^-	nTracks B^-	
				arm N	arm P		arm N	armP
dAVertex	60-100%	0	253107	855.1	1041.5	73873	1037.8	1204.8
		1	141599	470.7	596.6	225234	3136.9	3702.0
		2	287792	939.8	1208.0	197822	2735.8	3176.0
		3	153573	544.1	584.2	263854	3800.0	4109.3
dAVertex	30-60%	0	456294	3431.6	4089.5	132953	4098.4	4734.7
		1	262671	2037.5	2338.1	415791	12358.5	14848
		2	534937	3988.9	4581.4	375660	11529.3	13354.8
		3	287727	2238.9	2502.9	507318	15937.9	17382.7
dAVertex	10-30%	0	349935	4168.4	4804.5	101571	4842.7	5496.0
		1	202633	2341.2	2709.8	320457	14452.9	17374.9
		2	412234	4829.6	5529.5	292193	13710.4	15671.0
		3	221285	2633.5	3003.4	396562	18920.6	21044.8
dAVertex	0-10%	0	167952	2674.9	3215.3	48801	3039.6	3600.0
		1	98475	1545.7	1800.6	154719	9328.6	11405.7
		2	200990	3081.9	3648.5	143321	8994.9	10370.3
		3	108846	1664.0	1985.6	197049	12732.6	13980.5
dAPeriph	60-100%	0	405257	998.4	1134.2	362144	4509.6	5215.1
		1	1206211	3095.4	3569.4	1148409	14277.7	16527.6
dAPeriph	30-60%	0	425050	1645.9	1885.9	396956	7922.8	9148.6
		1	1230798	4984.3	5919.3	1129980	22450.3	26277.0
ppVertex	MinBias	0	194378	390.9	450.0	143230	1222.4	1451.3
		1	648729	1235.4	1423.8	1125723	10198.3	11605.6

Table B.3: Summary of Weighted K^- and Event Counts for All Data Sets

Trigger	Centrality	BO	nEvents B^+	nTracks B^+		nEvents B^-	nTracks B^-	
				arm N	arm P		arm N	armP
dAVertex	60-100%	0	253107	86.8	68.8	73873	6.0	4.0
		1	141599	52.0	47.0	225234	16.0	25.0
		2	287792	93.9	103.0	197822	12.0	17.0
		3	153573	44.1	59.3	263854	22.9	27.7
dAVertex	30-60%	0	456294	296.3	341.3	132953	24.2	29.2
		1	262671	172.0	223.9	415791	79.1	99.1
		2	534937	355.8	404.6	375660	62.2	90.3
		3	287727	202.4	221.3	507318	90.2	114.1
dAVertex	10-30%	0	349935	394.2	404.9	101571	34.1	39.2
		1	202633	226.9	243.9	320457	81.1	105.1
		2	412234	471.5	530.6	292193	77.2	92.1
		3	221285	243.3	291.9	396562	120.9	127.9
dAVertex	0-10%	0	167952	245.6	298.8	48801	20.0	23.3
		1	98475	143.9	170.9	154719	44.0	84.1
		2	200990	293.5	340.5	143321	56.2	86.2
		3	108846	152.4	173.6	197049	71.3	111.7
dAPeriph	60-100%	0	405257	145.3	227.6	362144	51.7	75.6
		1	1206211	518.7	617.3	1148409	162.9	164.9
dAPeriph	30-60%	0	425050	269.3	347.7	396956	90.6	100.3
		1	1230798	813.9	1017.9	1129980	252.5	293.8
ppVertex	MinBias	0	194378	62.2	87.2	143230	18.9	22.8
		1	648729	183.2	218.4	1125723	99.7	145.3

Table B.4: Summary of Weighted K^+ and Event Counts for All Data Sets

Trigger	Centrality	BO	nEvents B^+	nTracks B^+		nEvents B^-	nTracks B^-	
				arm N	arm P		arm N	armP
dAVertex	60-100%	0	253107	22.9	21.8	73873	23.0	27.0
		1	141599	15.0	8.0	225234	82.0	108.0
		2	287792	9.9	32.9	197822	71.1	73.1
		3	153573	16.1	11.1	263854	98.9	101.1
dAVertex	30-60%	0	456294	105.2	104.3	132953	86.1	97.4
		1	262671	53.9	60.9	415791	321.1	358.1
		2	534937	113.6	137.6	375660	235.2	274.1
		3	287727	69.8	75.5	507318	351.9	434.3
dAVertex	10-30%	0	349935	100.4	116.2	101571	102.2	113.2
		1	202633	52.9	86.9	320457	320.1	404.2
		2	412234	112.6	159.4	292193	337.3	395.4
		3	221285	56.5	63.4	396562	429.4	524.2
dAVertex	0-10%	0	167952	80.3	78.3	48801	70.2	89.0
		1	98475	40.0	41.0	154719	246.1	270.1
		2	200990	76.8	94.6	143321	172.1	251.3
		3	108846	47.5	59.6	197049	300.1	347.5
dAPeriph	60-100%	0	405257	47.3	67.6	362144	154.0	169.6
		1	1206211	158.0	187.9	1148490	486.8	605.4
dAPeriph	30-60%	0	425050	90.3	116.9	396956	269.5	308.5
		1	1230798	271.0	342.9	1129980	792.1	982.6
ppVertex	MinBias	0	194378	19.1	20.2	143230	45.7	55.1
		1	648729	72.2	78.1	1125723	360.7	437.5

Table B.5: Summary of Weighted \bar{p} and Event Counts for All Data Sets

Trigger	Centrality	BO	nEvents B^+	nTracks B^+		nEvents B^-	nTracks B^-	
				arm N	arm P		arm N	armP
dAVertex	60-100%	0	253107	104.6	111.7	73873	14.1	22.1
		1	141599	57.0	57.0	225234	48.0	50.0
		2	287792	107.9	118.0	197822	51.1	52.1
		3	153573	53.9	61.0	263854	60.6	55.8
dAVertex	30-60%	0	456294	374.1	391.4	132953	56.3	80.5
		1	262671	236.9	241.9	415791	183.1	230.2
		2	534937	433.8	503.5	375660	164.3	185.3
		3	287727	251.7	264.8	507318	251.5	245.8
dAVertex	10-30%	0	349935	395.0	494.1	101571	63.2	79.3
		1	202633	284.9	247.9	320457	236.2	283.1
		2	412234	555.4	619.3	292193	183.2	248.6
		3	221285	282.6	323.0	396562	324.2	342.8
dAVertex	0-10%	0	167952	291.4	295.2	48801	55.1	53.2
		1	98475	149.0	192.9	154719	146.1	184.1
		2	200990	329.8	362.6	143321	159.3	171.2
		3	108846	187.1	191.0	197049	185.9	231.6
dAPeriph	60-100%	0	405257	193.2	220.3	362144	98.4	109.7
		1	1206211	550.7	600.1	1148409	327.9	330.2
dAPeriph	30-60%	0	425050	308.6	377.3	396956	183.2	187.5
		1	1230798	949.4	1071.8	1129980	514.8	575.8
ppVertex	MinBias	0	194378	85.0	60.1	143230	26.8	42.0
		1	648729	209.1	231.2	1125723	203.5	233.5

Table B.6: Summary of Weighted p and Event Counts for All Data Sets

Trigger	Centrality	BO	nEvents B^+	nTracks B^+		nEvents B^-	nTracks B^-	
				arm N	arm P		arm N	armP
dAVertex	60-100%	0	253107	64.8	78.9	73873	30.0	33.0
		1	141599	39.0	54.0	225234	87.0	115.0
		2	287792	78.9	91.9	197822	101.0	113.1
		3	153573	53.2	57.2	263854	137.8	105.9
dAVertex	30-60%	0	456294	284.0	301.8	132953	153.1	147.3
		1	262671	172.9	196.9	415791	420.1	503.1
		2	534937	318.4	389.3	375660	390.2	455.5
		3	287727	166.5	222.2	507318	534.2	619.2
dAVertex	10-30%	0	349935	326.5	416.2	101571	186.5	197.5
		1	202633	161.9	236.8	320457	508.0	594.1
		2	412234	368.4	442.0	292193	460.2	578.6
		3	221285	200.0	226.2	396562	641.4	677.0
dAVertex	0-10%	0	167952	244.1	217.1	48801	89.3	117.3
		1	98475	118.9	152.9	154719	320.1	367.1
		2	200990	248.5	285.4	143321	304.1	333.4
		3	108846	140.1	163.0	197049	435.5	501.8
dAPeriph	60-100%	0	405257	130.7	143.5	362144	197.6	210.6
		1	1206211	376.7	434.4	1148409	707.2	726.1
dAPeriph	30-60%	0	425050	230.7	266.2	396956	404.1	427.3
		1	1230798	708.9	802.9	1129980	1094.0	1256.5
ppVertex	MinBias	0	194378	39.2	55.3	143230	63.0	76.0
		1	648729	151.4	150.3	1125723	481.8	519.8

Appendix C

Systematic Errors: dAVertex and dAPeriph

Table C.1: Event Selection Systematic Errors for the dAVertex and dAPeriph Data Sets

Event Selection Systematics				
Bunch Selectivity				
Species	Trigger	Pt-to-Pt Sys	Scale Sys	Comment
π	dAVertex	± 0.001	0	No sig sys var: $\frac{1}{2}\sigma$ MB
	dAPeriph	± 0.001	0	No sig sys var: $\frac{1}{2}\sigma$ MB
Kaon	dAVertex	± 0.005	0	No sig sys var: $\frac{1}{2}\sigma$ MB
	dAPeriph	± 0.005	0	No sig sys var: $\frac{1}{2}\sigma$ MB
Proton	dAVertex	0	± 0.006	Deviate low
	dAPeriph	0	± 0.006	Deviate low
PileUp				
Species	Trigger	Pt-to-Pt Sys	Scale Sys	Comment
π	dAVertex	± 0.0005	0	No sig sys var: $\frac{1}{2}\sigma$ MB
	dAPeriph	± 0.0005	0	No sig sys var: $\frac{1}{2}\sigma$ MB
Kaon	dAVertex	0	± 0.003	Deviate high
	dAPeriph	0	± 0.003	Deviate low
Proton	dAVertex	± 0.001	0	No sig sys var: $\frac{1}{2}\sigma$ MB
	dAPeriph	± 0.001	0	No sig sys var: $\frac{1}{2}\sigma$ MB
OctDeVz Status				
Species	Trigger	Pt-to-Pt Sys	Scale Sys	Comment
π	dAVertex	± 0.0005	0	No sig sys var: $\frac{1}{2}\sigma$ MB
	dAPeriph	± 0.0005	0	No sig sys var: $\frac{1}{2}\sigma$ MB
Kaon	dAVertex	± 0.003	0	No sig sys var: $\frac{1}{2}\sigma$ MB
	dAPeriph	± 0.003	0	No sig sys var: $\frac{1}{2}\sigma$ MB
Proton	dAVertex	± 0.002	0	Deviate low
	dAPeriph	± 0.002	0	No sig sys var: $\frac{1}{2}\sigma$ MB
OctDeVz Ranges				
Species	Trigger	Pt-to-Pt Sys	Scale Sys	Comment
π	dAVertex	± 0.001	± 0.002	Left and right: Deviate low Std variation: No sig sys var: $\frac{1}{2}\sigma$ MB
	dAPeriph	± 0.001	± 0.002	Left and right: Deviate low Std variation: No sig sys var: $\frac{1}{2}\sigma$ MB
Kaon	dAVertex	± 0.002	± 0.01	Left and right: One point crazy Std variation: No sig sys var: $\frac{1}{2}\sigma$ MB
	dAPeriph	± 0.002	± 0.01	Left and right: One point crazy Std variation: No sig sys var: $\frac{1}{2}\sigma$ MB
Proton	dAVertex	± 0.002	0	Left and right: no sig. sys var Std variations: No sig sys var: $\frac{1}{2}\sigma$ MB
	dAPeriph	± 0.002	0	Left and right: no sig. sys var Std variations: No sig sys var: $\frac{1}{2}\sigma$ MB

Table C.2: Centrality Determination Systematic Errors for the dAVertex and dAPeriph Data Sets

Centrality Determination Systematics				
Centrality Measure				
Species	Trigger	Pt-to-Pt Sys	Scale Sys	Comment
π	dAVertex	± 0.01	0	Envelope encompasses most values
	dAPeriph	± 0.01	0	Envelope encompasses most values
Kaon	dAVertex	± 0.02	0	Envelope encompasses most values
	dAPeriph	± 0.02	0	Envelope encompasses most values
Proton	dAVertex	± 0.02	0	Envelope encompasses most values
	dAPeriph	± 0.02	0	Envelope encompasses most values
Centrality Cut				
Species	Trigger	Pt-to-Pt Sys	Scale Sys	Comment
π	dAVertex	± 0.003	0	Envelope encompasses most values
	dAPeriph	± 0.003	0	Envelope encompasses most values
Kaon	dAVertex	± 0.01	0	Envelope encompasses most values
	dAPeriph	± 0.01	0	Envelope encompasses most values
Proton	dAVertex	± 0.01	0	Envelope encompasses most values
	dAPeriph	± 0.01	0	Envelope encompasses most values
Centrality Scaling				
Species	Trigger	Pt-to-Pt Sys	Scale Sys	Comment
π	dAVertex	± 0.003	0	Envelope encompasses most values
	dAPeriph	± 0.003	0	Envelope encompasses most values
Kaon	dAVertex	± 0.015	0	Envelope encompasses most values
	dAPeriph	± 0.015	0	Envelope encompasses most values
Proton	dAVertex	± 0.01	0	Envelope encompasses most values
	dAPeriph	± 0.01	0	Envelope encompasses most values

Table C.3: Track Selection Systematic Errors for the dAVertex and dAPeriph Data Sets

Track Selection Systematics				
Track Fit Probability				
Species	Trigger	Pt-to-Pt Sys	Scale Sys	Comment
π	dAVertex	± 0.001	0	Deviation significant
	dAPeriph	± 0.001	0	Deviation significant
Kaon	dAVertex	± 0.001	0	No sig sys var: $\frac{1}{2}\sigma$ MB
	dAPeriph	± 0.001	0	No sig sys var: $\frac{1}{2}\sigma$ MB
Proton	dAVertex	± 0.004	0	Deviation significant
	dAPeriph	± 0.004	0	Deviation significant
Dca Cut				
Species	Trigger	Pt-to-Pt Sys	Scale Sys	Comment
π	dAVertex	± 0.001	0	Deviation significant
	dAPeriph	± 0.001	0	Deviation significant
Kaon	dAVertex	± 0.001	0	No sig sys var: $\frac{1}{2}\sigma$ MB
	dAPeriph	± 0.001	0	No sig sys var: $\frac{1}{2}\sigma$ MB
Proton	dAVertex	± 0.005	0	Deviation significant
	dAPeriph	± 0.005	0	Deviation significant
Vertex Agreement				
Species	Trigger	Pt-to-Pt Sys	Scale Sys	Comment
π	dAVertex	0	± 0.001	Deviation significant
	dAPeriph	0	± 0.001	Deviation significant
Kaon	dAVertex	0	± 0.005	Deviation significant
	dAPeriph	0	± 0.005	Deviation significant
Proton	dAVertex	0	± 0.005	Deviation significant.
	dAPeriph	0	± 0.005	Deviation significant
p_T Cut				
Species	Trigger	Pt-to-Pt Sys	Scale Sys	Comment
π	dAVertex	± 0.001	0	No sig sys var: $\frac{1}{2}\sigma$ MB
	dAPeriph	± 0.001	0	No sig sys var: $\frac{1}{2}\sigma$ MB
Kaon	dAVertex	± 0.002	0	No sig sys var: $\frac{1}{2}\sigma$ MB
	dAPeriph	± 0.002	0	No sig sys var: $\frac{1}{2}\sigma$ MB
Proton	dAVertex	± 0.012	0	Deviation significant
	dAPeriph	± 0.012	0	Deviation significant

Table C.4: Particle Identification Systematic Errors for the dAVertex and dAPeriph Data Sets

Particle Identification Systematics				
<i>dE/dx</i> Cut: Band Sigma Variation				
Species	Trigger	Pt-to-Pt Sys	Scale Sys	Comment
π	dAVertex	N/A	N/A	Not applicable
	dAPeriph	N/A	N/A	Not applicable
Kaon	dAVertex	± 0.002	0	No sig sys var: $\frac{1}{2}\sigma$ MB
	dAPeriph	± 0.005	0	Deviation significant
Proton	dAVertex	± 0.002	0	No sig sys var: $\frac{1}{2}\sigma$ MB
	dAPeriph	± 0.007	0	Deviation significant
<i>dE/dx</i> Cut: <i>dE/dx</i> Cut Variation				
Species	Trigger	Pt-to-Pt Sys	Scale Sys	Comment
π	dAVertex	0	0	Not applicable
	dAPeriph	0	0	Not applicable
Kaon	dAVertex	± 0.01	0	Deviation significant
	dAPeriph	± 0.015	0	Deviation significant
Proton	dAVertex	± 0.005	0	Deviation significant
	dAPeriph	± 0.005	0	Deviation significant
p cut: Band Sigma Variation				
Species	Trigger	Pt-to-Pt Sys	Scale Sys	Comment
π	dAVertex	0	± 0.002	Deviate high
	dAPeriph	0	± 0.002	Deviate high
Kaon	dAVertex	± 0.01	0	No sig sys var: $\frac{1}{2}\sigma$ MB
	dAPeriph	± 0.01	0	No sig sys var: $\frac{1}{2}\sigma$ MB
Proton	dAVertex	± 0.005	0	No sig sys var: $\frac{1}{2}\sigma$ MB
	dAPeriph	± 0.01	0	No sig sys var: $\frac{1}{2}\sigma$ MB
p Cut: p Cut Variation				
Species	Trigger	Pt-to-Pt Sys	Scale Sys	Comment
π	dAVertex	± 0.007	0	Deviation significant
	dAPeriph	± 0.007	0	Deviation significant
Kaon	dAVertex	N/A	N/A	Not applicable
	dAPeriph	N/A	N/A	Not applicable
Proton	dAVertex	N/A	N/A	Not applicable
	dAPeriph	N/A	N/A	Not applicable

Table C.5: Other Systematic Errors for the dAVertex and dAPeriph Data Sets

Other Systematics				
Vz Counts Correction				
Species	Trigger	Pt-to-Pt Sys	Scale Sys	Comment
π	dAVertex	± 0.0005	0	Deviation significant
	dAPeriph	± 0.0005	0	Deviation significant
Kaon	dAVertex	± 0.0005	0	No sig sys var: $\frac{1}{2}\sigma$ MB
	dAPeriph	± 0.0005	0	No sig sys var: $\frac{1}{2}\sigma$ MB
Proton	dAVertex	± 0.0005	0	No sig sys var: $\frac{1}{2}\sigma$ MB
	dAPeriph	± 0.0005	0	No sig sys var: $\frac{1}{2}\sigma$ MB
Dead Channel Map				
Species	Trigger	Pt-to-Pt Sys	Scale Sys	Comment
π	dAVertex	± 0.005	0	No sig sys var: $\frac{1}{2}\sigma$ MB
	dAPeriph	± 0.005	0	No sig sys var: $\frac{1}{2}\sigma$ MB
Kaon	dAVertex	± 0.005	0	No sig sys var: $\frac{1}{2}\sigma$ MB
	dAPeriph	± 0.005	0	No sig sys var: $\frac{1}{2}\sigma$ MB
Proton	dAVertex	± 0.005	0	No sig sys var: $\frac{1}{2}\sigma$ MB
	dAPeriph	± 0.005	0	No sig sys var: $\frac{1}{2}\sigma$ MB
Spectrometer Arm				
Species	Trigger	Pt-to-Pt Sys	Scale Sys	Comment
π	dAVertex	0	± 0.004	Deviation significant
	dAPeriph	0	± 0.004	Deviation significant
Kaon	dAVertex	0	± 0.015	Deviation significant
	dAPeriph	0	± 0.015	Deviation significant
Proton	dAVertex	0	± 0.01	Deviation significant
	dAPeriph	0	± 0.01	Deviation significant
Beam Orbit Region				
Species	Trigger	Pt-to-Pt Sys	Scale Sys	Comment
π	dAVertex	± 0.01	0	No sig sys var: $\frac{1}{2}\sigma$ MB
	dAPeriph	± 0.01	0	No sig sys var: $\frac{1}{2}\sigma$ MB
Kaon	dAVertex	± 0.01	0	No sig sys var: $\frac{1}{2}\sigma$ MB
	dAPeriph	± 0.01	0	No sig sys var: $\frac{1}{2}\sigma$ MB
Proton	dAVertex	± 0.01	0	No sig sys var: $\frac{1}{2}\sigma$ MB
	dAPeriph	± 0.01	0	No sig sys var: $\frac{1}{2}\sigma$ MB

Appendix D

Systematic Errors: ppVertex

Table D.1: Event Selection Systematic Errors for the dAVertex and dAPeriph Data Sets

Event Selection Systematics		
Paddle Time		
Species	Sys	Comment:
π	± 0.003	No sig sys var: $\frac{1}{2}\sigma$ MB
Kaon	± 0.003	no sig deviation; use pion est
Proton	± 0.005	No sig sys var: $\frac{1}{2}\sigma$ MB
PileUp		
Species	Sys	Comment
π	± 0.002	No sig sys var: $\frac{1}{2}\sigma$ MB
Kaon	± 0.002	no sig deviation; use pion est
Proton	± 0.004	No sig sys var: $\frac{1}{2}\sigma$ MB
OctDe Status		
Species	Sys	Comment
π	± 0.003	No sig sys var: $\frac{1}{2}\sigma$ MB
Kaon	± 0.003	no sig deviation; use pion est
Proton	± 0.003	no sig deviation; use pion est
OctDeVz Ranges		
Species	Sys	Comment:
π	± 0.001	no dev use min est
Kaon	± 0.001	no sig deviation; use pion est
Proton	± 0.001	no sig deviation; use pion est

Table D.2: Track Selection Systematic Errors for the ppVertex Data Set

Track Selection Systematics		
Track Prob Fit Cut		
Species	Sys	Comment: Do not use no trk fit variation
π	± 0.002	No sig sys var: $\frac{1}{2}\sigma$ MB
Kaon	± 0.002	no sig deviation; use pion est
Proton	± 0.004	No sig sys var: $\frac{1}{2}\sigma$ MB
Dca Cuts		
Species	Sys	Comment: Only use loose and tight variations
π	± 0.0007	No sig sys var: $\frac{1}{2}\sigma$ MB
Kaon	± 0.0003	No sig sys var: $\frac{1}{2}\sigma$ MB
Proton	± 0.006	No sig sys var: $\frac{1}{2}\sigma$ MB
Vertex agreement cuts		
Species	Sys	Comment: Only use loose and tight variations
π	± 0.002	No sig sys var: $\frac{1}{2}\sigma$ MB
Kaon	± 0.007	No sig sys var: $\frac{1}{2}\sigma$ MB
Proton	± 0.002	No sig sys var: $\frac{1}{2}\sigma$ MB
P_T cuts		
Species	Sys	Comment:
π	± 0.001	no dev use min est
Kaon	± 0.012	No sig sys var: $\frac{1}{2}\sigma$ MB
Proton	± 0.016	No sig sys var: $\frac{1}{2}\sigma$ MB

Table D.3: Particle Identification Systematic Errors for the ppVertex Data Set

Particle Identification Systematics		
dE/dx cut: band σ variation		
Species	Sys	Comment: Use values from dAu analysis
π	N/A	Not applicable
Kaon	± 0.002	dAu
Proton	± 0.002	dAu
dE/dx cut: cut position variation		
Species	Sys	Comment: Use values from dAu analysis
π	N/A	Not applicable
Kaon	± 0.01	dAu
Proton	± 0.005	dAu
p cut: band σ variation		
Species	Sys	Comment: Use values from dAu analysis
π	± 0.002	dAu
Kaon	± 0.01	dAu
Proton	± 0.005	dAu
p cut: cut position variation		
Species	Sys	Comment: Use values from dAu analysis
π	± 0.007	dAu
Kaon	N/A	Not applicable
Proton	N/A	Not applicable

Table D.4: Other Systematic Errors for the ppVertex Data Set

Other Systematics		
Vz correction		
Species	Sys	Comment
π	± 0.003	No sig sys var: $\frac{1}{2}\sigma$ MB
Kaon	± 0.003	no sig deviation; use pion est
Proton	± 0.003	no sig deviation; use pion est
Dead Channel Map		
Species	Sys	Comment
π	± 0.005	dAu
Kaon	± 0.005	dAu
Proton	± 0.005	dAu
Spectrometer Arm		
Species	Sys	Comment
π	± 0.01	No sig sys var: $\frac{1}{2}\sigma$ MB
Kaon	± 0.01	use pion est
Proton	± 0.01	use pion est
Beam Orbit Region		
Species	Sys	Comment
π	± 0.01	
Kaon	± 0.01	
Proton	± 0.01	

BIBLIOGRAPHY

- [1] J. P. Blaizot, Nucl. Phys. A **661**, 3 (1999).
- [2] S. Eidelman *et al.*, Phys. Lett. B **592**, 1 (2004).
- [3] B. B. Back *et al.*, Phys. Rev. C **65**, 31901R (2002).
- [4] M. Gyulassy and M. Plumer, Phys. Lett. B **243**, 432 (1990).
- [5] R. Baier *et al.*, Phys. Lett. B **345**, 277 (1995).
- [6] P. Kolb, J. Sollfrank, and U. Heinz, Phys. Rev. C **62**, 054909 (2000).
- [7] S. A. Voloshin and A. M. Poskanzer, Phys. Lett. B **474**, 27 (2000).
- [8] B. B. Back *et al.*, Phys. Rev. Lett. **87**, 102301 (2001).
- [9] S. Pratt, Phys. Rev. Lett. **53**, 1219 (1984).

- [10] S. Pratt, Phys. Rev. D **33**, 1314 (1986).
- [11] GEANT 3.2.1, CERN Computing Library,
<http://wwwasd.web.cern.ch/wwwasd/geant/index.html>.
- [12] M. Gyulassy and X. N. Wang, Comput. Phys. Commun. **83**, 307 (1994). HI-JING v1.383 used for d+Au, and v1.35 used for Au+Au.
- [13] X. N. Wang and M. Gyulassy, Phys. Rev. D **44**, 3501 (1991).
- [14] Z. W. Lin, S. Pal, C. M. Ko, B. A. Li and B. Zhang, Phys. Rev. C **64**, 011902 (2001).
- [15] B. Zhang, C. M. Ko, B. A. Li and Z. Lin, Phys. Rev. C **61**, 067901 (2000).
- [16] M. Gyulassy, Y. Pang, and B. Zhang, Nucl. Phys. A **626**, 999 (1997).
- [17] B. Zhang, Compt. Phys. Commun. **109**, 193 (1998).
- [18] B. Andersson, G. Gustafson, G. Ingelman, and T. Sjostrand, Phys. Rep. **97**, 31 (1983).
- [19] B. Andersson, G. Gustafson, and B. Soderberg, Z. Phys. C **20**, 317 (1983).
- [20] T. Sjostrand, Comput. Phys. Commun. **82**, 74 (1994).
- [21] B. A. Li and C. M. Ko, Phys. Rev. C **52**, 2037 (1995).
- [22] H. Sorge, Phys. Rev. C **52**, 3291 (1995). Used version 2.4, including rope formation.

- [23] A. Bialas *et al.*, Nucl. Phys. **111**, 461 (1976).
- [24] A. Bialas *et al.*, Phys. Rev. D **25**, 2328 (1982).
- [25] A. Bialas *et al.*, Z. Phys. C **13**, 147 (1982).
- [26] B. B. Back *et al.*, Phys. Rev. Lett. **91**, 072302 (2003).
- [27] S. S. Adler *et al.*, Phys. Rev. Lett. **91**, 072303 (2003).
- [28] J. Adams *et al.*, Phys. Rev. Lett. **91**, 072304 (2003).
- [29] I. Arsene *et al.*, Phys. Rev. Lett. **91**, 072305 (2003).
- [30] I. G. Bearden *et al.*, Phys. Rev. Lett. **90**, 102301 (2002).
- [31] B. B. Back *et al.*, Phys. Rev. C **67**, 021901 (2003).
- [32] C. Adler *et al.*, Phys. Rev. Lett. **87**, 262302 (2001).
- [33] C. Adler *et al.*, Phys. Rev. Lett. **86**, 4778 (2001), Phys. Rev. Lett. **90**, 119903(E) (2003).
- [34] B. B. Back *et al.*, Phys. Rev. Lett. **87**, 102301 (2001).
- [35] I. G. Bearden *et al.*, Phys. Rev. Lett. **87**, 112305 (2001).
- [36] K. Adcox *et al.*, Phys. Rev. Lett. **88**, 242301 (2002).
- [37] B. B. Back *et al.*, Nucl. Phys. A **715**, 510c (2003).
- [38] G. van Buren *et al.*, Nucl. Phys. A **715**, 129c (2003).

- [39] S. S. Adler *et al.*, Phys. Rev. C **69**, 034909 (2004).
- [40] W. Busza and A. S. Goldhaber, Phys. Lett. B **139**, 235 (1984).
- [41] K. Abe *et al.*, Phys. Lett. B **200**, 266 (1988).
- [42] C. J. Gardner. Heavy Ion Parameters for 1995. AGS/AD/Tech. Note No. 417, Brookhaven National Laboratory (1995).
- [43] R. Bindel *et al.*, Nucl. Instr. Meth. A **474**, 38 (2001).
- [44] R. Bindel *et al.*, Nucl. Instr. Meth. A **488**, 94 (2002).
- [45] C. Adler *et al.*, Nucl. Instr. Meth. A **470**, 488 (2001).
- [46] B. B. Back *et al.*, Phys. Rev. C **70**, 011901(R) (2004).
- [47] B. Back *et al.*, Nucl. Instr. Meth. A **499**, 603 (2003).
- [48] P. Sarin, *Measurement of charged particle multiplicity distributions in Au+Au collisions up to 200 GeV*. Ph.D. Thesis, Massachusetts Institute of Technology (2003).
- [49] S. Johnson, R. Soltz, G. Kunde, *Measuring Centrality in pA/dA Collisions at RHIC with Grey Protons*. Poster, presented at the Quark Matter 2002 conference, http://www.phenix.bnl.gov/conf_2002.html.
- [50] P. V. C. Hough and B. W. Powell, Nuovo Cimento **18**, 1184 (1960).

- [51] K. Gulbrandsen, *Relative Yields of Antiparticles to Particles in Au+Au collisions at 130 and 200 GeV Per Nucleon Pair*. Ph.D. Thesis, Massachusetts Institute of Technology (2004).
- [52] W. S. C. Williams, *Nuclear and Particle Physics*. Clarendon Press; New York (1997).
- [53] W. R. Leo, *Techniques for Nuclear and Particle Physics Experiments*. Springer-Verlag; Berlin (1987).
- [54] D. H. Perkins, *Introduction to High Energy Physics*. Addison-Wesley Publishing; Reading, Massachusetts (1987).
- [55] J. Zimányi, Nucl. Phys. A **661**, 224 (1999).
- [56] A. Billmeier, J. Phys. G. **30**, S363 (2004).
- [57] K. Adcox *et al.*, Phys. Rev. Lett. **89**, 092302 (2002).
- [58] H. C. Fesefeldt. The simulation of hadronic showers: Physics and applications. Technical report, 1985. PITHA-85-02.
- [59] P. A. Aarnio. Fluka user's guide. Technical report, 1987. TIS-RP-190.
- [60] J. Adams *et al.*, nucl-ex/0309012.
- [61] I. G. Bearden *et al.*, nucl-ex/0409002.
- [62] B. B. Back *et al.*, nucl-ex/0409003.
- [63] L. Ahle *et al.*, Phys. Rev. Lett. **81**, 2650 (1998),

- [64] L. Ahle *et al.*, Phys. Rev. C **60**, 064901 (1999).
- [65] M. Banner *et al.*, Phys. Lett. B **122**, 322 (1983).
- [66] M. Aguilar-Benitez *et al.*, Z. Phys. C **50**, 405 (1991).
- [67] I. G. Bearden *et al.*, Phys. Lett. B **388** 431 (1996).
- [68] J. Bächler *et al.*, Nucl. Phys. A **661** 45 (1999).
- [69] A. M. Rossi *et al.*, Nucl. Phys. B **84**, 269 (1975).
- [70] K. Guettler *et al.*, Nucl. Phys. **B116**, 77 (1976).